Magnetic Nanoparticles: Synthesis, Characterization, Applications and a Systematic Study of Exchange Biasing

by

Joseph B. Tracy

B.S. in Creative Studies, Emphasis in Chemistry
Minors in German and Mathematics
University of California, Santa Barbara, 2000

Submitted to the Department of Chemistry in
Partial Fulfillment of the Requirements for the Degree of

DOCTOR OF PHILOSOPHY

at the

MASSACHUSETTS INSTITUTE OF TECHNOLOGY

June 2005

Signature of Author _____
Department of Chemistry
May 10, 2005

Certified by _____
Moungi G. Bawendi
Professor of Chemistry
Thesis Supervisor

Accepted by _____
Robert W. Field
Chairman, Departmental Committee on Graduate Students

This doctoral thesis has been examined by a committee of the Department of Chemistry as follows:

Professor Robert Griffin _____
Chairman

Professor Moungi Bawendi _____
Thesis Supervisor

Professor Rajeev Ram _____
Department of Electrical Engineering and Computer Science

Magnetic Nanoparticles: Synthesis, Characterization, Applications and a Systematic Study of Exchange Biasing

by

Joseph B. Tracy

Submitted to the Department of Chemistry on May 10, 2005 in partial fulfillment of the requirements for the degree of Doctor of Philosophy in Chemistry

ABSTRACT

We systematically investigated the magnetic properties of colloidal cobalt nanoparticles after three extents of oxidation: The native sample has a thin (1.0 nm) CoO shell and exhibits no exchange biasing. The purposefully partially oxidized sample has a thicker CoO shell (3.2 nm), and is exchange biased. The sample fully oxidized to CoO looses exchange biasing. Three distinct magnetic properties that result from the finite-thickness antiferromagnet shell exchange coupled to a finite-size ferromagnet core, and from crystal and stoichiometric defects, were observed: (1) an enhancement of the thermal stability of the orientation of the magnetic moment due to exchange biasing in the partially oxidized sample, (2) a low temperature paramagnetic response in the partially and fully oxidized samples due to crystallographic and stoichiometric defects in the CoO shell, and (3) an asymmetry in the field-dependent magnetization for the partially oxidized sample at low temperature due to small clusters of Co in a diffusion layer around the Co core. We interpret these effects using a simple phenomenological model and propose a method for fabricating magnetic media using exchange biased nanoparticles.

We further investigated the defect moments in the CoO shell and their role in exchange biasing. The distribution of the defect moments' melting temperatures was measured, and most melt below 50 K, which is well below the temperature at which the CoO lattice moments freeze. Experiments in the partially oxidized sample, in which the polarity of the biasing field was switched during cooling, show that the defect moments pin the Co core more strongly than the CoO lattice and thereby dominate exchange biasing at low temperature. At higher temperatures, the CoO defects are paramagnetic and cannot contribute to pinning, and the CoO lattice controls exchange biasing. By switching the field polarity and switching to zero field during cooling, exchange shift and coercivity tunability was demonstrated. We interpret these results using the domain state model of exchange biasing.

We also present results for the preparation and characterization of γ-Fe_2O_3 and FePt nanoparticles.

Thesis Supervisor: Moungi G. Bawendi
Title: Professor of Chemistry

Four things on earth are small,
yet they are exceedingly wise:

the ants are a people without strength,
yet they provide their food in the summer;

the badgers are a people without power,
yet they make their homes in the rocks;

the locusts have no king,
yet all of them march in rank;

the lizard can be grasped in the hand,
yet it is found in kings' palaces.

(Proverbs 30:24-28, NRSV)

Soli Deo Gloria

Table of Contents

Title page …….. 1
Signature page……3
Abstract……..5
Dedication……..7
Table of contents……9

Chapter 1: Introduction to nanomaterials
1.1: Defining the nanoscale……..13
1.2: Methods of fabricating nanostructures and self-assembly……14
1.3: Nanoparticles……15
1.3.1: Metallic nanoparticles……16
1.3.2: Semiconductor nanoparticles: ……...……16
1.3.3: Magnetic nanoparticles……..17
1.4: Nanowires ……18
1.5: Fullerenes and nanotubes……..18
1.6: Composite nanomaterials……..19
1.7: Toxicity concerns……..19
1.8: References……20

Chapter 2: Introduction to magnetic materials and measurements
2.1: Introduction to magnetic materials……... 23
2.1.1: Origin of magnetism……..23
2.1.2: Domain formation……..25
2.1.3: Magnetocrystalline anisotropy……...26
2.1.4: Superparamagnetism……..26
2.2: Magnetic measurements……...… 27
2.2.1: Temperature-dependent magnetization: blocking temperature…..… 27
2.2.2: Thermal remanent magnetization……..… 29
2.2.3: Field-dependent magnetization: history is important…… 30
2.3: Exchange bias……...… 31
2.4: Choice of materials……...34
2.5: Thesis overview……35
2.6: References……37

Chapter 3: Systematic study of exchange biasing in cobalt nanoparticles with different extents of oxidation
3.1: Introduction……...…39
3.2: Experimental……40
3.2.1: Preparation of systematically oxidized cobalt nanoparticles……40
3.2.2: Incorporation into polymer sticks……...…41
3.3: Transmission electron microscopy……... 44
3.4: Magnetic data: results and discussion……...48
3.4.1: Oxide thickness, magnetocrystalline anisotropy constants, and increased blocking temperature due to exchange biasing……..49

3.4.2: Defects in the CoO shell……57
3.4.3: Phenomenological model: physical picture and temperature-dependence of exchange shift and coercivity…… 58
3.5: Proposal…… 63
3.6: Conclusions……...64
3.7: References……65
Appendix A: Method for preparing small (*d* = 2-3 nm) cobalt Nanoparticles……...68
Appendix B: Justification that cobalt nanoparticles are non-interacting in the polymer matrix……70
Appendix C: Supplementary data……..……...73
Appendix D: Curie-Weiss law analysis……75

Chapter 4: Defects in CoO dominate exchange biasing in partially oxidized cobalt nanoparticles
4.1: Defects and the domain state model of exchange biasing…… 77
4.2: First switching experiment: field-dependent magnetization……79
4.2.1: Defects dominate exchange bias…….……...79
4.2.2: Exchange field changes sign during heating……. 82
4.3: Second switching experiment: causing the exchange field to change sign twice during cooling……...83
4.4: Third switching experiment: randomizing exchange biasing at low temperature…… 85
4.5: Fourth switching experiment: switching to or from zero field……. 89
4.6: Discussion of coercivity……... 92
4.7: First switching experiment: thermal remanent magnetization……..93
4.8: Fifth switching experiment: memory effect of repeated switching during cooling……100
4.9: Second switching experiment: thermal remanent magnetization……... 102
4.10: Third switching experiment: thermal remanent magnetization…… 104
4.11: Fourth switching experiment: thermal remanent magnetization……..… 110
4.12: Sixth switching experiment: switching during heating…… 112
4.13: Seventh switching experiment: switching during cooling and heating…… 115
4.14: Thermal remanent magnetization: cooling field dependence……... 117
4.15: Magnetic training effect……... 118
4.16: Conclusions and data to 2.5 K…….. 120
4.17: References……..... 124
Appendix E: Supplementary data…….. 125
Appendix F: Conversion of thermal remanent magnetization to moment per particle……. 129

Chapter 5: Iron oxide nanoparticles and their incorporation into silica microspheres with quantum dots
5.1: Introduction…… 130
5.2: Chemistry and characterization of γ-Fe_2O_3 nanoparticles……..… 130
5.2.1: Preparation……...130

5.2.2: Transmission electron microscopy…….. 131
5.2.3: Magnetic properties……..... 134
5.2.4: Discussion of coercivity……..… 136
5.3: Incorporation of γ-Fe_2O_3 nanoparticles into SiO_2 microspheres with quantum dots……...…137
5.3.1: Background……...…138
5.3.2: Preparing the nanoparticles for incorporation……. 138
5.3.3: Incorporation……... 139
5.3.4: Characterization of the product……... 140
5.4: Trapping SiO_2(core)//SiO_2,Fe_2O_3,CdSe/CdZnS(shell) microspheres on a microelectromagnetic device…….. 142
5.5: Conclusions…… 145
5.6: References…….. 146

Chapter 6: Iron platinum alloy nanoparticles
6.1: Introduction…… 147
6.2: Preparation of FePt nanoparticles……...148
6.3: Surface chemistry……... 149
6.3.1: Octadecanethiol……... 149
6.3.2: Solubility in ethanol……149
6.4: Transmission electron microscopy……. 150
6.5: Magnetic characterization……...154
6.6: References…….. 156

Chapter 7: Functionalization and magnetic properties of commercial cobalt nanoparticles
7.1: Introduction…… 157
7.2: Surface chemistry……... 157
7.3: Transmission electron microscopy……. 158
7.4: Magnetic characterization……...161
7.5: References…….. 163

Appendix G: Guide to Electron Microscopy
G.1: Motivation……..164
G.2: Sample preparation…… 164
G.3: Microscope setup……...165
G.4: Stigmation, focusing, and illumination……..165
G.5: Magnification……..…167
G.6: Taking pictures…….. 167
G.7: Electron diffraction……168
G.8: Choosing the right microscope……..169
G.9: Developing pictures……...…169
G.10: Scanning pictures and adding scale bars……..… 170

Acknowledgements……..…. 171

Chapter 1

Introduction to nanomaterials

1.1: Defining the nanoscale

Atoms and small molecules have been the subject of intense investigation by physical chemists, in particular in gas-phase laser spectroscopy[1] and mass spectrometry[2]. Such investigations have been important for understanding phenomena in nature, such as atmospheric chemistry[3]. Atoms and small molecules have also found diverse applications in trace detection[4], remote sensing[5], and as lasing media in CO_2 and Ar^+ ion lasers[6]. Many applications exploit the fixed energy levels of small molecules, and the molecular homogeneity of a pure sample.

Macroscopic crystals are known as "bulk" materials. By varying the composition, purity, and patterning of bulk materials, materials with novel mechanical, electrical, optical, and magnetic properties have been prepared. These properties are often quite different from those of molecules with the same chemical composition.

Materials of intermediate size between small molecules and bulk materials, which we define as the "nanoscale" size regime (between about 1-100 nm), can exhibit novel properties that are different from materials of the same chemical composition in their molecular and bulk forms. These novel properties often originate from the high surface area to volume ratio in structures of this size. Surface effects, which are often negligible when studying bulk materials, are significant in nanostructures.

1.2: Methods of fabricating nanostructures and self-assembly

In nanoscience, new methods for preparing nanostructured materials are developed, and their physical and chemical properties are investigated. Knowledge of these novel properties enables new applications in nanotechnology, which may replace a competing technology, or may be entirely new applications. There is great promise for nanomaterials to have many applications in biology and information storage and processing due to their size scale.

There are two primary methods for preparing nanomaterials. Lithography has been highly developed as a method for etching and depositing nanoscale features in silicon and other semiconductors[7]. Lithography is an "etching-down" approach because it etches nanoscale features in a bulk material. Another approach is the "building-up" approach, in which molecular precursors, under the right conditions, are grown or assembled into nanoscale objects. The building-up approach is used in biological systems; proteins, DNA, and RNA are polymeric materials that are built up from amino and nucleic acids, which are again assembled into organelles, cells, and organisms.

The assembly process in biological systems is known as self-assembly. In self-assembly, simple structures are spontaneously transformed into more complex ones, when provided with the proper chemical and physical environment (temperature, pressure, electromagnetic excitation, etc.). The "chemical toolbox" of naturally occurring biological systems is highly refined and optimized for self-assembly. A major challenge in nanoscience is to find the right conditions for controlled self-assembly of artificial nanostructures, both of molecular precursors into nanoscale objects[8], and the secondary self-assembly of these nanoscale objects into more complicated composite structures[9, 10].

Nanomaterials with novel optical, electronic, magnetic, biological, and mechanical properties are of great interest. Nanoparticles (NPs), nanotubes, and nanowires are nanostructures that exhibit these novel properties. In order to maximize the range of novel properties and applications, many nanomaterials are hybrids of organic and inorganic materials. We briefly introduce each kind of nanomaterial.

1.3: Nanoparticles

NPs are small particles which nanoscale dimensions in every direction. There are a variety of methods used for preparing inorganic and organic NPs, including chemical vapor deposition[11], sputtering[12, 13], and microemulsion polymerization[14]. For NPs which have size-dependent physical properties, a highly monodisperse sample is desirable.

One method which has proven particularly useful for growing monodisperse NPs is the colloidal seeded-growth approach, which is often used to grow NPs with inorganic cores in solution from molecular precursors by first nucleating small seeds in solution and then growing additional precursors onto the nuclei. Both nucleation and growth steps are usually mediated by organic ligands. After the growth is finished, the NPs consist of inorganic cores with organic ligands bound to the surface, so that they may be individually dispersed in a variety of solvents and appropriately functionalized for different applications.

We now consider different classes of NPs, which are arranged by their novel physical properties.

1.3.1: Metallic nanoparticles

Au NPs have been used historically as a coloring agent in stained glass, before the phenomenon that gives rise to their coloration was understood[15]. Metallic NPs exhibit plasmon resonances, which are coherent oscillations of their conduction electrons throughout each NP that are excited by the electrical field of light[15, 16]. Au, Ag, and Cu NPs are well-known for having their plasmon frequencies in the visible spectrum[16], which causes their coloration, because light at the plasmon frequency is scattered more intensely than other colors. The plasmon resonance frequency depends on the NP volume and shape[17], and when two metallic NPs are in close proximity to each other, the electric fields of their plasmon resonances may couple, which causes a red-shift in the plasmon frequency. This phenomenon is applied in home pregnancy test kits[18] and other biological applications[19]. If many metallic NPs are patterned adjacent to one another, the excitation of the plasmon frequency may be wave-guided through the coupled particles, an effect which is studied and applied in the field of plasmonics[20].

1.3.2: Semiconductor nanoparticles

Semiconductor NPs, such as CdSe, have bright luminescence, the color of which is size-dependent[21]. For small semiconductor NPs, the valence and conduction band have not fully formed and consist instead of a series of discrete states. As the NP size increases, the band gap energy decreases, and the absorbance and emission peaks shift to the red. An exciton is similar to a hydrogen atom because it consists of an interacting positive and negative charge, and it also has a Bohr radius, which corresponds to the average electron-hole separation and is material-dependent. When the Bohr radius of the

exciton is on the order of or smaller than the NP radius, then the particle is said to be "quantum confined," and it has discrete states[22]. A quantum confined NP is called a "quantum dot" (QD). In the quantum confined regime, the band gap is size-dependent.

QDs have applications in many areas in which dye molecules are currently used. QDs have large absorbance cross sections, which are proportional to their core volume[23], and high quantum yields[24]. Although individual NPs exhibit blinking phenomena[25], they are more robust than dye molecules because they do not photobleach as rapidly[26]. Moreover, they do not need to be excited on-resonance as dye molecules do and can be multiplexed easily[27]. QDs have already found many applications in medicine[28] and biology[29], and more are under development.

1.3.3: Magnetic nanoparticles

Magnetic NPs are the main focus of this thesis. A more thorough introduction to magnetic NPs is given in Chapter **2**. Magnetic NPs have novel physical properties. Below a certain size limit (which is material-dependent), magnetic NPs are single-domain magnets. Their coercivity[30] and the thermal stability of the orientation of their magnetic moments are size-dependent. The atomic magnetic moments in ferromagnets, antiferromagnets, and ferrimagnets usually point along a preferred (easy) axis direction when no field is applied. The magnetocrystalline anisotropy energy (E_A) must be overcome to flip the moment from one easy axis to another (or into the opposite direction along the same easy axis). To first order, E_A scales linearly with the volume. For small NP sizes, E_A may be on the order of k_BT, and thermal energy causes the NP moments to fluctuate, which is known as superparamagnetism.

Magnetic recording is a key area for the application of magnetic NPs, if the problem of superparamagnetism can be overcome[12]. Magnetic NPs are also currently employed in biological separations[31] and magnetic resonance imaging[32]. More applications are under development [33], and magnetic NPs also have promise for applications in spintronics[34].

1.4: Nanowires

Nanowires (which have nanoscale dimensions in two directions and are elongated the their third dimension) have been prepared of metals, semiconductors, and magnetic materials. Nanowires have novel electron transport properties, but contacting them can be difficult. Electrically-pumped lasing from single semiconductor nanowires has been deomonstrated[35], and they have promise for application in nanophotonics[36] and nanoelectronics[37]. Nanowires also have been demonstrated to work as chemical[38] and biological sensors[39]. Magnetic nanowires[40] have an anisotropic coercivity and may be useful in magnetoresistive devices.

1.5: Fullerenes and nanotubes

The Nobel Prize in chemistry in 1996 was awarded to Robert Curl, Jr., Harold Kroto, and Richard Smalley for the discovery of fullerenes, which are ball-shaped molecules of carbon, such as C_{60}. Subsequently, carbon nanotubes (CNTs) were discovered. Analytically, a CNT is obtained by rolling up a graphene sheet, and the electronic structure and electrical properties are determined by how it is rolled[41]. CNTs have been used for many of the same applications as nanowires. Field-effect transistors

have been fabricated from CNTs[42], and their use in chemical sensing has also been demonstrated[43].

1.6: Composite nanomaterials

Each of the classes of nanomaterials discussed thus far is under intense investigation, but there is also great interest in developing biological applications for nanomaterials[44] and in preparing composite nanomaterials that combine the properties of these classes. Some examples of composite nanomaterials include Au-tipped CdSe nanorods[45], binary superlattices of magnetic and semiconductor NPs[9], heterodimers of metallic and magnetic NPs[46], and heterodimers[47] and small clusters of magnetic and semiconductor NPs[48]. Unique magnetooptically active materials have also been fabricated by connecting magnetic NPs to exfoliated sheets of perovskites[49].

1.7: Toxicity concerns

Since nanomaterials are of interest precisely because their physical properties differ from those of bulk materials of the same composition, there is concern that some nanomaterials may behave differently in the environment from their bulk counterparts and will thereby have different environmental health and safety impacts. Material Safety Data Sheets have not been generated for most nanomaterials, but they are needed for this reason[50]. One nanomaterial which has been investigated is C_{60}, which has been found to be significantly more toxic than graphite[51].

1.8: References

[1] W. Demtröder, *Laser spectroscopy : basic concepts and instrumentation* (Springer, Berlin ; New York, 2003).

[2] K. Downard and Royal Society of Chemistry (Great Britain), *Mass spectrometry : a foundation course* (Royal Society of Chemistry, Cambridge, 2004).

[3] R. L. Miller, A. G. Suits, P. L. Houston, R. Toumi, J. A. Mack, and A. M. Wodtke, Science 265, 1831 (1994).

[4] V. Swayambunathan, R. C. Sausa, and G. Singh, Applied Spectroscopy 54, 651 (2000).

[5] P. Hering, J. P. Lay, and S. Stry, *Laser in environmental and life sciences : modern analytical methods* (Springer, Berlin ; New York, 2004).

[6] D. L. Andrews, *Lasers in chemistry* (Springer-Verlag, Berlin ; New York, 1997).

[7] S. A. Campbell, *The science and engineering of microelectronic fabrication* (Oxford University Press, New York, 2001).

[8] M. J. Zaworotko, Chemical Society Reviews 23, 283 (1994).

[9] C. B. Murray, S. H. Sun, and F. X. J. Redl, Abstracts of Papers of the American Chemical Society 225, U74 (2003).

[10] Y. Lin, A. Boker, J. B. He, K. Sill, H. Q. Xiang, C. Abetz, X. F. Li, J. Wang, T. Emrick, S. Long, Q. Wang, A. Balazs, and T. P. Russell, Nature 434, 55 (2005).

[11] S. Gangopadhyay, G. C. Hadjipanayis, C. M. Sorensen, and K. J. Klabunde, Journal of Applied Physics 73, 6964 (1993).

[12] V. Skumryev, S. Stoyanov, Y. Zhang, G. Hadjipanayis, D. Givord, and J. Nogués, Nature (London, United Kingdom) 423, 850 (2003).

[13] R. Morel, A. Brenac, and C. Portemont, Journal of Applied Physics 95, 3757 (2004).

[14] C. L. Chang and H. S. Fogler, Langmuir 13, 3295 (1997).

[15] S. Link and M. A. Ei-Sayed, Annual Review of Physical Chemistry 54, 331 (2003).

[16] U. Kreibig and M. Vollmer, *Optical Properties of Metal Clusters. (Springer Series in Materials Science 25)*, 1995).

[17] M. A. El-Sayed, Accounts of Chemical Research 34, 257 (2001).

[18] C. R. Martin and D. T. Mitchell, Analytical Chemistry 70, 322A (1998).

[19] T. A. Taton, C. A. Mirkin, and R. L. Letsinger, Science 289, 1757 (2000).

[20] R. P. Van Duyne, Science 306, 985 (2004).

[21] C. B. Murray, C. R. Kagan, and M. G. Bawendi, Annual Review of Materials Science 30, 545 (2000).

[22] L. E. Brus, Journal of Chemical Physics 80, 4403 (1984).

[23] C. A. Leatherdale, W. K. Woo, F. V. Mikulec, and M. G. Bawendi, Journal of Physical Chemistry B 106, 7619 (2002).

[24] B. O. Dabbousi, J. RodriguezViejo, F. V. Mikulec, J. R. Heine, H. Mattoussi, R. Ober, K. F. Jensen, and M. G. Bawendi, Journal of Physical Chemistry B 101, 9463 (1997).

[25] R. G. Neuhauser, K. T. Shimizu, W. K. Woo, S. A. Empedocles, and M. G. Bawendi, Physical Review Letters 85, 3301 (2000).

[26] X. Michalet, F. Pinaud, T. D. Lacoste, M. Dahan, M. P. Bruchez, A. P. Alivisatos, and S. Weiss, Single Molecules 2, 261 (2001).
[27] M. Y. Han, X. H. Gao, J. Z. Su, and S. Nie, Nature Biotechnology 19, 631 (2001).
[28] S. Kim, Y. T. Lim, E. G. Soltesz, A. M. De Grand, J. Lee, A. Nakayama, J. A. Parker, T. Mihaljevic, R. G. Laurence, D. M. Dor, L. H. Cohn, M. G. Bawendi, and J. V. Frangioni, Nature Biotechnology 22, 93 (2004).
[29] W. J. Parak, D. Gerion, T. Pellegrino, D. Zanchet, C. Micheel, S. C. Williams, R. Boudreau, M. A. Le Gros, C. A. Larabell, and A. P. Alivisatos, Nanotechnology 14, R15 (2003).
[30] R. C. O'Handley, *Modern Magnetic Materials: Principles and Applications* (John Wiley & Sons, New York, 2000).
[31] S. Bucak, D. A. Jones, P. E. Laibinis, and T. A. Hatton, Biotechnology Progress 19, 477 (2003).
[32] M. F. Kircher, J. R. Allport, E. E. Graves, V. Love, L. Josephson, A. H. Lichtman, and R. Weissleder, Cancer Research 63, 6838 (2003).
[33] H. Lee, A. M. Purdon, and R. M. Westervelt, Ieee Transactions on Magnetics 40, 2991 (2004).
[34] S. A. Wolf, D. D. Awschalom, R. A. Buhrman, J. M. Daughton, S. von Molnár, M. L. Roukes, A. Y. Chtchelkanova, and D. M. Treger, Science (Washington, DC, United States) 294, 1488 (2001).
[35] X. F. Duan, Y. Huang, R. Agarwal, and C. M. Lieber, Nature 421, 241 (2003).
[36] C. M. Lieber, Mrs Bulletin 28, 486 (2003).
[37] J. Goldberger, D. J. Sirbuly, M. Law, and P. Yang, Journal of Physical Chemistry B 109, 9 (2005).
[38] M. Law, J. Goldberger, and P. D. Yang, Annual Review of Materials Research 34, 83 (2004).
[39] W. U. Wang, C. Chen, K. H. Lin, Y. Fang, and C. M. Lieber, Proceedings of the National Academy of Sciences of the United States of America 102, 3208 (2005).
[40] F. Dumestre, B. Chaudret, C. Amiens, M. C. Fromen, M. J. Casanove, P. Renaud, and P. Zurcher, Angewandte Chemie-International Edition 41, 4286 (2002).
[41] M. S. Dresselhaus, G. Dresselhaus, and P. C. Eklund, *Science of fullerenes and carbon nanotubes* (Academic Press, San Diego, 1996).
[42] A. Javey, J. Guo, Q. Wang, M. Lundstrom, and H. J. Dai, Nature 424, 654 (2003).
[43] R. J. Chen, S. Bangsaruntip, K. A. Drouvalakis, N. W. S. Kam, M. Shim, Y. M. Li, W. Kim, P. J. Utz, and H. J. Dai, Proceedings of the National Academy of Sciences of the United States of America 100, 4984 (2003).
[44] C. M. Niemeyer, Angewandte Chemie, International Edition 40, 4128 (2001).
[45] T. Mokari, E. Rothenberg, I. Popov, R. Costi, and U. Banin, Science 304, 1787 (2004).
[46] H. W. Gu, Z. M. Yang, J. H. Gao, C. K. Chang, and B. Xu, Journal of the American Chemical Society 127, 34 (2005).
[47] H. W. Gu, R. K. Zheng, X. X. Zhang, and B. Xu, Journal of the American Chemical Society 126, 5664 (2004).
[48] D. S. Wang, J. B. He, N. Rosenzweig, and Z. Rosenzweig, Nano Letters 4, 409 (2004).
[49] F. E. Osterloh, Journal of the American Chemical Society 124, 6248 (2002).

[50] V. L. Colvin, C. M. Sayes, K. D. Ausman, J. Fortner, and D. Lyons, Abstracts of Papers of the American Chemical Society 227, U1232 (2004).
[51] C. M. Sayes, J. D. Fortner, W. Guo, D. Lyon, A. M. Boyd, K. D. Ausman, Y. J. Tao, B. Sitharaman, L. J. Wilson, J. B. Hughes, J. L. West, and V. L. Colvin, Nano Letters 4, 1881 (2004).

Chapter 2

Introduction to magnetic materials and measurements

2.1: Introduction to magnetic materials

2.1.1: Origin of magnetism

Spin angular momentum usually dominates orbital angular momentum in determining the magnetic properties of a material. Materials in which all spins are paired are diamagnetic and generate a weak moment that opposes the direction of an applied field. When there are unpaired spins present that do not interact with those on adjacent atoms, the sample is paramagnetic, and the unpaired spins give rise to a moment that aligns parallel to the direction of an applied field. Paramagnetic effects dominate diamagnetic effects in magnitude.

When unpaired spins on adjacent atoms interact, they may have ferromagnetic, antiferromagnetic, or ferrimagnetic alignment. In the ferromagnetic case, the spins align parallel to one another, and their moments add. If the spins align antiparallel to each other, the moments cancel, and the material is antiferromagnetic. If there are two different sublattices aligned antiparallel to each other, then the material is ferrimagnetic. Ferromagnets (FMs) have an ordering temperature called the Curie (T_C) temperature, above which they are paramagnetic. Antiferromagnets (AFMs) have an analogous temperature, the Néel temperature (T_N), above which they are paramagnetic. Ferrimagnets have an analogous temperature, and some authors identify it as T_N [1], and others, as T_C [2]. (We use the T_N designation.)

The type of ordering is determined by the exchange interaction, which depends on orbital overlap. Neighbor-neighbor interactions are called direct exchange interactions, but longer-range, indirect exchange interactions mediated by the conduction electrons in metals, or by oxide ions between metal ions in a metal oxide, can also be important.

We consider the direct exchange between adjacent unpaired electrons on adjacent atoms. The wavefunctions for singlet and triplet configurations are:

$$\Psi_{\uparrow\uparrow} = \frac{1}{\sqrt{2}}\left[\psi_a(\mathbf{r}_1)\psi_b(\mathbf{r}_2) + \psi_a(\mathbf{r}_2)\psi_b(\mathbf{r}_1)\right]\chi_{\uparrow\uparrow}$$
$$\Psi_{\uparrow\downarrow} = \frac{1}{\sqrt{2}}\left[\psi_a(\mathbf{r}_1)\psi_b(\mathbf{r}_2) - \psi_a(\mathbf{r}_2)\psi_b(\mathbf{r}_1)\right]\chi_{\uparrow\downarrow} \qquad \textbf{(Eq. 2.1)}$$

The corresponding energies are:

$$E_{\uparrow\uparrow} = \int \Psi^*_{\uparrow\uparrow}\hat{H}\Psi_{\uparrow\uparrow}\,d\mathbf{r}_1 d\mathbf{r}_2$$
$$E_{\uparrow\downarrow} = \int \Psi^*_{\uparrow\downarrow}\hat{H}\Psi_{\uparrow\downarrow}\,d\mathbf{r}_1 d\mathbf{r}_2 \qquad \textbf{(Eq. 2.2)}$$

In order to determine which state is lower in energy, we take the difference in energies, which is related to the exchange integral, J:

$$E_{\uparrow\downarrow} - E_{\uparrow\uparrow} = 2\int \psi^*_a(\mathbf{r}_1)\psi^*_b(\mathbf{r}_2)\hat{H}\psi_a(\mathbf{r}_2)\psi_b(\mathbf{r}_1)d\mathbf{r}_1 d\mathbf{r}_2 = 2J \qquad \textbf{(Eq. 2.3)}$$

Therefore, if $J < 0$, then parallel alignment is more energetically favorable, and the material is ferromagnetic. If $J > 0$, then antiparallel alignment is preferred, and the material is antiferromagnetic or ferrimagnetic. The sign of J depends on the interatomic spacing and orbital filling and is determined by the Pauli exclusion principle, as well as the anti-symmetric nature of electron wavefunctions[1].

2.1.2: Domain formation

A region in a FM in which all of the atomic magnetic moments point in the same direction is called a magnetic domain. (Ferrimagnets and antiferromagnets also have domains in which all of the moments on one sublattice point in the same direction, and the moments on the other sublattice point in the opposite direction.) Although the exchange interaction favors the parallel configuration of adjacent moments in a FM, the size to which a single domain can grow in zero applied field is limited. The moments in a domain generate a dipolar field, which will tend to align adjacent moments in the opposite direction. Above a certain size (the single-domain limit), the sample is composed of multiple domains with their dipoles coupled because that configuration minimizes the total energy associated with the exchange and dipolar interactions better than a single domain would. The single-domain limit is material-dependent, and it depends on the relative strengths of the exchange interaction and the dipolar field. Despite this material-dependence, the sizes of the NPs studied in this thesis are sufficiently small to assume that they are single-domain NPs.

When a field is applied, the Zeeman energy of a moment in the applied field is:

$$E_Z = -\vec{\boldsymbol{\mu}} \cdot \vec{\mathbf{B}} \qquad \textbf{(Eq. 2.4)}$$

Therefore, if a field is applied to a sample that is composed of multiple domains, the domains that are parallel to the field direction will grow in order to minimize the Zeeeman energy.

2.1.3: Magnetocrystalline anisotropy

In FMs, AFMs, and ferrimagnets, the moments also interact with the crystal lattice. This interaction is called magnetocrystalline anisotropy. There are particular lattice directions along which it is more and less favorable for the moment to point. The more favorable directions are the "easy" axes, and less favorable directions are the "hard" axes. We consider HCP cobalt as an example of a uniaxial material, which has one easy axis, and a hard plane perpendicular to the easy axis. In order to rotate the moment from the easy axis to point in the opposite direction, it must be rotated through the hard plane. The energy required for this rotation is called the magnetocrystalline anisotropy energy (E_A). E_A is most accurately expressed as series that consists of many terms, but all terms except for the first one are typically neglected for NPs. E_A is expressed,

$$E_A = (K_1 \sin^2 \theta)V , \qquad \textbf{(Eq. 2.5)}$$

where θ is the angle between the moment and the easy axis. K_1 is called the first magnetocrystalline anisotropy constant, and when the higher order terms are neglected, it is often called K, the magnetocrystalline anisotropy constant.

2.1.4: Superparamagnetism

E_A can be on the order of k_BT in magnetic NPs due to their small volumes, but for $T < T_C$ (T_N) (depending on the material) the atomic moments in each NP continue to align parallel (or antiparallel for an AFM or ferrimagnet) to one another while their orientations fluctuate due to the thermal energy. This effect is called superparamagnetism because the moment of each NP behaves like a large paramagnetic moment.

The Brownian motion of a superparamagnetic NP moment as it fluctuates is modeled by the Néel-Brown model[3], which is similar to an Arrhenius treatment:

$$t = t_0 \exp\left(\frac{KV}{k_B T}\right), \qquad \textbf{(Eq. 2.6)}$$

where t is the mean time between flips at temperature T, and t_0 is a constant, which typically has a value of about 10^{-9}s [1]. The energy barrier used in **Eq. 2.6** is KV, which is the energy barrier obtained from **Eq. 2.5** when the moment is rotated through the hard plane. The magnetization process of a superparamagnet obeys a Langevin function, which is described in Appendix **C**.

2.2: Magnetic measurements

Magnetic measurements may be performed in a variety of magnetometers. In this thesis, we used a superconducting quantum interference device (SQUID) magnetometer, which measures sensitive changes in the magnetic flux in a pickup coil as the sample is moved through it. The SQUID magnetometer is cooled with liquid He and can attain a minimum temperature of about 2 K.

2.2.1: Temperature-dependent magnetization: blocking temperature

Measurements of M vs. T in a small applied field are performed on magnetic NPs in order to observe the transition between ferromagnetism (ferrimagnetism) and superparamagnetism. The sample is cooled in zero field to low temperature, and then a small measuring field (0.01 T in our case) is applied. The sample is measured as it is heated in the small field. (In a related measurement, the field cooled M vs. T, the sample is cooled in the same small measuring field, rather than in zero field.)

During the zero field cooled experiment, the sample is ferromagnetic at low temperatures, and the magnetocrystalline anisotropy energy is greater than the Zeeman energy that would favor orienting the NPs into the field. Thus, there is little orientation into the field direction, and a low moment is measured. As the sample is heated, the thermal energy helps the moments overcome the magnetocrystalline anisotropy energy, and they become superparamagnetic. Although the NP moments fluctuate, there is a greater mean component of the fluctuations in the applied field direction, which causes the magnetization to increase when the NPs become superparamagnetic. As the temperature is raised further, the component of the fluctuations in the applied field direction decreases (in accordance with the Langevin behavior of paramagnets), and the magnetization decreases. Therefore, there is a peak in the magnetization at the temperature at which the NPs become superparamagnetic. This temperature is called the blocking temperature (T_B). T_B is measured experimentally as the peak in the real component of the magnetic susceptibility (χ') vs. T for AC measurements, or in M vs. T at small applied field in DC measurements. (Since the applied field is small, the DC M vs. T curve serves as a linear approximation of the DC susceptibility, if the values of M are divided by the applied field.)

In order to compare the Néel-Brown model with SQUID measurements, we ask the question: Using a measurement frequency of ω, at what temperature will ω be the mean flip frequency? That is, at what T is $\omega = 1/t$, where t is obtained from (**Eq. 2.6**)? The blocking temperature from experiments can be compared with the Néel-Brown model by substituting it into **Eq. 2.6** and solving for it:

$$T_B = \frac{KV}{\ln(t/t_0)k_B} \qquad \textbf{(Eq. 2.7)}$$

For DC measurements, a value of t = 100 s is typically used. If the NPs are to be applied in magnetic recording, then a more stringent requirement must be satisfied, which is $KV \geq$ 50-70 k_BT [4].

Antiferromagnets can also exhibit superparamagnetism if $T_B < T_N$. However, this measurement technique does not apply to antiferromagnets because they have no net moment (or a very small net moment when there are an odd number of lattice planes), which makes observations of the magnetic behavior of anitferromagnets intrinsically more challenging than for FMs or ferrimagnets.

2.2.2: Thermal remanent magnetization

Thermal remanent magnetization (TRM) is a similar measurement to the field-dependent magnetization. The sample is cooled in a field, which can be of small or large magnitude, and after the field is switched off at low temperature, M vs. T is measured during heating. If the cooling field was sufficiently high, the NP moments are initially frozen at low temperature with their moments pointing along easy axes in orientations near to the direction of the cooling field because the magnetocrystalline anisotropy energy is greater than the thermal energy. This value of the magnetization at zero field is called the remanence or remanent magnetization. As the sample is heated, the thermal energy begins to exceed the magnetocrystalline anisotropy energy, and the magnetization decays to zero as the NPs become superparamagnetic, since there is no applied field.

2.2.3: Field-dependent magnetization: history is important

M vs. *H* measurements are useful for characterizing ferromagnetic (ferrimagnetic) samples. A typical *M* vs. *H* curve is shown schematically in **Fig. 2.1**. The field is usually scanned up to the highest available field in the magnetometer. If the curve flattens at high field, the magnetization has reached a maximum value, called the saturation magnetization (M_S). As the field is decreased to zero, the magnetization decreases to the remanence (M_R). When the field is applied in the negative direction, the magnetization eventually decreases to zero. The magnitude of the field at which this occurs is called the coercive field or coercivity (H_C). Eventually, the field is saturated in the negative direction, and the process that occurs as the field is increased is analogous to the case when the field is decreased.

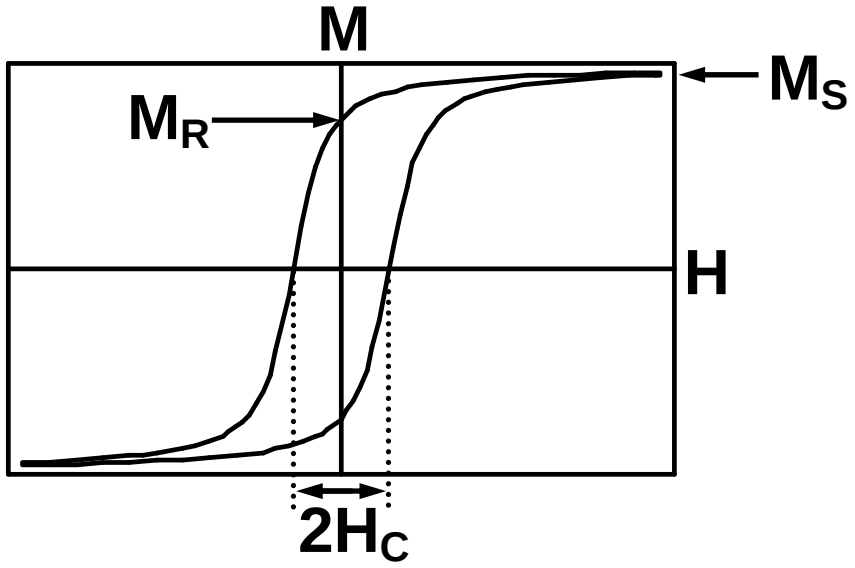

Fig. 2.1: Schematic *M* vs. *H* curve of a FM

If we choose a field and wish to know the magnetization, we must also know the history of the sample, since each field value in the plot corresponds to two magnetizations. This property is called hysteresis. As the sample is heated, H_C decreases, and the two curves collapse into one. That happens when the sample becomes superparamagnetic because the thermal fluctuations erase each NP's memory of its history.

Measurements of single-domain NPs and multiple-domain samples both look similar to the one depicted in **Fig 2.1**. The field-dependent magnetization of single-domain NPs has been modeled in greater detail using the Stoner-Wohlfarth model[1]. H_C depends on the NP size as well as the temperature. When the moment of a small single-domain NP switches (and fluctuates in the superparamagnetic regime), all of the atomic moments rotate coherently. Larger single-domain NPs may switch through other mechanisms, such as the temporary introduction of a domain wall, even though the NPs are still single-domain in zero applied field. H_C reaches a maximum at the largest NP size that switches by coherent rotation[1].

2.3: Exchange bias

When a sample containing an interface between a FM (or ferrimagnet) and an AFM (or ferrimagnet) is cooled in a magnetic field, it may exhibit an additional unidirectional anisotropy due to magnetic coupling at the interface. This effect, called exchange biasing (EB), was first discovered nearly 50 years ago in oxidized Co NPs (NPs)[5]. EB has been observed in many other magnetic materials, and vigorous experimental and theoretical research on EB continues. Although much progress has

been made, the microscopic mechanism of EB still is not completely understood. Exchange biased materials have important technological applications, such as in giant magnetoresistance based spin valves that are used in hard drive read heads; other spintronics applications, such as magnetic random access memory, are under development[6]. For additional background on EB, we refer to recent reviews[7-10].

Some general features of EB are an enhancement of H_C over a sample that was cooled in zero field, and a shift of the M vs. H loop along the field axis in the direction opposite to that of the applied cooling field, which is called the exchange shift (H_{EB}). A schematic M vs. H curve for an exchange biased FM that was cooled in a positive field is shown in **Fig. 2.2**. The sign convention usually used for H_{EB} is that a shift along the negative field direction has a positive value, so that cooling in a positive field gives rise to a positive H_{EB}.

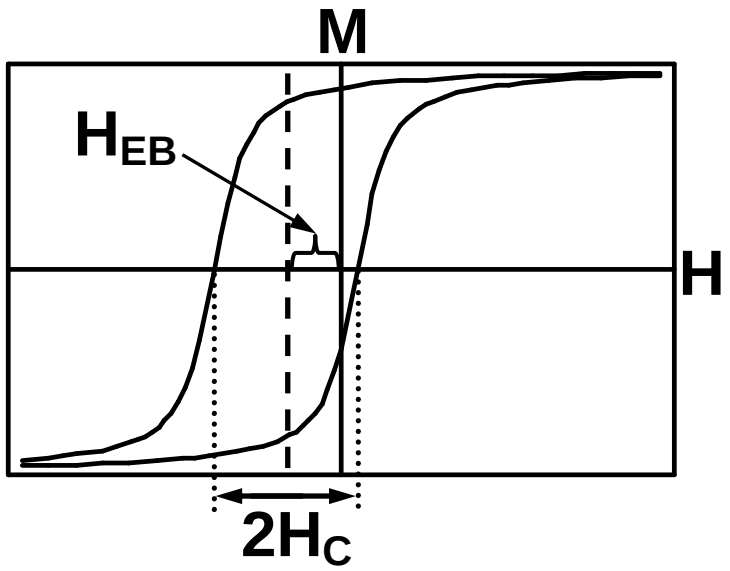

Fig. 2.2: Schematic M vs. H curve of an exchange biased FM after cooling in a positive field

EB originates from the exchange coupling between the moments in the FM and AFM. EB can only arise if the sample is cooled from above $T_{B,\,AFM}$ or T_N of the AFM. As the sample is cooled through T_N, the moments in the AFM couple to one another, but the AFM may still be superparamagnetic. As the AFM cools below $T_{B,\,AFM}$, the moments freeze in the lattice. Since a field is applied during cooling, the FM is oriented in the field direction. After cooling, the AFM tends to pin the FM in the same orientation in which it was cooled. This pinning effect is the unidirectional anisotropy of EB, which causes the *M* vs. *H* curve in **Fig. 2.2** to shift so that a positive magnetization is preferred.

The energies associated with this unidirectional anisotropy are depicted schematically in **Fig. 2.3** for a NP with a FM core and an AFM shell. In this example, the FM core has a uniaxial magnetocrystalline anisotropy with an easy axis pointing along the page horizontally ($\theta = 0$ and $\theta = \pi$, along the easy axis). The NP is cooled in a field pointing to the right ($\theta = 0$). In **Fig. 2.3a**, $T > T_N$, and when the field is switched to rotate the moment to $\theta = \pi$, the energy increases as the magnetization rotates through the hard plane, and then the energy minimum for $\theta = \pi$ is the same as for $\theta = 0$. These states are degenerate because the AFM is paramagnetic and is unable to pin the core and cause EB. In **Fig. 2.3b**, $T < T_N$ and $T < T_{B,AFM}$, and the AFM pins the core. The orientation in the direction of the initial cooling field is energetically favored. The arrows in the shell AFM in **Fig. 2.3b** indicate the direction in which the AFM pins the core FM; the arrows do not depict the microscopic structure of the atomic magnetic moments in the AFM. In **Fig. 2.3a**, the arrows point in all directions to represent paramagnetism and no pinning interaction.

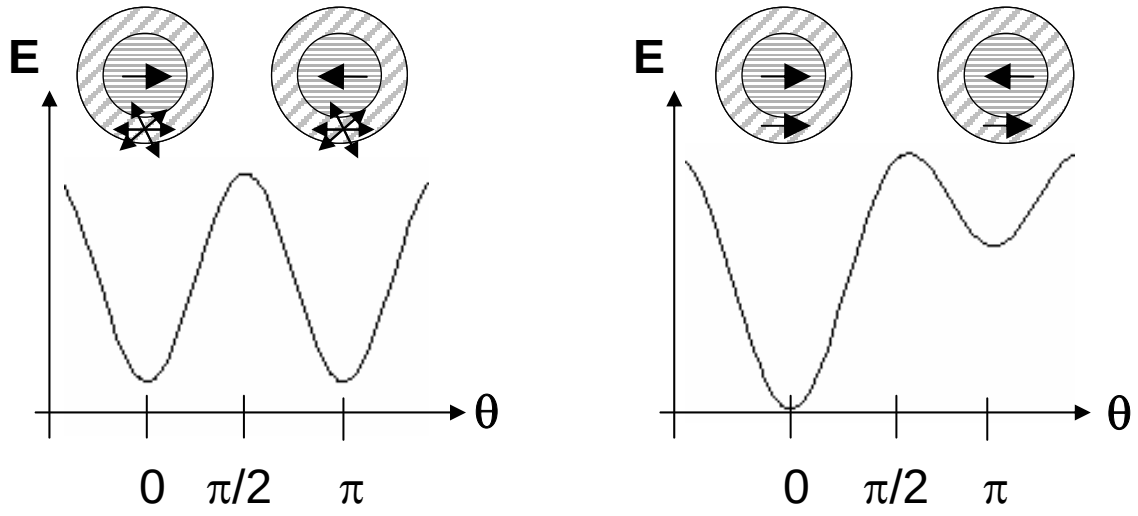

(a) $T > T_N$ **(b)** $T < T_N$ **and** $T < T_{B,AFM}$

Fig. 2.3: Schematic energy diagram of a FM(core)/AFM(shell) NP showing **(a)** no EB and **(b)** EB. The FM core has a uniaxial magnetocrystalline anisotropy with an easy axis pointing along $\theta = 0$ and $\theta = \pi$.

2.4: Choice of materials

The properties of many magnetic materials are listed in Table **2.1**. The table is incomplete because some of the data are difficult to find and are not needed for this thesis. Ni has a lower saturation magnetization than Fe, but Fe oxidizes quickly in air. Co has high magnetocrystalline anisotropy and a hexagonal phase, which is what originally made it of interest in our research group[11, 12]. However, cobalt oxidizes in air and is not water-stable. Iron has a variety of oxides with interesting magnetic properties[13]. Maghemite and magnetite are useful for biological applications like magnetic resonance imaging[14] because of their biocompatibility and their stability in water and air. The face-centered tetragonal phase (FCT) of FePt is also of great interest

because of its high magnetocrystalline anisotropy. However, the FCT phase is usually obtained by annealing the FCC phase, which leads to sintering and agglomeration[15-17]. Both phases of FePt are air-stable. Because of the high magnetocrystalline anisotropy and thereby high H_C of the FCT phase of FePt, it is a candidate for high-density magnetic recording media.

Material	Magnetic Structure	Structure	M_S (emu/g)	μ_B (per Fe, Co, Ni atom)	T_C/T_N (K)	K (J/m^3)
Fe	ferromagnetic	BCC	221	2.2	1043	4.8 x 10^4
Co	ferromagnetic	HCP	162	1.7	1388	4.1 x 10^5
Co	ferromagnetic	FCC	162	1.7	1388	-7 x 10^4 [18]
CoO	antiferromagnetic	rocksalt	0	3.8 [19]	290 [20]	
Ni	ferromagnetic	FCC	57	0.6	627	-4.5 x 10^3
FeO (wustite)	antiferromagnetic	rocksalt	0	4		
γ-Fe_2O_3 (maghemite)	ferrimagnetic	metastable defect spinel	74	2.5	863-945	~(1-4) x 10^4 [21]
Fe_3O_4 (magnetite)	ferrimagnetic	spinel	84	1.4	850	
α-Fe_2O_3 (hematite)	antiferromagnetic	corundum (hexagonal)	0	2.5		
FePt	ferromagnetic	FCC				~ 1 x 10^5 [22]
FePt	ferromagnetic	FCT		3.4 [23]		7 x 10^6 [24]

Table 2.1: Magnetic properties for a variety of transition metals and metal oxides. Except where otherwise noted, all data are from reference [1].

2.5: Thesis overview

The main topic of this thesis is a study of the magnetic properties of Co NPs with different extents of oxidation, which begins in Chapter **3**. EB in partially oxidized Co NPs is also reported and discussed. The magnetic properties of defect moments in the CoO shell of oxidized NPs and their effect on EB are reported in Chapter **4**. The remaining chapters cover preliminary work in a few different areas: The preparation and

magnetic properties of γ-Fe_2O_3 NPs are reported in Chapter **5**, along with a method for incorporating them into silica microspheres along with CdSe QDs. Trapping of these magnetic and highly luminescent microspheres on a microelectromagnetic device is demonstrated and discussed. The preparation and magnetic properties of FePt NPs are described in Chapter **6**. TEM results show that FePt NPs may fuse together in solution. Methods for functionalizing commercially available Co NPs and their magnetic properties are discussed in Chapter **7**. Appendix **G** is a guide for performing transmission electron microscopy on NPs using the microscopes in the CMSE at MIT.

2.6: References

[1] R. C. O'Handley, *Modern Magnetic Materials: Principles and Applications* (John Wiley & Sons, New York, 2000).

[2] C. M. Sorensen, in *Nanoscale Materials in Chemistry*, edited by K. J. Klabunde (Wiley-Interscience, New York, 2001), p. 169.

[3] W. F. Brown, Physical Review 130, 1677 (1963).

[4] D. Weller, A. Moser, L. Folks, M. E. Best, W. Lee, M. F. Toney, M. Schwickert, J. U. Thiele, and M. F. Doerner, Ieee Transactions on Magnetics 36, 10 (2000).

[5] W. H. Meiklejohn and C. P. Bean, Physical Review 105, 904 (1957).

[6] S. A. Wolf, D. D. Awschalom, R. A. Buhrman, J. M. Daughton, S. von Molnár, M. L. Roukes, A. Y. Chtchelkanova, and D. M. Treger, Science (Washington, DC, United States) 294, 1488 (2001).

[7] A. E. Berkowitz and K. Takano, Journal of Magnetism and Magnetic Materials 200, 552 (1999).

[8] J. Nogués and I. K. Schuller, Journal of Magnetism and Magnetic Materials 192, 203 (1999).

[9] M. Kiwi, Journal of Magnetism and Magnetic Materials 234, 584 (2001).

[10] R. L. Stamps, Journal of Physics D: Applied Physics 33, R247 (2000).

[11] D. P. Dinega and M. G. Bawendi, Angewandte Chemie, International Edition 38, 1788 (1999).

[12] D. P. Dinega and Massachusetts Institute of Technology. Dept. of Chemistry., 2001).

[13] F. X. Redl, C. T. Black, G. C. Papaefthymiou, R. L. Sandstrom, M. Yin, H. Zeng, C. B. Murray, and S. P. O'Brien, Journal of the American Chemical Society 126, 14583 (2004).

[14] M. F. Kircher, J. R. Allport, E. E. Graves, V. Love, L. Josephson, A. H. Lichtman, and R. Weissleder, Cancer Research 63, 6838 (2003).

[15] T. Thomson, M. F. Toney, S. Raoux, S. L. Lee, S. Sun, C. B. Murray, and B. D. Terris, Journal of Applied Physics 96, 1197 (2004).

[16] T. J. Klemmer, C. Liu, N. Shukla, X. W. Wu, D. Weller, M. Tanase, D. E. Laughlin, and W. A. Soffa, Journal of Magnetism and Magnetic Materials 266, 79 (2003).

[17] H. Zeng, S. H. Sun, T. S. Vedantam, J. P. Liu, Z. R. Dai, and Z. L. Wang, Applied Physics Letters 80, 2583 (2002).

[18] T. Suzuki, D. Weller, C. A. Chang, R. Savoy, T. Huang, B. A. Gurney, and V. Speriosu, Applied Physics Letters 64, 2736 (1994).

[19] W. L. Roth, Physical Review 110, 1333 (1958).

[20] K. Takano, R. H. Kodama, A. E. Berkowitz, W. Cao, and G. Thomas, Physical Review Letters 79, 1130 (1997).

[21] S. Morup and E. Tronc, Physical Review Letters 72, 3278 (1994).

[22] B. Stahl, J. Ellrich, R. Theissmann, M. Ghafari, S. Bhattacharya, H. Hahn, N. S. Gajbhiye, D. Kramer, R. N. Viswanath, J. Weissmuller, and H. Gleiter, Physical Review B 67 (2003).

[23] A. B. Shick and O. N. Mryasov, Physical Review B 67 (2003).

[24] S. Sun, C. B. Murray, D. Weller, L. Folks, and A. Moser, Science (Washington, D. C.) 287, 1989 (2000).

Chapter 3

Systematic study of exchange biasing in cobalt nanoparticles with different extents of oxidation

3.1: Introduction

About 5 years ago, Co NPs were of interest for their potential application in magnetic recording[1-3]. However, over the last 5 years, much attention has shifted away from Co NPs and to FePt NPs[4-7] because FePt has a magnetocrystalline anisotropy that is much greater than Co and does not oxidize in air. It is well-known that Co NPs oxidize in air, and Dinega showed an unusual *M* vs. *T* curve for partially oxidized Co NPs in his thesis[8], but the effects of the surface oxide on the magnetic properties were not thoroughly investigated. In this chapter, we report a systematic investigation of the magnetic properties of Co NPs with different extents of oxidation. Shortly after we began this work about two years ago, the magnetic properties of Co NPs embedded in a bulk CoO matrix were reported[9], and in this study, we report the effects of a finite-thickness oxide that is prepared using a different method.

The interface between Co (FM) and CoO (AFM) has been used as a prototype for studying EB because it has a large unidirectional anisotropy, and T_N for bulk CoO is near room temperature at 293 K[10]. Exchange biased Co/CoO interfaces have been investigated in thin films[11] and NPs prepared using cluster-beam deposition[12], chemical vapor deposition[13], sputtering[9, 14], and also colloidal methods[15, 16]. Colloidal Co NPs can be economically prepared using wet chemical methods with a high level of control over

NP size and crystal structure[1-3, 17-20]. NP surface functionalization can be well controlled and exploited to manipulate[21] and assemble NPs[1, 3, 22] in ways that are not possible for particles prepared using physical methods. In particular, surface ligands control particle solubility, prevent agglomeration, and can provide functional groups for further chemistry on the NP surface.

Colloidal Co NPs with three extents of oxidation were investigated: The native sample has a thin (1.0 nm) CoO shell and exhibits no exchange biasing. The purposefully partially oxidized sample has a thicker CoO shell (3.2 nm), and is exchange biased. The sample fully oxidized to CoO looses exchange biasing. We observe three distinct magnetic properties that result from the finite-thickness antiferromagnet shell exchange coupled to a finite-size ferromagnet core, and from crystal and stoichiometric defects: (1) an enhancement of the thermal stability of the orientation of the magnetic moment due to exchange biasing in the partially oxidized sample, (2) a low temperature paramagnetic response in the partially and fully oxidized samples due to defects in the CoO shell, and (3) an asymmetry in the field-dependent magnetization for the partially oxidized sample at low temperature due to small clusters of Co in a diffusion layer around the Co core.

3.2: Experimental

3.2.1: Preparation of systematically oxidized cobalt nanoparticles

All of the NPs used in this study were prepared in the same batch in order to eliminate size variations among different batches. Co NPs were prepared as follows: In an inert atmosphere, 0.55 g $Co_2(CO)_8$ (Strem) was dissolved in 16 mL dioctyl ether

(TCI). This solution was injected into a solution of 0.10 mL trioctlyphosphine (Strem, 97%) in 19 mL dioctyl ether at 235 ˚C. Following injection, the solution was heated at 180 ˚C for 10 minutes. The NPs began to aggregate, and 0.14 g stearic acid (Aldrich, 98%) was added. The mixture was then heated for another 10 minutes at 180 ˚C, which dispersed the NPs. A similar procedure for making smaller Co NPs (2-3 nm diameter) is described in Appendix **A**.

Inside a glovebox, the NPs were precipitated by adding ethanol. After centrifuging (3900 RPM for 2 minutes) and discarding the supernatant, they were redispersed in hexanes. After centrifuging again (3900 RPM for 2 minutes), the solids were discarded. Ethanol was added to the hexanes solution to precipitate the NPs, and after centrifuging, (3900 RPM for 2 minutes) and discarding the supernatant, the NPs were redispersed in tetrahydrofuran (THF). They could be stored indefinitely in a nitrogen glovebox, but were found to have slightly oxidized. We identify this as the "native" sample. The "partial" sample was purposefully partially oxidized by bubbling air through a solution of the native sample for 5 minutes and then waiting 6 weeks. To prepare the "full" sample, which was fully oxidized to CoO, the NPs were transferred back into dioctyl ether and heated while bubbling air through the solution at 100 ˚C for 28 hours.

3.2.2: Incorporation into polymer sticks

After each extent of oxidation, some NPs were dispersed in poly(lauryl methacrylate) cross-linked with ethyleneglycol dimethacrylate[23]. In order obtain polymer sticks that are solid yet not too brittle, we prepared a monomer solution that was 83%

lauryl methacrylate and 17% ethylene glycol by mass. As an initiator, 0.40% (by mass) 2,2'-azobisisobutyronitrile (AIBN) was added. This amount of initiator was chosen in order to lead to complete polymerization without producing bubbles in the sample.

Under vacuum, the solvent was removed from 0.5-1.0 mL of the concentrated NP solution in THF. After adding 0.5-1.0 mL of the monomer solution, the sample was sonicated for a few minutes, until the NPs redispersed. The solution was transferred to a new glass vial, and was then placed in an oven set at 120 °C for 5 minutes. After cooling, the vial was broken open, and the polymer stick was retrieved. Photographs of the polymer sticks with and without NPs are shown in Fig. **3.1.**

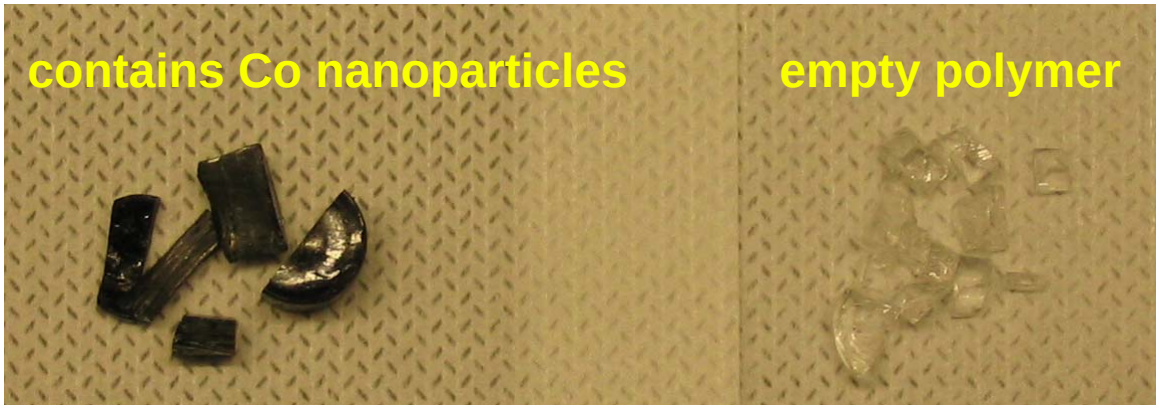

Figure 3.1: Polymer sticks, empty (right) and containing oxidized Co NPs (left)

The NP concentration was chosen to be dilute so that the average interparticle distance was greater than 70 nm, a distance at which dipolar coupling between NPs is negligible. A microtomed slice of one of the polymer sticks is shown in **Fig. 3.2**. The slice thickness was chosen to be 20-40 nm. There appears to be some aggregation in the

polymer, but even at relatively close distances, the NPs are not significantly interacting. Justification that the NPs are not significantly interacting is given in Appendix **B**.

The NP/polymer samples were stored in a nitrogen glovebox when they were not being measured in order to prevent further oxidation. Elemental analysis was performed on each polymer sample by Galbraith Laboratories, Inc., using inductively coupled plasma – optical emission spectroscopy.

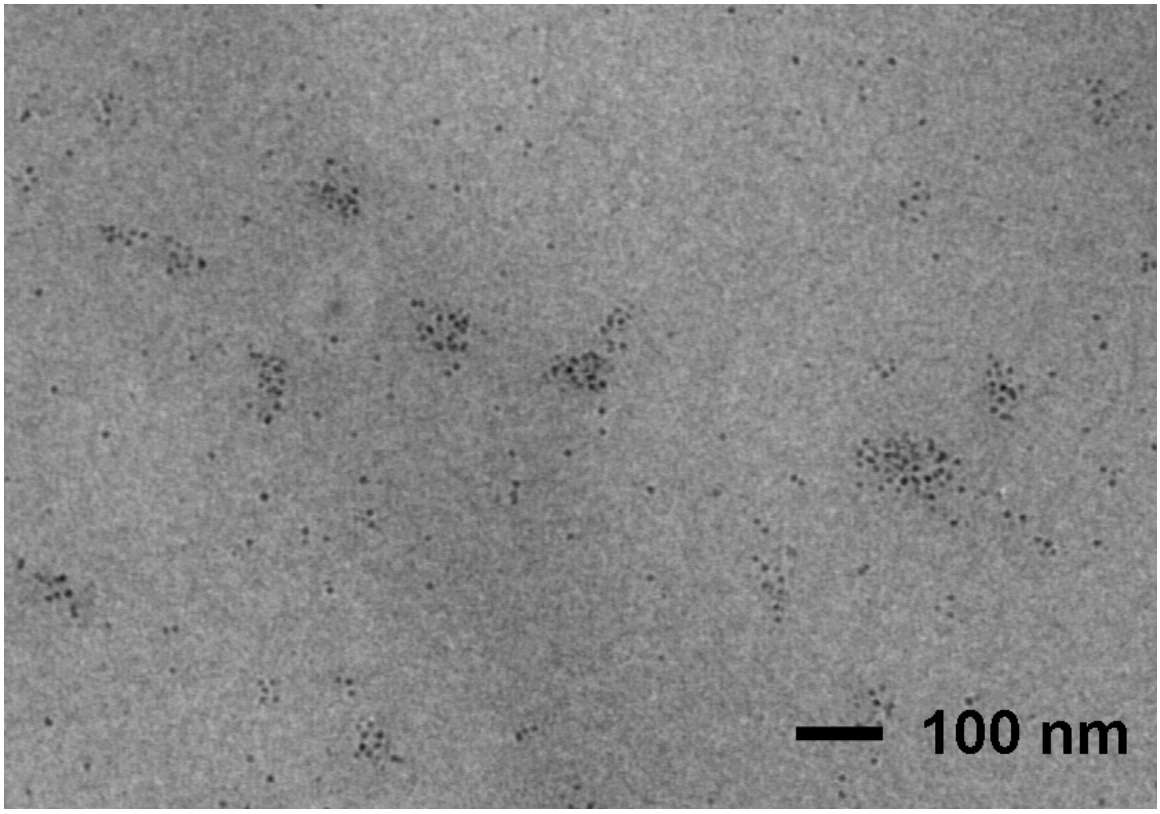

Figure 3.2: TEM of microtomed polymer stick containing oxidized Co NPs

3.3: Transmission electron microscopy investigation

Transmission electron microscopy (TEM) was performed on a JEOL 2000 FX microscope, and high resolution TEM (HRTEM) was performed on a JEOL 2010. TEM images of the native NPs (**Fig. 3.3a**) show that they have a diameter of 7.8 nm with a standard deviation of 1.0 nm. They are polycrystalline FCC with many defects, as seen in the "speckled" contrast in each NP. Partially oxidized NPs (**Figs. 3.3b and 3.4**) are polycrystalline, but individual crystalline grains are resolvable. HRTEM micrographs show that these partially oxidized NPs are composed of grains of about 3 nm in diameter. Typically, there are one or two central grains surrounded by 4-7 grains in each NP. Many of the partially oxidized NPs show darkened cores, rather than the random distribution of

dark spots that was observed for the native sample. These TEM images are similar to those in another study of partially oxidized NPs[24].

The fully oxidized NPs (**Fig. 3.3c**) are polycrystalline and hollow, which is consistent with a similar recent study performed on single-crystal ε-Co NPs[25]. The outer diameter of the NPs has increased to accommodate the hollow cavity and the volume expansion as oxygen was incorporated into the NPs. Using electron diffraction **(Fig. 3.5)**, the crystal structure of the oxide phase after heating in air was verified to be CoO. A more thermodynamically stable oxide phase is Co_3O_4, but a higher heating temperature is generally required to prepare it[26]. CoO has a rock salt crystal structure, whereas Co_3O_4 is spinel. Each ring is assigned to CoO as follows: A ~ <111>; B ~ <200>; C ~ <220>; D ~ <311> and <222>; E ~ <400>; F ~ <331> and <420>; G ~ <422>. No additional rings were observed. If the sample were Co_3O_4, no <200>, <331>, and <420> reflections would be observed, but these reflections were observed and are attributed to CoO. Furthermore, if a significant amount of Co_3O_4 were present, its <111> and <220> planes would give rise to rings inside of A, but because no rings were observed inside of A, the absence of the <111> and <220> reflections also shows that Co_3O_4 is not significantly present.

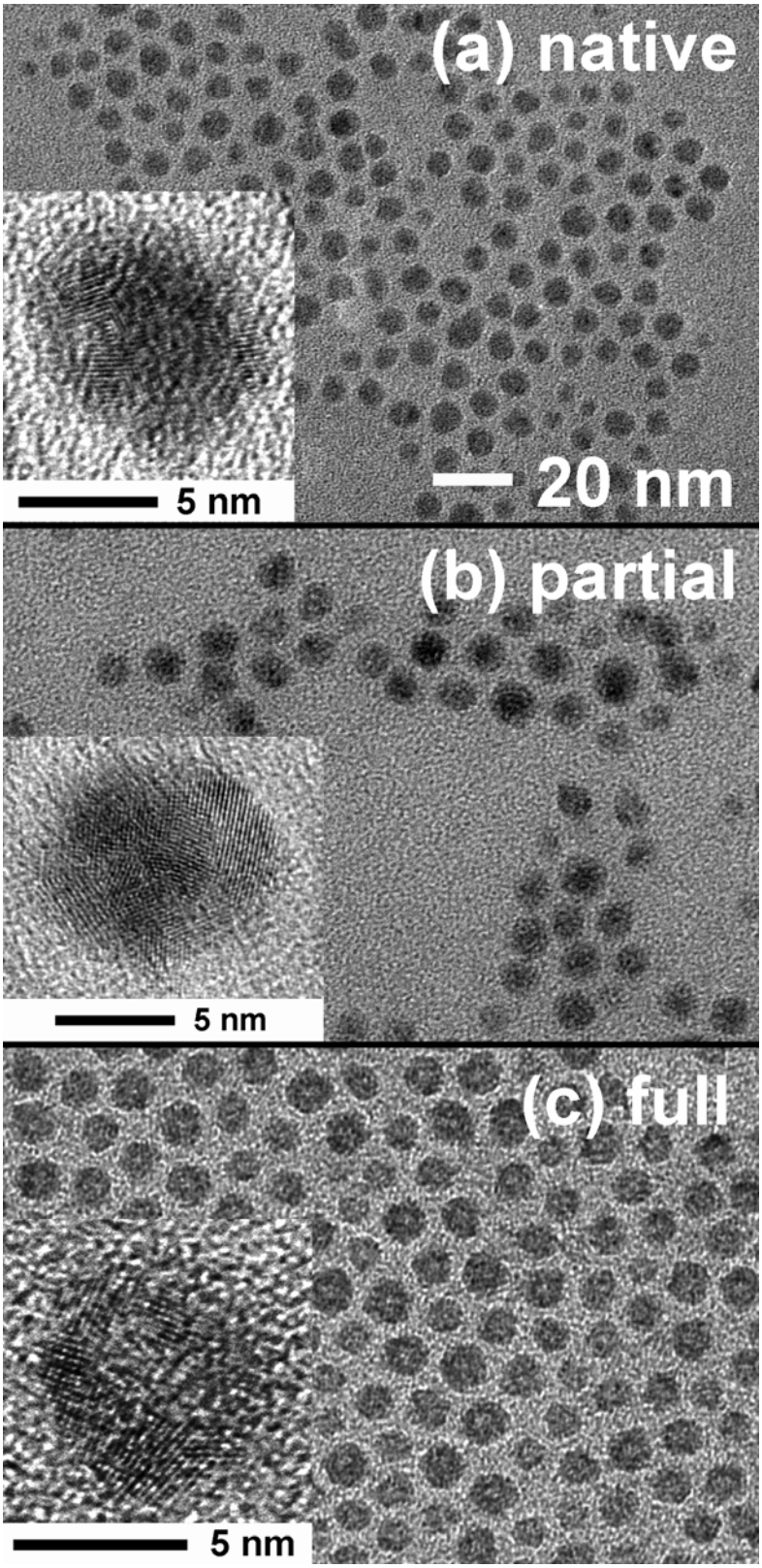

Figure 3.3: TEM and HRTEM (insets) of Co NPs with **(a)** native, **(b)** partial, and **(c)** full oxidation

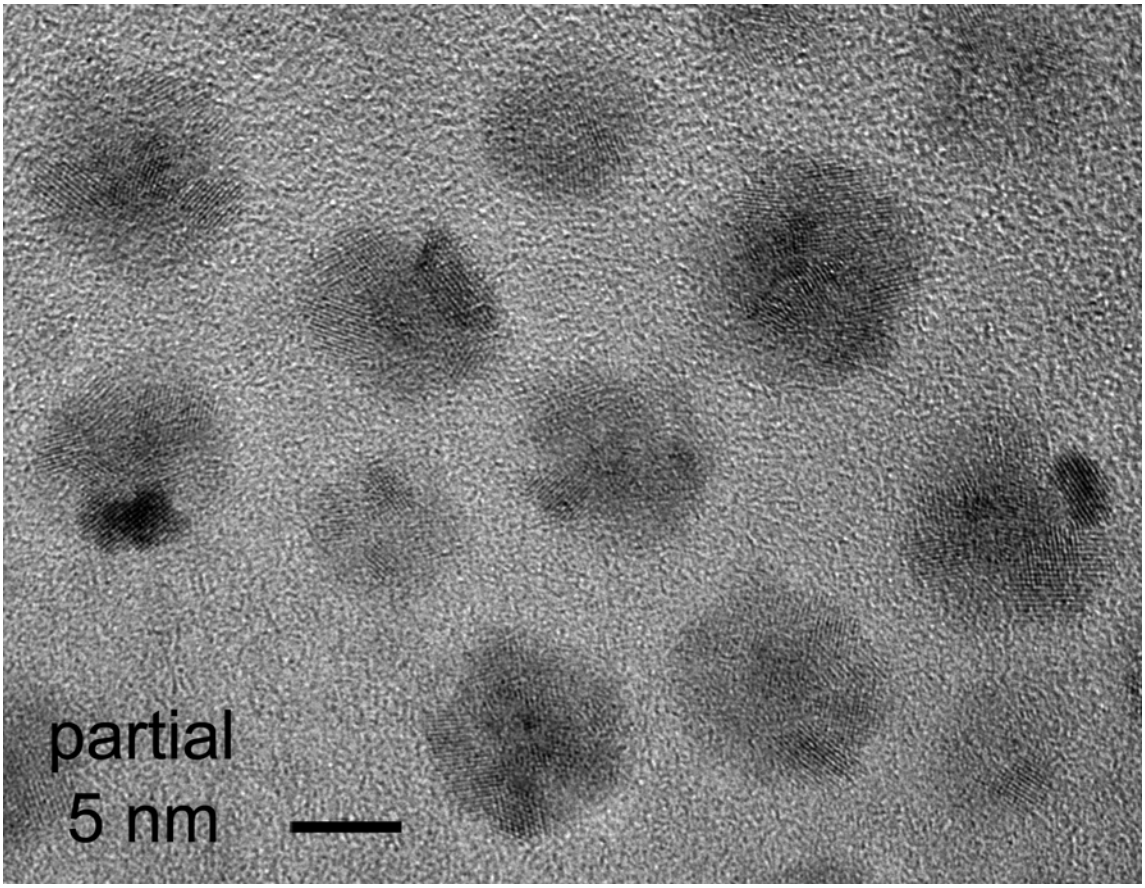

Figure 3.4: HRTEM of partially oxidized Co NPs

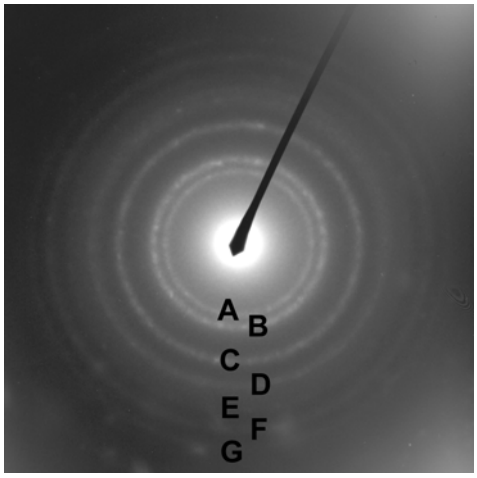

Figure 3.5: Electron diffraction micrograph of full sample

3.4: Magnetic data: results and discussion

SQUID measurements were performed on a Quantum Design MPMS-5S. In the field-dependent magnetization measurements, a correction was made to remove the diamagnetic background of the polymer. Reference *M* vs. *H* curves for a piece of the empty polymer (m = 0.0429 g) are shown in **Fig. 3.6**. As expected, the *M* vs. *H* curves are linear, and the susceptibility (χ) is the slope of each line. The slope at 5 K gives χ_{5K} = -1.430 x 10^{-4} emu/(g·T). For $T \geq 50$ K, χ = -1.704 x 10^{-4} emu/(g·T). For 5 K > T > 50 K, an interpolated value of χ was used for the polymer background correction.

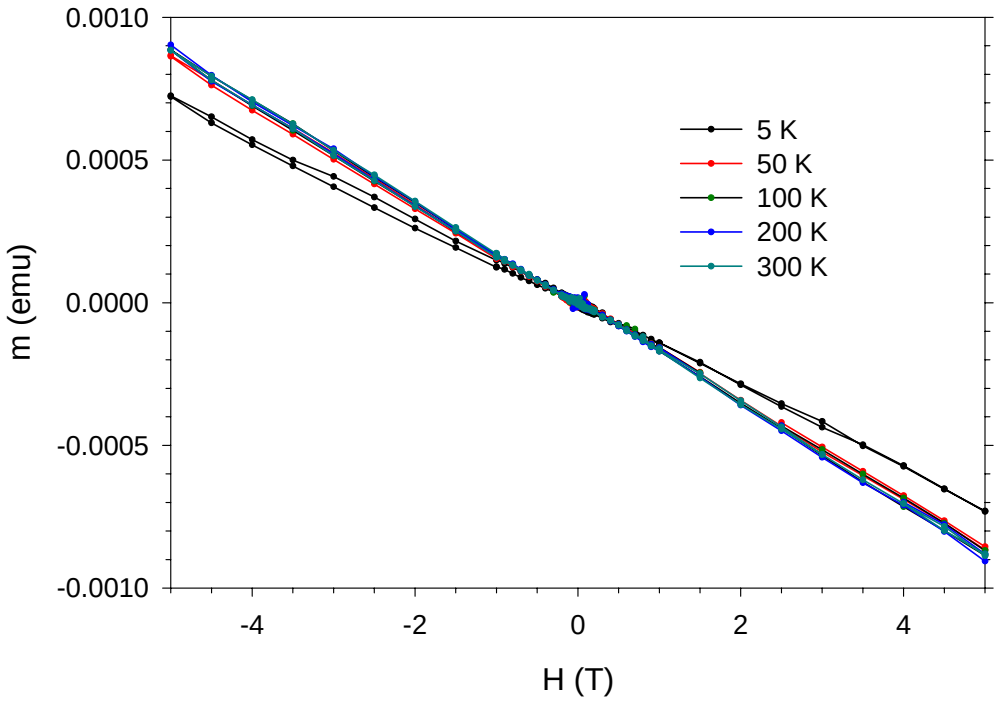

Figure 3.6: *M* vs. *H* of an empty polymer sample of mass 0.0429 g at a variety of temperatures.

The magnetization units of emu/g reported in this chapter and the next are based on the mass of cobalt. The mass of ligands and oxygen in the oxidized samples is excluded.

3.4.1: Oxide thickness, magnetocrystalline anisotropy constants, and increased blocking temperature due to exchange biasing

The *M* vs. *H* curves for native NPs after cooling in a 5 T field (**Fig. 3.7a**) exhibit no exchange shift (H_{EB}). Although the Co cores are highly polycrystalline, they are too small to sustain domain walls and are single domain magnets. We note that at high fields, the *M* vs. *H* curves for native NPs do not exactly overlap, and an additional component with positive slope that is greatest at low temperature is observed, which is caused by the susceptibility of the CoO shell (**Fig. 3.7b**). We used the *M* vs. *H* curves for fully oxidized NPs to subtract the component of the temperature-dependent susceptibility of CoO, with which we calculated that M_S in the native sample is 91 emu/g. This value of M_S is 56 % of the bulk magnetization for Co (162 emu/g) [27]. Although interactions with carboxylate ligands that are chemisorbed[28] on the surface and residual CO from the NP preparation could reduce M_S[18, 29-31] below the bulk value, these effects cannot explain such a large reduction, and we conclude that the reduction in M_S must be primarily caused by the formation of a thin layer of CoO on the surface of our native NPs, the thickness of which we measure later in this chapter.

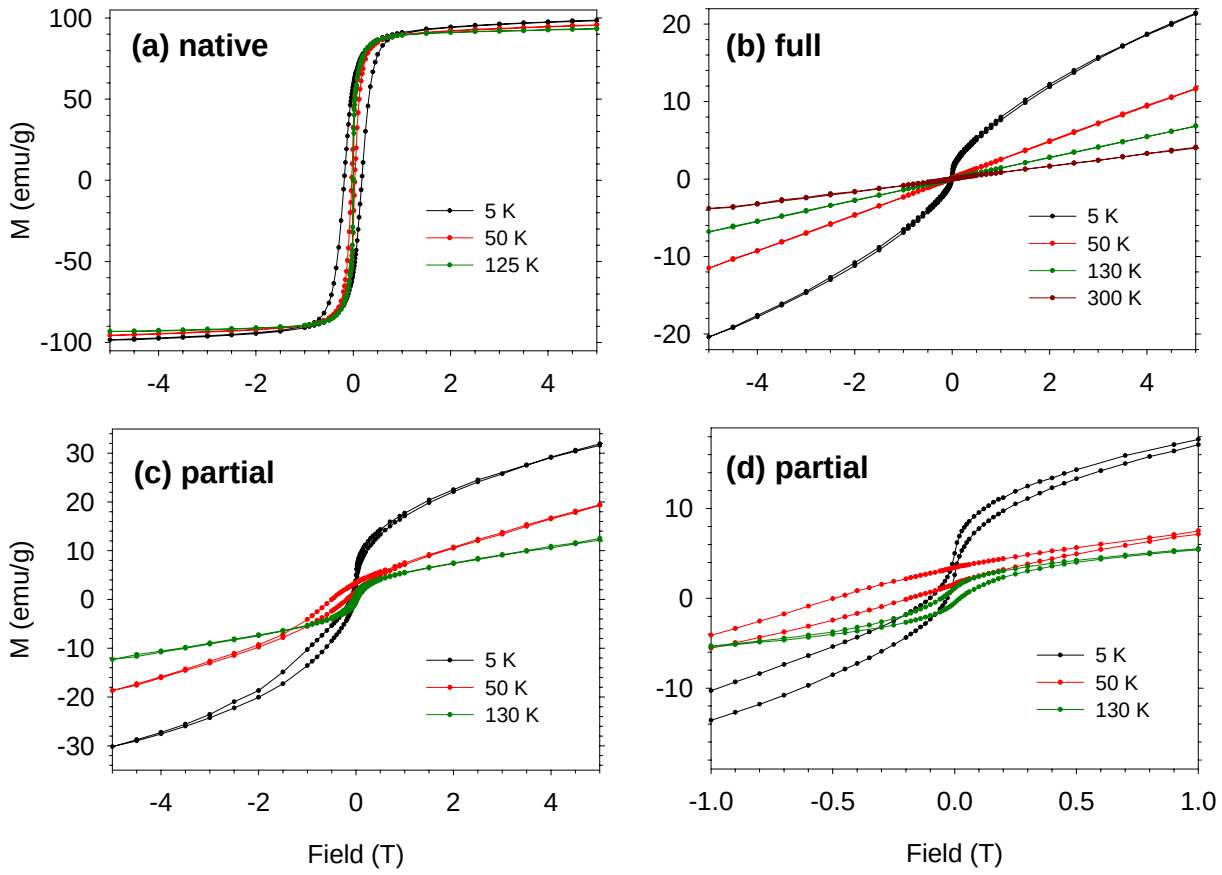

Figure 3.7: Co NPs with **(a)** native, **(b)** full and **(c-d)** partial oxidation: *M* vs. *H* after cooling from 300 K in a 5 T field at different temperatures. For clarity, data for (b-d) at 25 K, 100 K, and 180 K are in Appendix **C**.

From **Eq. 2.7**, we obtain that $KV = k_B T_B \ln(\omega_0 / \omega)$, where T_B is the blocking temperature, ω is the measurement frequency, and we set $\omega_0 = 10^9$ Hz [32]. In this study, we measured the blocking temperature of the Co moments and did not directly measure moments of CoO grains because they are antiferromagnetic, and their crystal axes are randomly oriented.

The out-of-phase susceptibility (χ''), which corresponds to dissipative processes in the sample, is plotted along with χ' for the native sample in **Fig 3.8**. As expected, T_B increases with increasing frequency. The magnitude of χ'' at all temperatures increases with frequency, which is expected because the dissipation should be greater at higher frequencies. (Data for χ'' at 1kHz are omitted because they were excessively noisy and are not needed for the analysis.) From χ' at 1 kHz, we measured T_B = 195 K and calculated the product $KV = 3.7 \times 10^{-20}$ J.

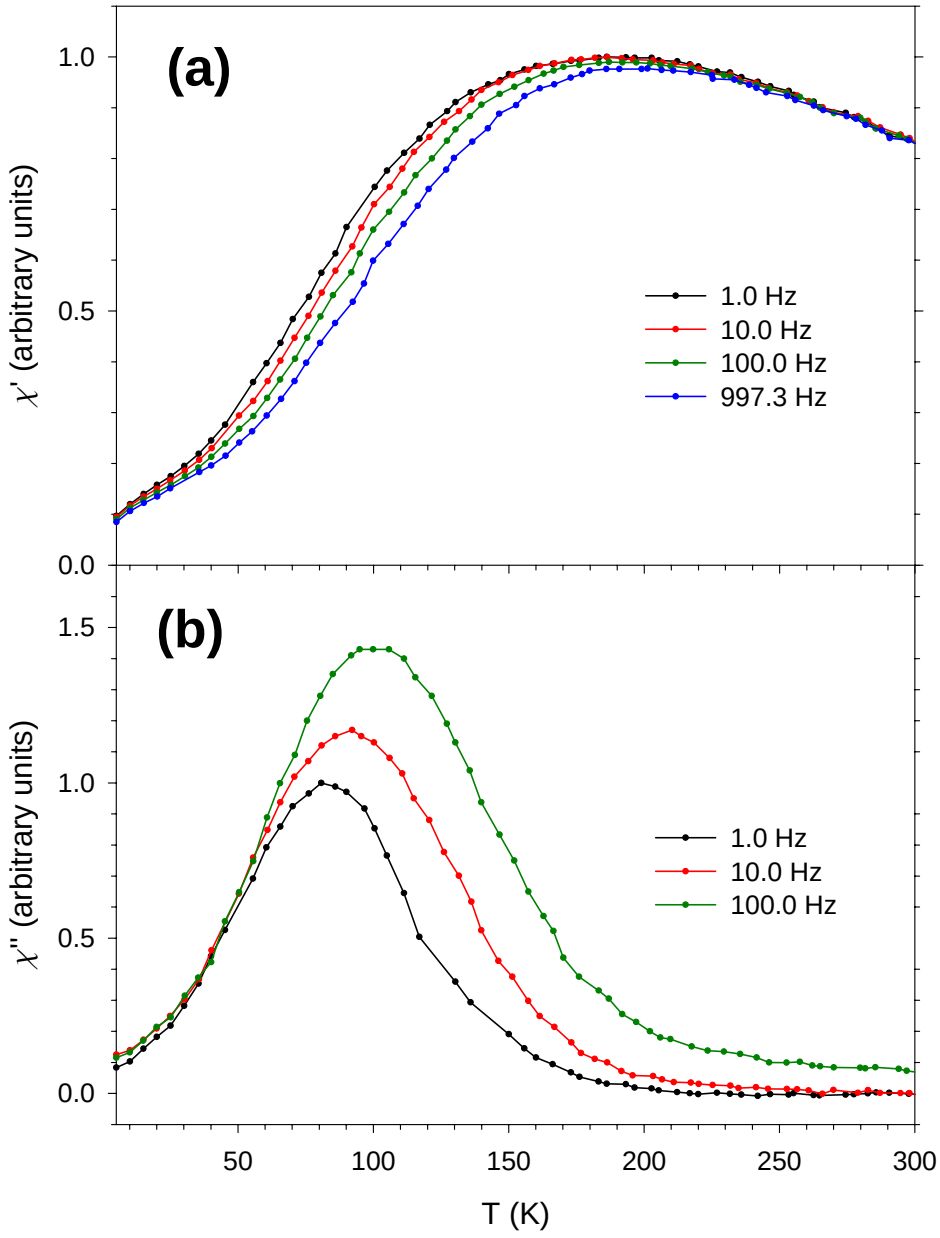

Figure 3.8: AC susceptibility for Co NPs with native oxidation: **(a)** χ'vs. *H* and **(b)** χ''vs. *H* at a variety of frequencies.

In DC measurements of the native sample (**Fig. 3.9a**), we found that T_B of the Co is 120 K. Since T_B is linearly proportional to V, we can propagate the standard deviation of the diameter distribution as measured by TEM into a standard deviation of 43 K in T_B. The effect of the size distribution is to make the peak in **Fig. 3.9a** broader than it would be if the particles were perfectly monodisperse. After oxidizing the sample to form partially oxidized NPs (**Fig. 3.9b**), T_B of the Co core increases to 170 K. This peak has vanished in the fully oxidized sample (**Fig. 3.9c**), which indicates that it has no ferromagnetic component and that oxidation was complete. The moments of the Co cores before and after partial oxidation were measured using the Curie-Weiss law by fitting a line to the ZFC *1/M* vs. *T* curve for $T > T_B$ in **Figs. 3.9a-b**, which is a standard analysis procedure that is described in Appendix **D**. The value of the slope extracted from *1/M* vs. *T* was multiplied by a factor of 0.56 in order to account for the oxide shell on the native sample and to normalize the units of *M* to be emu per unoxidized Co atom. In order to relate the volume of the ferromagnetic core of the particles to its volume, we used the bulk M_S (162 emu/g).

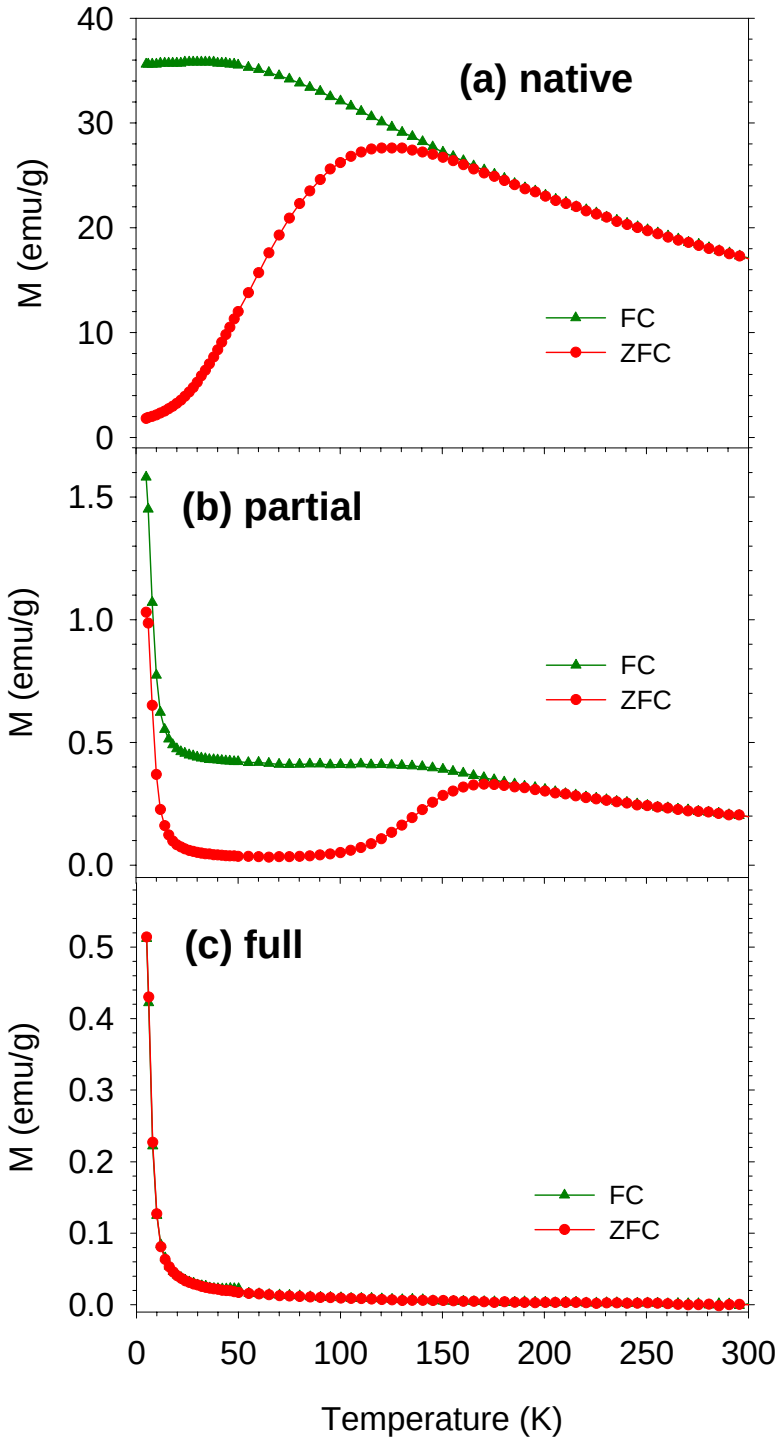

Figure 3.9: Co NPs with **(a)** native, **(b)** partial and **(c)** full oxidation: *M* vs. *T*: ZFC and field cooled (FC), measured in 0.01 T field.

The average moment per native NP (m_{native}) was 30,700 μ_B, which corresponds to a Co core diameter of 7.2 nm. We can now estimate an upper limit of the CoO thickness. After correcting for density differences in the Co core and CoO shell, we find that if 56% of the Co atoms are in the core, then the oxide thickness is ~1.0 nm, which gives a total native NP diameter of ~ 9.2 nm. Using this diameter, we find $K = 9.1 \times 10^4$ J/m^3 from the product KV, which is consistent with values from other measurements of polycrystalline FCC Co NPs[33]. We note that the total diameter measured from these SQUID measurements is slightly larger than that measured from TEM. TEM measurements may tend to slightly underestimate NP sizes, since it can be difficult to observe surface layers in TEM. Since the particles were briefly heated in air when preparing polymer sticks, it is also possible that the particles that were measured in SQUID had slightly more oxide and a larger diameter than those from the same sample that were measured in TEM.

For the partially oxidized NPs, the moment of the core determined from Curie-Weiss analysis ($m_{partial}$) was 2,900 μ_B. If we assume, as expected, that the moment scales linearly with the volume of the Co domain, then the Co core diameter in the partially oxidized NPs is 3.3 nm, and the oxide thickness is 3.2 nm. Even though the size of the Co core has decreased in the partially oxidized NPs, T_B has increased due to EB on each NP, which increases the effective anisotropy. Since T_B scales linearly with volume, if K is assumed to be independent of size, then T_B of the Co core of the partially oxidized NPs without any oxide would be 11 K, which strongly underscores the enhanced thermal stability provided by the CoO shell. A similar increase in T_B due to EB has been observed previously for sputtered Co NPs in a bulk CoO matrix[9].

Because EB occurs only for $T < T_N$, the upper limit of the temperature at which EB may be observed is T_N. However, for finite-thickness antiferromagnets, the anisotropy enhancement of EB can vanish at temperatures significantly below T_N[34, 35]. In order for EB to occur, the AFM must be able to pin the FM as it is reversed. A couple mechanisms by which small AFM grains may fail to pin an adjacent FM as the temperature increases are (1) if the AFM becomes superparamagnetic above a blocking temperature $T_{B,CoO} < T_N$, or (2) if the magnetocrystalline anisotropy of CoO decreases so that moments throughout the AFM would all rotate as the FM moment rotates[13]. Although our experiments do not elucidate the mechanism, the oxide layer on the native NPs is too thin for the sample to exhibit EB at any temperature, which others have also reported[9]. For partially oxidized NPs, however, EB causes T_B of the Co core to increase to 170 K. $T_{B,CoO}$ provides an upper bound of the temperature to which EB can be used to stabilize the orientation of the magnetic moment of Co NPs. If the CoO grain size is increased, EB should stabilize the moments to a higher temperature, since both $T_{B,CoO}$[36] and the magnetocrystalline anisotropy energy increase as the grain size increases.

We sought a value of $T_{B,CoO}$ for 3.2 nm CoO grains for comparison, but such a value is not consistently found in the thin film literature. The values reported for thin films of CoO with 3.0 nm thicknesses range from 170 K[37] to 250 K[36] and ~275 K[34, 38]. These differences can most likely be attributed to differences among the microstructures of the films and different materials on which the CoO films are deposited. In particular, if the film is deposited on a ferromagnet or on a ferrimagnet, the exchange coupling at the interface may also change have an effect in determining $T_{B,CoO}$. From our experiments, we know that $T_{B,CoO} \geq 170$ K for our 3.2 nm grains, since EB is observed up to this

temperature. Reported values of the magnetocrystalline anisotropy constant of CoO also vary widely with reports including K_{CoO} = 5 x 10^5 J/m^3 [39] and K_{CoO} = 1.1 x 10^7 J/m^3 [34]. These inconsistencies may also be due to microstructural differences and different measurement temperatures. If we assume that the grains are spheres of diameter 3.2 nm, we calculate $K_{CoO} \geq$ 3 x 10^6 J/m^3 from the expression, $K_{CoO} = k_B T_{B,CoO} \ln(\omega_0 / \omega)/V$, where we have used ω = 0.01 Hz, which is a value typically used for the time scale of DC SQUID measurements.

3.4.2: Defects in the CoO shell

We now turn to our observation of a low temperature paramagnetic response in the partially and fully oxidized samples which we attribute to defects in the CoO shell. Both samples exhibit a rise in the ZFC *M* vs. *T* curve as *T* approaches zero (**Figs. 3.9b-c**). This rise has previously been attributed to moments at defect sites in the CoO[10], such as crystal defects at NP surfaces, grain boundaries and variations in the Co to O stoichiometry. These moments associated with these crystal defects appear as paramagnetic impurities because they are prevented from strongly coupling into the AFM lattice. In order to measure the moments associated with these defects, Curie-Weiss law analysis was performed by fitting a line to the ZFC *1/M* vs. *T* data for *T* < 50 K in **Figs. 3.9b-c**, which is the same procedure that we performed earlier for the Co cores. The moment per NP of the paramagnetic impurities in the CoO shell is 420 μ_B in the partially oxidized sample and 330 μ_B in the fully oxidized sample. If each defect were a Co^{2+} ion, which has a moment of 3.8 μ_B[40], then these measured moments would correspond to about 95 Co^{2+} ions in the CoO shell that are not exchange coupled to the CoO lattice.

The assignment of these paramagnetic impurities as defects in the CoO shell is confirmed since these impurities are not observed in pure Co and the moments were about the same in the partially and fully oxidized samples. Such impurities have also been observed in CoO thin films[10]. These defects may also have a significant effect on EB[41]. These quantitative measurements may also be useful for comparison with theoretical simulations of the properties of antiferromagnetic NPs[42].

3.4.3: Phenomenological model: physical picture and temperature-dependence of exchange shift and coercivity

The *M* vs. *H* curves for partially oxidized NPs (**Figs. 3.7c-d**) are rich with many phenomena, because this sample has a FM core and AFM shell and exhibits EB. Before considering the asymmetries in the *M* vs. *H* measurements for partially oxidized NPs at low temperature, we first consider *M* vs. *H* measurements for fully oxidized NPs (**Fig. 3.7b**), so that the component of the magnetization due to the CoO shell can be removed from the magnetization of the partially oxidized sample, which simplifies the analysis. Saturation is not achieved in either the partially or fully oxidized sample. CoO has a large magnetocrystalline anisotropy, and the magnetization is due to canting the spins away from the easy axis of the AFM lattice. If all the Co^{2+} moments could be aligned ferromagnetically, the resulting saturation magnetization for pure CoO would be 238 emu/g[37]. Even in a 5 T field, the magnetization does not approach saturation. The magnetic susceptibility of fully oxidized NPs decreases with increasing *T*, as the grains become superparamagnetic and then paramagnetic for $T > T_N$. There have been a few studies of the magnetic properties of CoO NPs[43-45], but the magnetic measurements were

performed only at room temperature, and the smallest particles studied had d = 15 nm, for which $T_{B,CoO}$ is not significantly reduced from the bulk value[36].

An M vs. H curve for the partially oxidized NPs from which the susceptibility contribution from CoO has been removed is shown in **Fig. 3.10a**. (Data at 25 K, 100 K, and 180 K are included in Appendix **C**.) In order to remove the susceptibility contribution of the CoO shell and consider only the core magnetization, EB and other interface effects in the partially oxidized sample, we have subtracted M_{full} (**Fig. 3.7b**) multiplied by 0.947 from the curve for $M_{partial}$ (**Fig. 3.7c**). This factor of 0.947 is derived as $1-\left(\left(m_{partial}/m_{native}\right)\frac{91\,\text{emu/g}}{162\,\text{emu/g}}\right)$, since the partially oxidized NPs are not completely oxidized. The low temperature behavior of the partially oxidized NPs exhibits many unusual properties:

(1) M_S of the Co core increases significantly as the temperature is lowered (**Fig. 3.9a**). This is contrary to the expectation that M_S should be independent of temperature in this range.

(2) H_{EB} and H_C appear to be suppressed.

(3) The M vs. H curve splits into two highly asymmetric lobes.

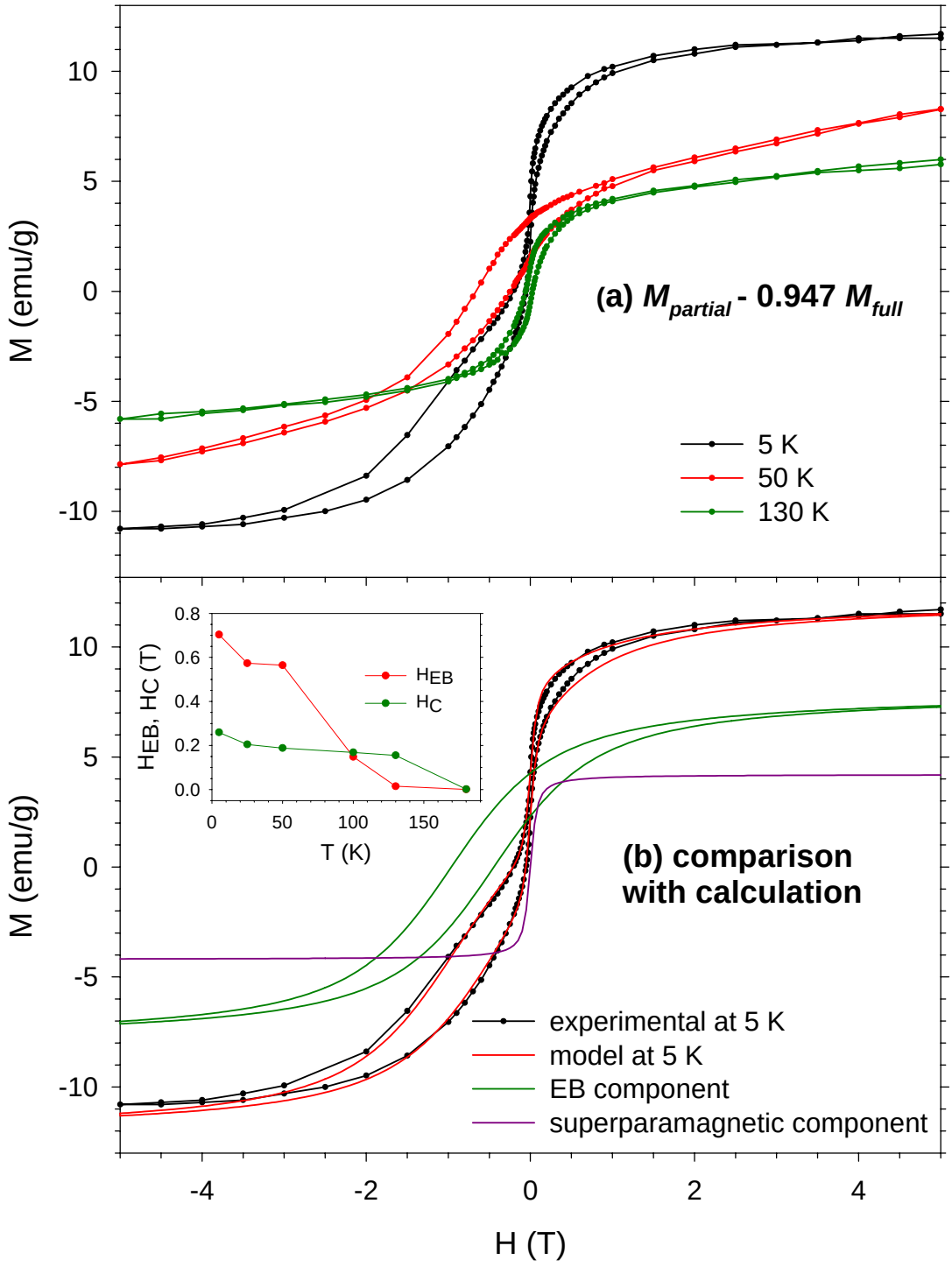

Figure 3.10: *M* vs. *H* for the partial sample after subtracting 0.947 times M_{full}: **(a)** from experimental data and **(b)** compared with modeled curves at 5 K; inset: H_{EB} and H_C vs. *T*. Additional data at 25 K, 100 K, and 180 K are in Appendix **C.**

Each of these observations is explained using a simple model. The curve in **Fig. 3.10a** at 5 K is modeled as the sum of two curves (**Fig. 3.10b**). The first curve simulates an exchange biased Co core that has nonzero H_{EB} and H_C and is generated by shifting two Langevin functions along the H axis. The second curve is a Langevin function centered at the origin, which corresponds to a superparamagnet. The parameters for these curves were determined by doing a fit to the experimental data. This simple model fits the data quite well.

The model reproduces property (1) well at a fixed temperature. As the temperature is increased to 300 K, we expect H_{EB} and H_C in the curve corresponding to the Co core to become smaller but for M_S to remain constant. In order for the superparamagnetic curve to fit the data, M_S decreases quickly with increasing temperature. Therefore, at a given temperature, this model works quite well, but the temperature dependent M_S of the superparamagnetic curve decreases much more quickly than the flattening that occurs in a Langevin function as T increases.

Properties (2) and (3) are also reproduced well. The superparamagnetic curve that is only significant at low T splits the curve at 5 K into two lobes. EB is not suppressed, but the measured H_{EB} is reduced because the large lobe does not significantly intersect the field axis. If the fitting procedure is used to remove the superparamagnetic component, then H_{EB} as measured from the curve for the simulated exchange biased core is 0.70 T at 5 K. We have repeated this fitting procedure at different temperatures, and have plotted H_{EB} and H_C from the curve for the simulated exchange biased core (**Fig. 3.10b, inset**). We find that H_{EB} and H_C decrease with increasing T and vanish when $T > T_{B,Co}$, as is expected.

We propose that there are clusters of a few unoxidized Co atoms in a Co-rich, O-deficient diffusion zone between the core and shell in the partially oxidized sample that are superparamagnetic at 5 K. Measurements of paramagnetic defect moments in the CoO shell have already been discussed, and this is a separate effect. For these clusters, M_S may decrease with increasing temperature because they are very small, and their surfaces are exchange coupled to the surrounding CoO spins, which could cause them to violate the Langevin temperature dependence, thus explaining property (1). As evidence for such Co clusters, we note that the height of the low temperature rise in the ZFC magnetization of partially oxidized sample (**Fig. 3.9b**) is 1.0 emu/g, but it is only 0.5 emu/g for the fully oxidized sample (**Fig. 3.9c**). This difference suggests that there are additional superparamagnetic spins at low temperature in the partially oxidized sample. A similar physical model of small ferromagnetic clusters at a metal/oxide interface was also recently proposed for the surfaces of FePt NPs[46]. Our model may also be applicable to work on α-Fe(core)/γ-Fe_2O_3(shell) NPs, in which an M vs. H curve with a similar asymmetry to ours was observed at low temperature[47].

Most other physical explanations for the superparamagnetic curve that we considered are inconsistent with the model. The superparamagnetic curve cannot be due to Co cores that are not significantly oxidized because M_S quickly decays with increasing temperature, which is inconsistent with the Langevin behavior that unoxidized cores would exhibit. One might attribute the superparamagnetic curve to an interaction between the Co core and CoO shell, such as canting of the CoO spins in the field of the core, or of defect moments orienting in the field generated by the core. Such an explanation is not plausible because the superparamagnetic curve is symmetric about zero

field and does not follow the exchange biased curve, as one would expect for an interaction with the cores. The superparamagnetic curve must be caused by an interaction with the applied field. Moreover, the magnetization of the CoO shell has already been removed in **Fig. 3.10a**, so the superparamagnetic curve cannot be attributed to an interaction between the applied field and the defects that are present in the CoO shell for both the partially and fully oxidized samples.

3.5: Proposal

It has previously been suggested that the enhancement in the thermal stability of magnetic NPs caused by EB could be useful for developing high-density magnetic recording media[9]. A challenge in developing high-density magnetic recording media is that as the ferromagnetic NP size decreases, T_B also decreases, but useful media must be operable at room temperature. In order to increase the thermal stability of magnetic NPs, their magnetic anisotropy must be increased. Colloidally prepared FePt NPs are actively being pursued as a potential material for high density magnetic recording due to their high magnetocrystalline anisotropy[4]. However, the desirable high-anisotropy, high-coercivity phase of FePt is achieved only after annealing, which leads to sintering and agglomeration[46, 48, 49], thereby causing a polydisperse size distribution and inhomogeneous magnetic properties.

In order to use EB rather than intrinsically high magneocrystalline anisotropy, a pair of FM/AFM materials could be chosen that exhibit EB, and for which the AFM has T_N and $T_{B,AFM}$ sufficiently greater than room temperature. Colloidal NPs of the FM could be patterned on a substrate. These NPs would be superparamagnetic when not coupled to

the AFM. After removing the ligands, a thin film of the AFM could then be deposited, which is depicted in **Fig. 3.11**. By cooling the substrate below T_N in a field, the unidirectional anisotropy directions of all of the NPs would be oriented in the same direction. This approach would circumvent the challenges associated with preparing the high-coercivity phase of FePt NPs and would also solve the problem of aligning the anisotropy axes of each NP into the same direction.

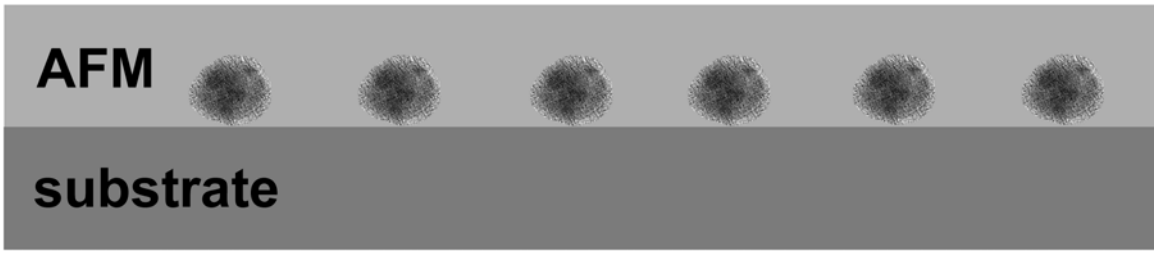

Figure 3.11: Proposed substrate for using exchange biased NPs for magnetic recording.

3.6: Conclusions

In this chapter, we have comprehensively investigated the magnetic properties of colloidal Co NPs with native, partial, and full oxidation. Beyond a minimum CoO shell thickness, EB greatly enhances the anisotropy of Co NPs and stabilizes their magnetic moments to higher temperatures. A phenomenological model was developed to describe the unusual *M* vs. *H* curves for partially oxidized NPs at low *T*. We attribute these unusual magnetic properties to clusters of Co atoms in a diffusion region at the interface in partially oxidized NPs. Paramagnetic spins at defect sites in CoO were also quantitatively measured.

3.7: References

[1] S. Sun and C. B. Murray, Journal of Applied Physics 85, 4325 (1999).

[2] D. P. Dinega and M. G. Bawendi, Angewandte Chemie, International Edition 38, 1788 (1999).

[3] V. F. Puntes, K. M. Krishnan, and P. Alivisatos, Applied Physics Letters 78, 2187 (2001).

[4] S. Sun, C. B. Murray, D. Weller, L. Folks, and A. Moser, Science (Washington, D. C.) 287, 1989 (2000).

[5] S. H. Sun, S. Anders, T. Thomson, J. E. E. Baglin, M. F. Toney, H. F. Hamann, C. B. Murray, and B. D. Terris, Journal of Physical Chemistry B 107, 5419 (2003).

[6] Y. H. Huang, Y. Zhang, G. C. Hadjipanayis, and D. Weller, Journal of Applied Physics 93, 7172 (2003).

[7] M. Chen, J. P. Liu, and S. H. Sun, Journal of the American Chemical Society 126, 8394 (2004).

[8] D. P. Dinega and Massachusetts Institute of Technology. Dept. of Chemistry., 2001).

[9] V. Skumryev, S. Stoyanov, Y. Zhang, G. Hadjipanayis, D. Givord, and J. Nogués, Nature (London, United Kingdom) 423, 850 (2003).

[10] K. Takano, R. H. Kodama, A. E. Berkowitz, W. Cao, and G. Thomas, Physical Review Letters 79, 1130 (1997).

[11] F. Radu, M. Etzkorn, R. Siebrecht, T. Schmitte, K. Westerholt, and H. Zabel, Physical Review B: Condensed Matter and Materials Physics 67, 134409/1 (2003).

[12] D. L. Peng, K. Sumiyama, T. Hihara, S. Yamamuro, and T. J. Konno, Physical Review B: Condensed Matter and Materials Physics 61, 3103 (2000).

[13] S. Gangopadhyay, G. C. Hadjipanayis, C. M. Sorensen, and K. J. Klabunde, Journal of Applied Physics 73, 6964 (1993).

[14] R. Morel, A. Brenac, and C. Portemont, Journal of Applied Physics 95, 3757 (2004).

[15] M. Verelst, T. O. Ely, C. Amiens, E. Snoeck, P. Lecante, A. Mosset, M. Respaud, J. M. Broto, and B. Chaudret, Chemistry of Materials 11, 2702 (1999).

[16] M. Spasova, U. Wiedwald, M. Farle, T. Radetic, U. Dahmen, M. Hilgendorff, and M. Giersig, Journal of Magnetism and Magnetic Materials 272-276, 1508 (2004).

[17] J.-K. Lee and S. M. Choi, Bulletin of the Korean Chemical Society 24, 32 (2003).

[18] J. Osuna, D. deCaro, C. Amiens, B. Chaudret, E. Snoeck, M. Respaud, J. M. Broto, and A. Fert, Journal of Physical Chemistry 100, 14571 (1996).

[19] J. P. Chen, C. M. Sorensen, K. J. Klabunde, and G. C. Hadjipanayis, Journal of Applied Physics 76, 6316 (1994).

[20] C. Petit and M. P. Pileni, Journal of Magnetism and Magnetic Materials 166, 82 (1997).

[21] C. M. Niemeyer, Angewandte Chemie, International Edition 40, 4128 (2001).

[22] Y. Lalatonne, J. Richardi, and M. P. Pileni, Nature Materials 3, 121 (2004).

[23] J. Lee, V. C. Sundar, J. R. Heine, M. G. Bawendi, and K. F. Jensen, Advanced Materials (Weinheim, Germany) 12, 1102 (2000).

[24] M. Spasova, T. Radetic, N. S. Sobal, M. Hilgendorff, U. Wiedwald, M. Farle, M. Giersig, and U. Dahmen, Materials Research Society Symposium Proceedings 721, 195 (2002).
[25] Y. Yin, R. M. Rioux, C. K. Erdonmez, S. Hughes, G. A. Somorjai, and A. P. Alivisatos, Science (Washington, DC, United States) 304, 711 (2004).
[26] N. N. Greenwood and A. Earnshaw, in *Chemistry of the Elements* (Butterworth-Heinemann, Boston, 1997).
[27] R. C. O'Handley, *Modern Magnetic Materials: Principles and Applications* (John Wiley & Sons, New York, 2000).
[28] N. Wu, L. Fu, M. Su, M. Aslam, K. C. Wong, and V. P. Dravid, Nano Letters 4, 383 (2004).
[29] Pick and H. Dreyssé, Physical Review B 59, 4195 (1999).
[30] A. E. Berkowitz, J. A. Lahut, I. S. Jacobs, L. M. Levinson, and D. W. Forester, Physical Review Letters 34, 594 (1975).
[31] C. M. Sorensen, in *Nanoscale Materials in Chemistry*, edited by K. J. Klabunde (Wiley-Interscience, New York, 2001), p. 169.
[32] S. Blundell, *Magnetism in Condensed Matter* (Oxford University Press, New York, 2001).
[33] G. A. Held, G. Grinstein, H. Doyle, S. Sun, and C. B. Murray, Physical Review B: Condensed Matter and Materials Physics 64, 012408/1 (2001).
[34] P. J. van der Zaag, Y. Ijiri, J. A. Borchers, L. F. Feiner, R. M. Wolf, J. M. Gaines, R. W. Erwin, and M. A. Verheijen, Physical Review Letters 84, 6102 (2000).
[35] U. Nowak, K. D. Usadel, J. Keller, P. Miltényi, B. Beschoten, and G. Güntherodt, Physical Review B: Condensed Matter and Materials Physics 66, 014430/1 (2002).
[36] Y. J. Tang, D. J. Smith, B. L. Zink, F. Hellman, and A. E. Berkowitz, Physical Review B: Condensed Matter and Materials Physics 67, 054408/1 (2003).
[37] T. Ambrose and C. L. Chien, Physical Review Letters 76, 1743 (1996).
[38] E. N. Abarra, K. Takano, F. Hellman, and A. E. Berkowitz, Physical Review Letters 77, 3451 (1996).
[39] W. H. Meiklejohn and C. P. Bean, Physical Review 105, 904 (1957).
[40] W. L. Roth, Physical Review 110, 1333 (1958).
[41] J. Keller, P. Miltényi, B. Beschoten, G. Güntherodt, U. Nowak, and K. D. Usadel, Physical Review B: Condensed Matter and Materials Physics 66, 014431/1 (2002).
[42] R. H. Kodama and A. E. Berkowitz, Physical Review B 59, 6321 (1999).
[43] L. Zhang, D. Xue, and C. Gao, Journal of Magnetism and Magnetic Materials 267, 111 (2003).
[44] L. Zhang and D. Xue, Journal of Materials Science Letters 21, 1931 (2002).
[45] C. F. J. Flipse, C. B. Rouwelaar, and F. M. F. De Groot, European Physical Journal D: Atomic, Molecular and Optical Physics 9, 479 (1999).
[46] T. Thomson, M. F. Toney, S. Raoux, S. L. Lee, S. Sun, C. B. Murray, and B. D. Terris, Journal of Applied Physics 96, 1197 (2004).
[47] R. K. Zheng, G. H. Wen, K. K. Fung, and X. X. Zhang, Journal of Applied Physics 95, 5244 (2004).

[48] T. J. Klemmer, C. Liu, N. Shukla, X. W. Wu, D. Weller, M. Tanase, D. E. Laughlin, and W. A. Soffa, Journal of Magnetism and Magnetic Materials 266, 79 (2003).
[49] H. Zeng, S. H. Sun, T. S. Vedantam, J. P. Liu, Z. R. Dai, and Z. L. Wang, Applied Physics Letters 80, 2583 (2002).

Appendix A for Chapter 3

Method for preparing small (d = 2-3 nm) cobalt nanoparticles

The method for preparing small (d = 2-3 nm) Co NPs is identical to the method described for preparing larger Co NPs in section **3.2.1** with the following exceptions: The amount of trioctylphosphine was increased to 1.0 mL. The heating procedure was also prolonged: After heating at 180 ˚C for 10 minutes, the mixture was heated to 190 ˚C for 10 minutes, to 200 ˚C for 10 minutes, to 210 ˚C for 10 minutes, and then to 215 ˚C for 15 minutes.

After adding the stearic acid and cooling, a modified procedure was used to process the NPs because of their size-dependent solubility. The contents of the reaction flask were split into four parts, and 20 mL of methanol and 10 mL of ethanol were added to each part. After centrifuging, most of the NPs had precipitated, and the supernatant (which still had a brown color) was discarded. The precipitate was redispersed into 10 mL of hexanes and was centrifuged, after which the supernatant was retained, and 10 mL of ethanol and 20 mL of ethanol were added to it to precipitate the NPs. After centrifuging, the precipitated NPs could be redispersed into hexanes or THF. Fig. **A.1** shows a TEM image of Co NPs prepared in this manner. A small portion of larger NPs are also present.

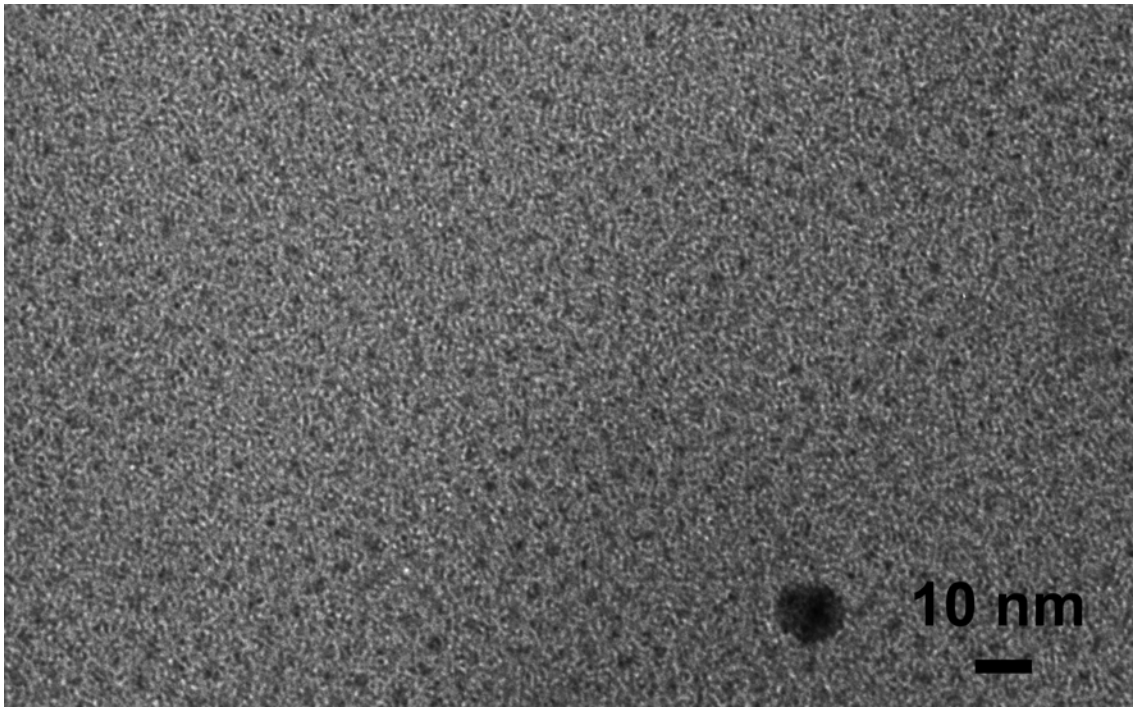

Figure A.1: TEM of small Co NPs

Appendix B for Chapter 3

Justification that cobalt NPs are non-interacting in the polymer matrix

The magnetic field generated outside of a single-domain ferromagnetic sphere that is magnetized along the x-axis sphere of radius r_0 is given as[1]:

$$H_x = \mu_0 M_0 \frac{1}{3}\left(\frac{r_0}{r}\right)^3 \left(2\,\mathrm{Cos}^2\,\theta - \mathrm{Sin}^2\,\theta\right) \qquad \textbf{(Eq. B.1)}$$

$$H_y = H_z = \mu_0 M_0 \left(\frac{r_0}{r}\right)^3 \mathrm{Cos}(\theta)\mathrm{Sin}(\theta)\,, \qquad \textbf{(Eq. B.2)}$$

where θ is the angle between the magnetization vector and the x-axis. The maximum field is generated along the x-axis, and is of magnitude 1.2 T at the surface of the sphere, but this field decays quickly with increasing distance.

Since the maximum field is generated along the x-axis, H_x is an upper bound of the field generated by a NP in any direction. In order to obtain the maximum field that another NP may experience due to this field, we calculate the minimum separation distance between the core of one NP and the interface between the core and shell of a neighboring NP. That distance is the radius of one NP plus twice its oxide thickness plus the distance between particles due to their ligand shells, which we estimate to be 1.5 nm from TEM measurements. For the native sample, the core diameter is 7.2 nm. Therefore, the minimum core-to-interface separation is 7.1 nm, and the average core-to-core separation is 10.7 nm. The minimum core-to-interface separation in the partial sample is 9.6 nm, and the minimum core-to-core separation is 11.2 nm. The maximum field, H_{max},

experienced by a second particle in the vicinity of the first which generates the field is plotted as a function of distance in **Fig. B.1** (native sample) and **Fig. B.2** (partial sample). For the native sample, H_{max} at a distance of 7.1 nm is 0.16 T, and at 10.7 nm, it is 0.05 T. For the partial sample, H_{max} at a distance of 9.6 nm is 0.006 T, and at 11.2 nm, it is 0.004 T.

The maximum field of 0.16 T for the native sample is significant. However, that field quickly decays across the volume of the NP, and the effective field at the minimum separation is much lower. Almost all of the NPs, even in the aggregated areas of Fig. **3.2** have at least a small separation, which would reduce the maximum field to below 0.05 T. NPs in Fig. **3.2** which appear to overlap may an actually have some separation, since the microtome slice was 20-40 nm thick. Most of the NPs have a larger separation and thus have even weaker interactions, which should not significantly effect the magnetic measurements. The interactions at the same distances in the partial sample are much smaller than for the native sample, since the partial core is smaller, and the CoO is thicker. Therefore, interparticle interactions in both samples should not significantly affect the magnetic measurements. If the interparticle interactions were to have an effect, it would be greater for the native sample than for the partial sample.

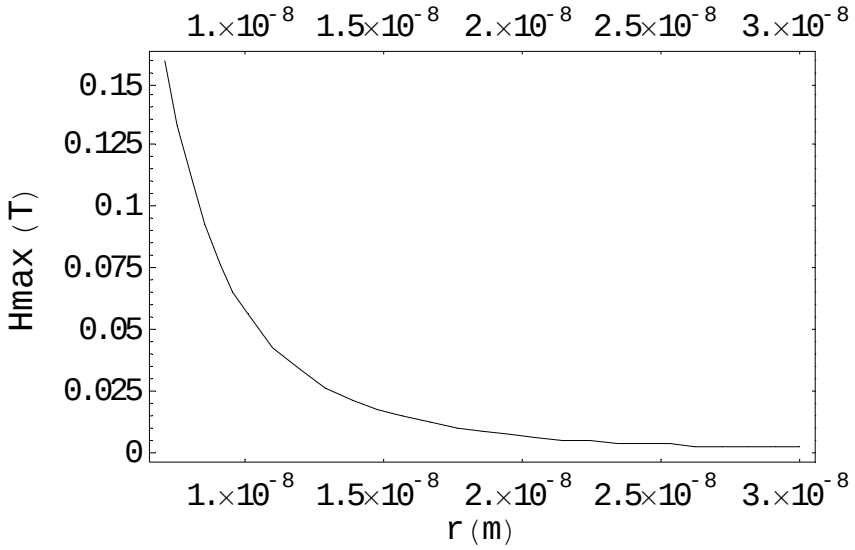

Figure B.1: Maximum field experienced by one native NP which is generated by another native NP, as a function of distance

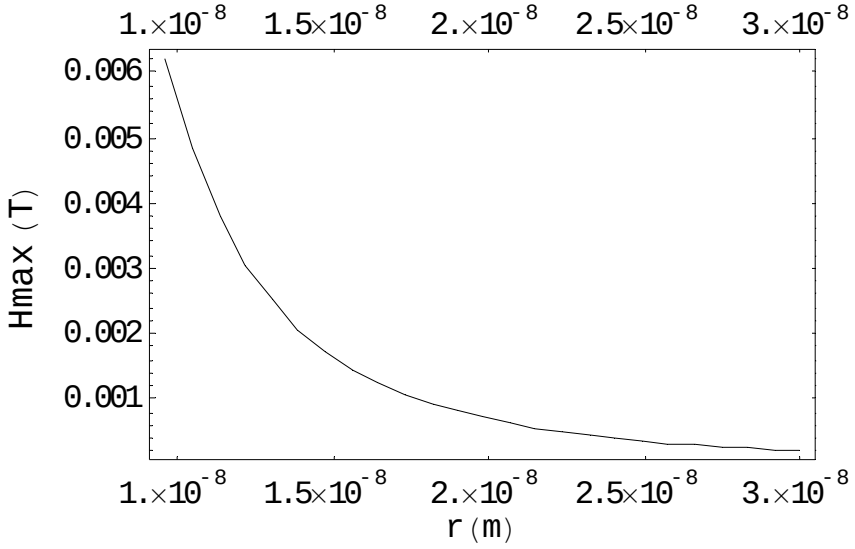

Figure B.2: Maximum field experienced by one partial NP which is generated by another partial NP, as a function of distance

References:

[1] R. C. O'Handley, *Modern Magnetic Materials: Principles and Applications* (John Wiley & Sons, New York, 2000).

Appendix C for Chapter 3

Supplementary data

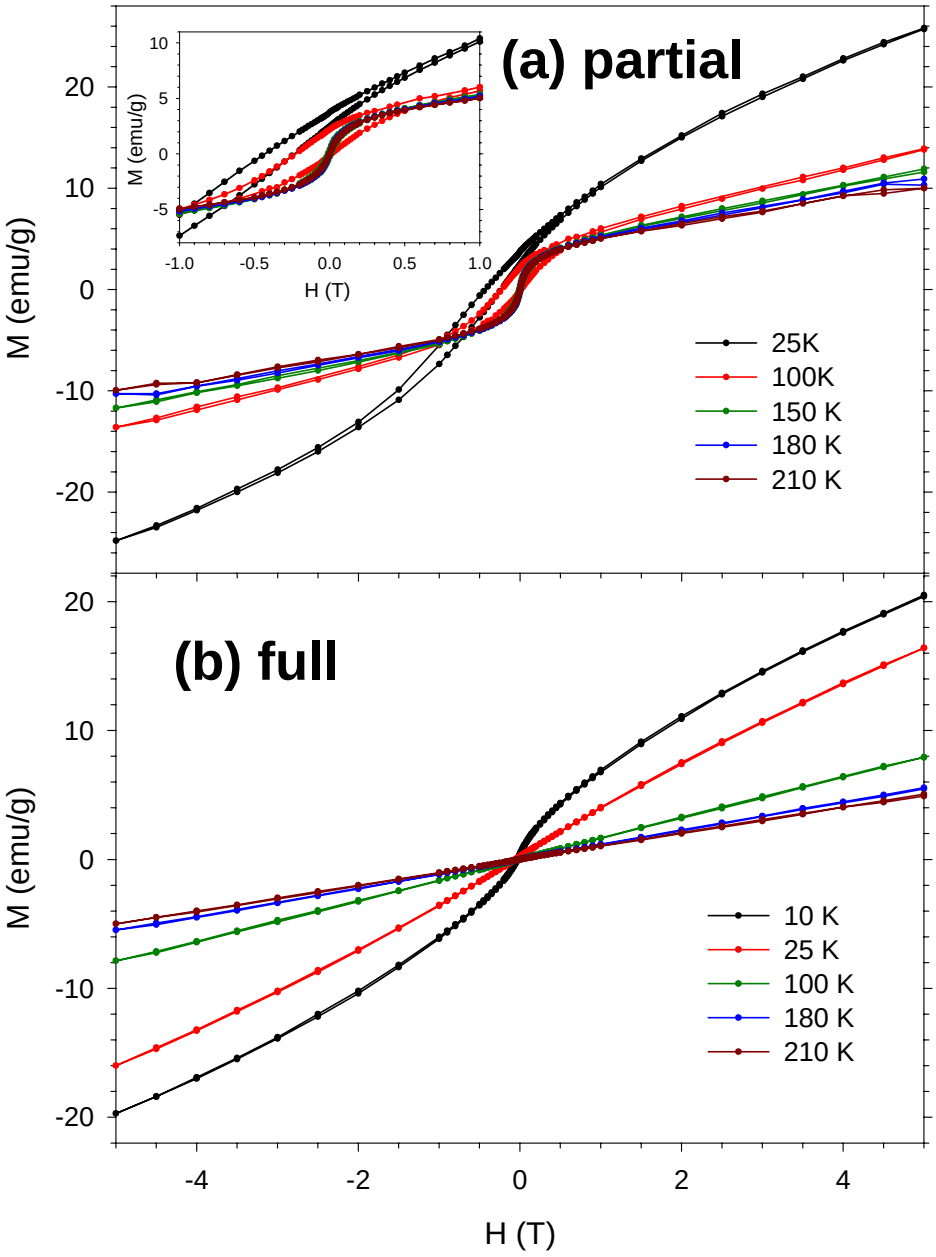

Figure C.1: (Additional data for **Fig. 3.7**) Co NPs with **(a)** partial and **(b)** full oxidation: *M* vs. *H* after cooling from 300 K in a 5 T field at different temperatures.

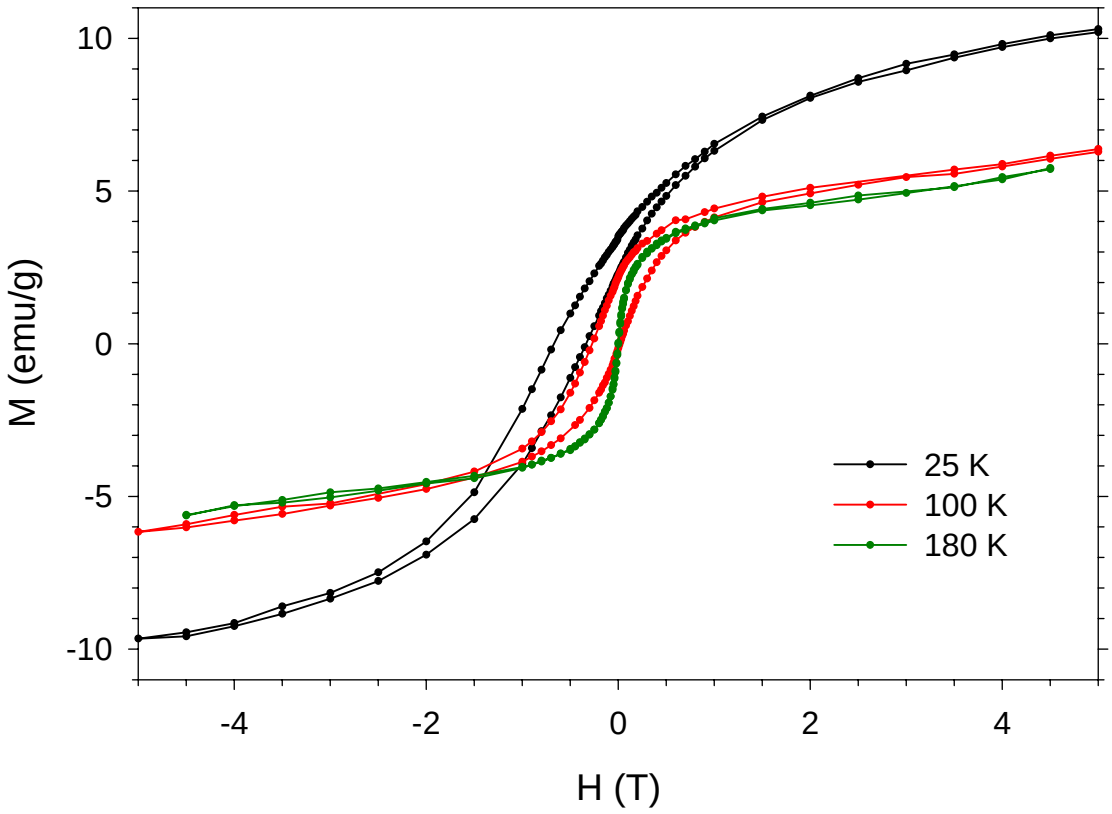

Figure C.2: (Additional data for **Fig. 3.10a**) *M* vs. *H* for the partial sample after subtracting 0.947 times M_{full} at different temperatures. (The field for the curve at 180 K was swept to ±5 T, but the data at ±5 are omitted because there was an instrumental error during those measurements.)

Appendix D for Chapter 3

Curie-Weiss law analysis

The field- and temperature-dependence of the magnetization of a paramagnet is described classically by a Langevin function. Molecular paramagnets with small J (total angular momentum quantum number) are better described by a Brillouin function, which takes into account the quantized nature of spin. However, all of the moments described in this thesis have large J, for which the Brillouin function reduces to a Langevin function in the classical limit:

$$\langle m \rangle = \mu L\left(\frac{\mu\mu_0 H}{k_B T}\right) = \mu \coth\left(\frac{\mu\mu_0 H}{k_B T} - \frac{k_B T}{\mu\mu_0 H}\right) \qquad \textbf{(Eq. D.1)}$$

In **Eq. D.1,** <*m*> is the average moment measured, μ is the saturation moment, *H* is the magnetic field, k_B is the Boltzmann constant, and *T* is the temperature. For small *B*, we take the Taylor expansion of <*m*> about *B* = 0 and retain the first term:

$$\langle m \rangle = \mu\left(\frac{\mu\mu_0 H}{3k_B T} - \frac{1}{45}\left(\frac{\mu\mu_0 H}{k_B T}\right)^3 + \ldots\right) \approx \frac{\mu^2 \mu_0 H}{3k_B T} \qquad \textbf{(Eq. D.2)}$$

The magnetization $M = N_V \langle m \rangle$, where $N_V = 1/V$ is the number of moments per unit volume, and *V* is the volume of one moment. Therefore,

$$\chi = \frac{M}{H} = \frac{N_V \langle m \rangle}{H} = \frac{\mu^2 N_V \mu_0}{3k_B T} = \frac{C}{T}, \qquad \textbf{(Eq. D.3)}$$

where χ is the magnetic susceptibility, and

$$C = \frac{\mu^2 N_V \mu_0}{3k_B} \qquad \textbf{(Eq. D.4)}$$

is the Curie constant. A slightly modified form of **Eq. D.3**, which incorporates an additional parameter, T_C, is known as the Curie-Weiss Law:

$$M = \frac{\mu^2 N_V \mu_0 H}{3k_B(T - T_C)} \qquad \textbf{(Eq. D.5)}$$

Eq. C.5 can be applied to calculate the magnitude of a (super)paramagnetic moment from the decay of its magnetization with increasing temperature. Using $N_V = 1/V$, we note that

$$\frac{1}{M} = \frac{3k_B V(T - T_C)}{\mu^2 \mu_0 H} \qquad \textbf{(Eq. D.6)}$$

has a linear dependence on T. However, $V = \mu / M_S$. Therefore, the slope of $1/M$ vs. T is

$$\frac{d(1/M)}{dT} = \frac{3k_B}{M_S \mu \mu_0 H} \quad . \qquad \textbf{(Eq. D.7)}$$

M_S can be measured, and from the slope, the moment, μ may be calculated.

In our analysis, N_V was calculated for the native sample using **Eq. D.7**. We then solved for $N_V = M_S/\mu$. If we assume that the number of Co atoms per NP did not change during oxidation, then N_V is the same for each sample because the magnetization was reported in units of moment per mass of unoxidized cobalt. For the analysis of the partial and full samples, we derived

$$\frac{d(1/M)}{dT} = \frac{3k_B}{N_V \mu^2 \mu_0 H} \qquad \textbf{(Eq. D.8)}$$

from **Eq. D.6** and solved it for μ.

Chapter 4

Defects in CoO dominate exchange biasing in partially oxidized cobalt nanoparticles

4.1: Defects and the domain state model of exchange biasing

In the previous chapter, we showed that the partially oxidized sample exhibits EB, which causes an increase in T_B of the core. We also observed paramagnetic impurities in the CoO shell, which we attributed to crystallographic defects at surfaces, grain boundaries, and variations in the Co to O stoichiometry, since oxidation to Co_3O_4 is also possible. We now consider the role that these defects play in determining the EB behavior.

Since the initial discovery of EB in oxidized Co NPs[1], many models have been proposed, but a comprehensive microscopic understanding is still lacking. It has been well-established that spins at the FM/AFM interfaces adopt an orthogonal arrangement which is called "spin-flop coupling,"[2] but this configuration does not give rise to EB[3]. Recently, the role of the crystallographic and magnetic domain structure of the AFM has been investigated[4-7]. FM/AFM layers can have uncompensated spins at the interface, which are tightly coupled to the AFM lattice but are not antiferromagnetically coupled with another spin in the interfacial plane. These uncompensated spins can give rise to EB but are not required, since fully compensated interfaces can also exhibit EB[8].

Thin film experiments have shown that about 1% of the CoO surface spins are uncompensated[9]. If we suppose that 1% of the Co/CoO interface in our partially oxidized

NPs has uncompensated CoO spins, a total of 5 uncompensated CoO spins would be found on the surface of the Co core. In Chapter **3**, we found that there is a moment equivalent to about 95 Co^{2+} moments per NP. It is quite plausible that the EB generated by these defect moments could overwhelm that of 5 uncompensated moments at low temperature.

A roughened FM/AFM interface can exhibit enhanced[10] or reduced EB[8] compared to a smooth one. Recent experiments[5] have shown that if defects are induced in the AFM but away from the interface with the FM, then the EB can also be enhanced. This result is explained by the domain state (DS) model of EB[4]. In the DS model, the domain structure throughout the AFM determines the spin arrangement and the exchange interaction at the interface[4]. The DS model has been experimentally verified in thin films by inducing chemical defects such as Mg^{2+} substitution or overoxidation in a CoO film coupled to Co, but defects were intentionally induced 3 nm away from the interface with Co. For small defect concentrations (such that the defects are a perturbation on the perfect lattice, rather than making it amorphous), H_{EB} increases with increasing defect concentration[5]. Nowak, et al[4] interpreted their data by attributing the enhanced EB to a change in the domain structure of the AFM. Domains in the AFM carry a small uncompensated moment at the FM/AFM interface. Defects induced anywhere in the AFM can aid in the formation of domain walls, thereby modifying the AFM domain structure and the uncompensated moment. Increased numbers of defects often lead to enhanced EB.

The DS model explains many phenomena in exchange biased systems and the difficulty in quantitatively reproducing others' measurements, because the DS of an AFM

is highly sensitive to the conditions under which the interface is prepared[4]. Unfortunately, the DS model is difficult to apply quantitatively in a predictive manner because it is difficult to experimentally characterize the DS of an AFM.

4.2: First switching experiment: field-dependent magnetization

4.2.1: Defects dominate exchange bias

EB may be observed in the partial sample below a maximum temperature at which the CoO shell fails to pin the core. We have attributed the low temperature rise in **Figs. 3.9b-c** to crystallographic and stoichiometric defects. Already at 50 K, this rise has significantly decayed. We attribute the peak at 170 K in **Fig 3.9b** to pinning that is caused by the CoO lattice. If the defect moments are not optimally exchange coupled into the antiferromagnetic lattice, we would expect each defect moment to have a lower "effective" T_N, at which the defect moment becomes paramagnetic. Our experiments show that this is the case, and we have studied the role of these defects in EB.

By cooling the sample in a biasing field from room temperature to below 170 K and then switching at an intermediate temperature before cooling to 5 K, we have frozen the CoO lattice to pin a particular orientation of the Co core. If the defect moments are still paramagnetic at the switching temperature, they could be reoriented to pin the opposite orientation of the core, which could cause a change in the EB.

The partial and full samples were cooled in a -5 T field from 300 K to a switching temperature of 25-100 K, at which the field was switched to at 5 T, and cooling was resumed to 5 K. This cooling procedure is depicted in **Fig. 4.1**. After cooling, *M* vs. *H* (**Fig. 4.2**) and remanent magnetization measurements (**Fig 4.9**) were performed. In order

to remove the component of the CoO susceptibility from the *M* vs. *H* curve and consider only the effects of the ferromagnetic core and EB, the same procedure as described in section **3.4.3** was used, in which we carried out identical measurements on the partial and full samples and then plotted (**Fig. 4.2**) the difference, $M_{partial} - 0.947M_{full}$. (The *M* vs. *H* curves for the partial and full samples are included in Appendix **E** (**Fig. E.1**).) Each *M* vs. *H* curve was fit in order to remove the superparamagnetic component, and the values for H_{EB} and H_C were taken from the fit using the procedure developed in section **3.4.3,** and are presented in the inset in **Fig 4.2**.

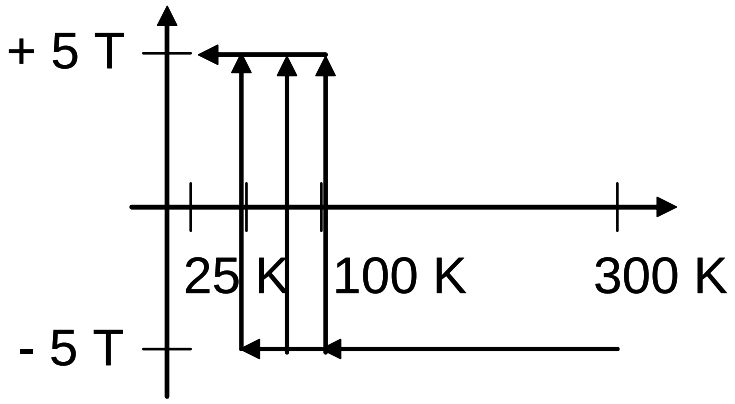

Figure 4.1: Switching procedure for **Fig. 4.2** and **Fig 4.9**

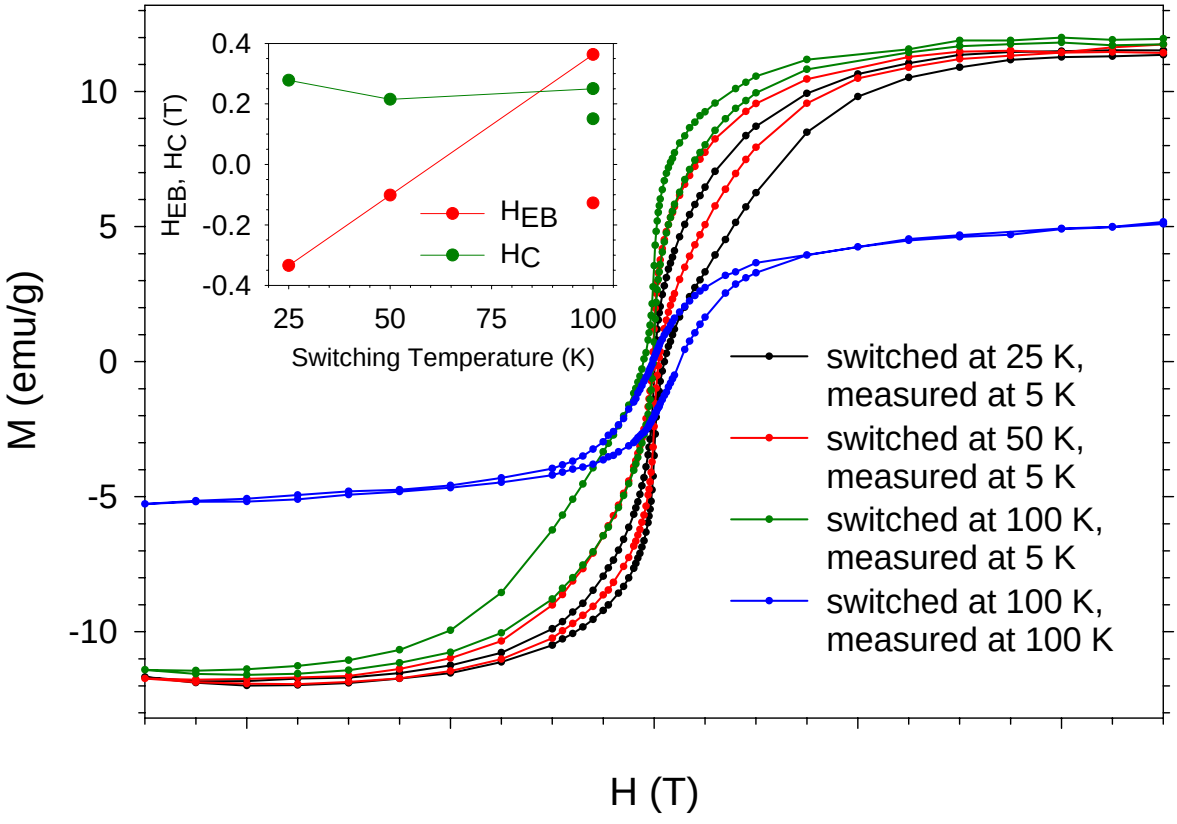

Figure 4.2: ($M_{partial}$ – 0.947 M_{full}) vs. H after cooling from 300 K in a -5 T field, followed by switching at 25 K, 50 K, or 100 K; inset: H_{EB} and H_C vs. T from the fit for each curve. Curves for $M_{partial}$ and M_{full} vs. H are in Appendix **E**, **Fig. E.1**.

If the sample were cooled from 300 K to 5 K in a -5 T field, we would expect $H_{EB,\ 5\ K}$ = -0.70 T < 0 (section **3.4.3**). We note that for a switching temperature (T_{switch}) of 25 K, H_{EB} = -0.34 T > -0.70 T. (Negative H_{EB} is consistent with having the larger lobe in the *M* vs. *H* curve along the positive field-axis.) Switching at 25 K reduces the magnitude of the EB compared to the field cooled case, but H_{EB} is still negative. As T_{switch} is increased to 50 K, $H_{EB,\ 5K}$ = -0.10 T, and for T_{switch} = 100 K, $H_{EB,\ 5K}$ = 0.36 T > 0.

These results are consistent with a physical model in which the defect moments would freeze at a distribution of temperatures below 170 K. For T_{switch} = 25 K, some of the defect moments have reoriented at 25 K to pin the core in the positive field direction, and after cooling to 5 K, they have frozen and continue pinning the core in the positive field direction. Their effect is to reduce the magnitude of H_{EB}, but not enough defect moments are reoriented to reverse the sign of H_{EB}. For T_{switch} = 50 K, the situation is the same, except more defect moments have reoriented to pin the core in the positive field direction, and the magnitude of H_{EB} is further reduced. For T_{switch} = 100 K, enough defect moments have reoriented to give rise to positive H_{EB}. Therefore, those defect moments that froze below 100 K dominate the EB generated in the opposing field direction by defect moments that froze above 100 K and the CoO lattice. Thus, we have shown that the defect moments dominate EB, and we have some evidence that they have a variety of freezing temperatures.

4.2.2: Exchange field changes sign during heating

After measuring at 5 K for T_{switch} = 100 K, the sample was heated to 100 K in a 5 T field and was measured again, which is also plotted in **Fig. 4.2**. We found that

$H_{EB,\ 100\ K}$ = -0.13 T. Although H_{EB} was positive at 5 K, at 100 K, it is negative. Therefore, H_{EB} has switched signs during the heating process. By heating the sample up to 100 K, the defect moments which were frozen below 100 K have "melted" (become paramagnetic), and they can no longer pin the core. This *M* vs. *H* loop is the same as the one which we would observe after cooling the sample from 300 K to 100 K in a -5 T field and then immediately measuring at 100 K.

4.3: Second switching experiment: causing the exchange field to change sign twice during heating

This unusual result led us to ask us whether we could cause H_{EB} to switch sign twice during heating, if we switched the biasing field twice during cooling. We used the cooling procedure shown in **Fig. 4.3**. Each sample was cooled from 300 K to 100 K in a 5 T field. At 100 K, the field was switched to -5 T, and cooling was resumed to 50 K, at which the field was switched to 5 T, and cooling was continued to 5 K.

As in section **4.2.1**, the partial and full samples were measured, and *M* vs. *H* curves were plotted using $M_{partial} - 0.947M_{full}$ (**Fig. 4.4**). Remanent magnetization measurements were also performed (**Fig. 4.13**) and are discussed in section **4.9**. The *M* vs. *H* curves for the partial and full samples are included in Appendix **E** (**Fig. E.2**). The values for H_{EB} and H_C were taken from the fit using the procedure developed in section **3.4.3,** and are presented in the inset in **Fig 4.4**.

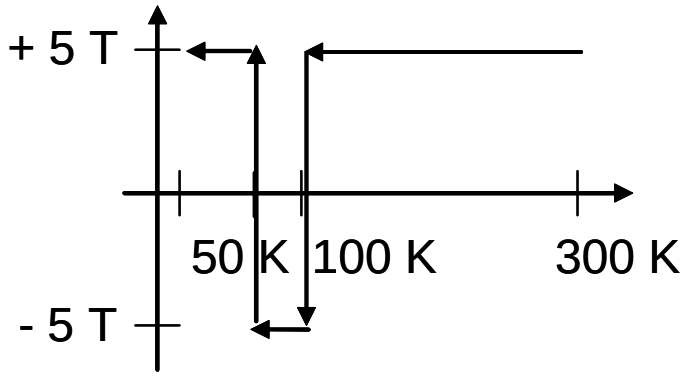

Figure 4.3: Switching procedure for **Fig. 4.4** and **Fig. 4.13**

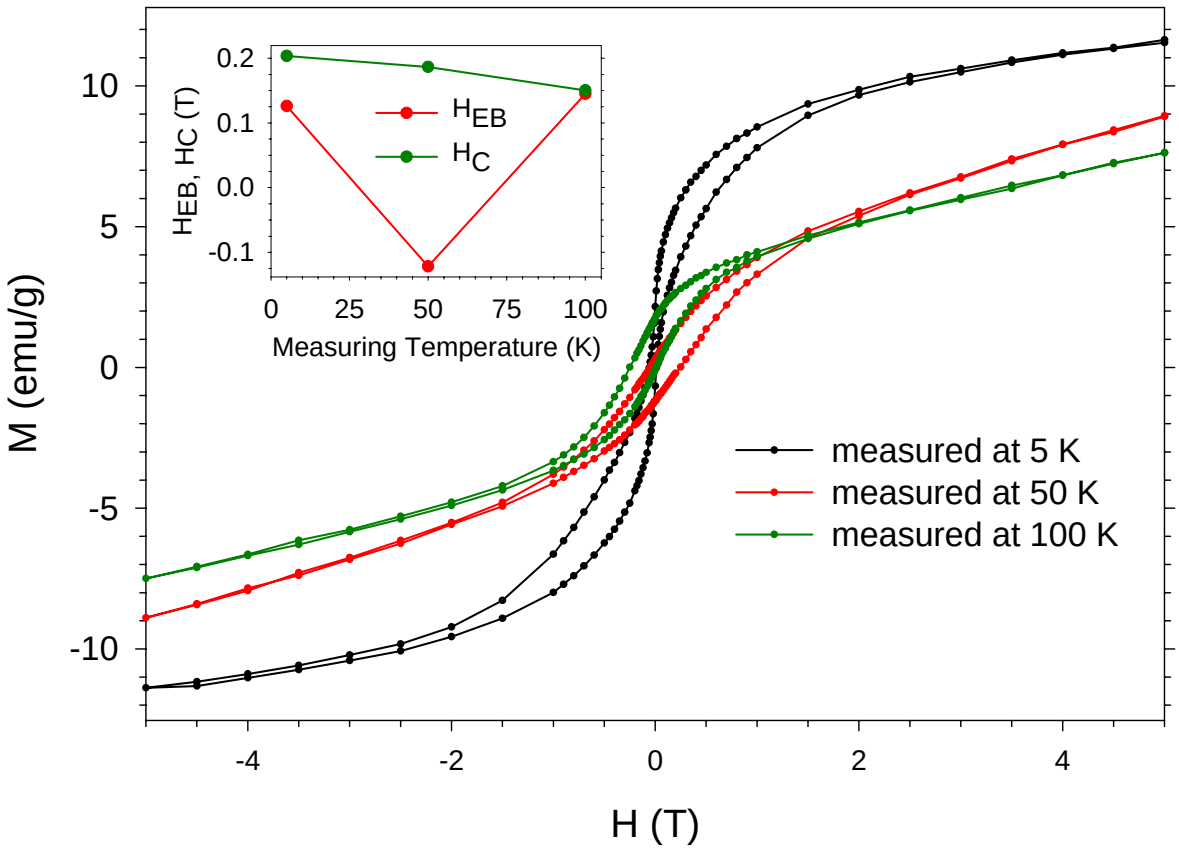

Figure 4.4: ($M_{partial}$ – 0.947 M_{full}) vs. H after cooling from 300 K to 100 K in a -5 T field, from 100 K to 50 K in a 5 T field, and from 50 K to 5 K in a -5 T field, followed by measurement at 5 K, 50 K, and 100 K; inset H_{EB} and H_C vs. T from the fit for each curve. $M_{partial}$ and M_{full} vs. H are in Appendix **E**, **Fig. E.2**.

From the inset in **Fig 4.4**, we see that H_{EB} changes twice sign during heating. This serves as further proof for the distribution of defect moment freezing temperatures. The defect moments which froze in the negative field direction between 50 K and 100 K dominate EB at 50 K because the defect moments which were frozen below 50 K have melted, thus causing $H_{EB,\,50\,K} < 0$. If the defect moments all had the same freezing temperature rather than a distribution of freezing temperatures, a maximum of one sign change of H_{EB} would be possible, because the defects could dominate at low temperature and the lattice could dominate at high temperature, but it would be impossible to divide defect moments according to their freezing temperatures so that they would dominate EB in different directions at different temperatures.

4.4: Third switching experiment: randomizing exchange biasing at low temperature

The switching experiments in sections **4.2** and **4.3** demonstrate that switching may be used to "tune" the value H_{EB}. Other investigations in the literature have shown that EB tuning can be achieved by using different strengths of cooling fields[11-15], and by preparing the sample with different remanent magnetizations at $T > T_N$ and then cooling in zero field[16]. In this section, we demonstrate that switching can be used to "randomize" EB at low temperature. In the M vs. H curve for a zero field cooled sample (**Fig. 4.6**), $H_{EB} = 0$ is expected and observed. We expect each NP to have non-zero H_{EB}, since each NP has a non-zero moment about which the CoO lattice orients during cooling. However, in zero applied field, the distribution of the orientation of the moments above $T_{B,Co}$ is random, and this random distribution is frozen during zero field cooling, which

gives $H_{EB} = 0$ for an ensemble of NPs. We achieve a similar result through a switching procedure.

We used the cooling procedure shown in **Fig. 4.5**. The partial and full samples were cooled from 300 K to 100 K in a -5 T field. At 100 K, the field was switched to +5 T for one minute. The field was then switched to zero, and cooling was resumed to 5 K. M vs. H was measured at 5 K, and then again after heating to 100 K. For comparison, the samples were cooled from 300 K to 5 K in zero field and were measured at 5 K. Remanent magnetization measurements were also performed for the same cooling procedure (**Fig. 4.14**) in section **4.10**. As in section **4.2.1**, M vs. H curves were plotted using $M_{partial} - 0.947M_{full}$ (**Fig. 4.6**). The M vs. H curves for the partial and full samples are included in Appendix **E** (**Fig. E.3**). The values for H_{EB} and H_C were taken from the fit using the procedure developed in section **3.4.3,** and are presented in the inset in **Fig 4.6**.

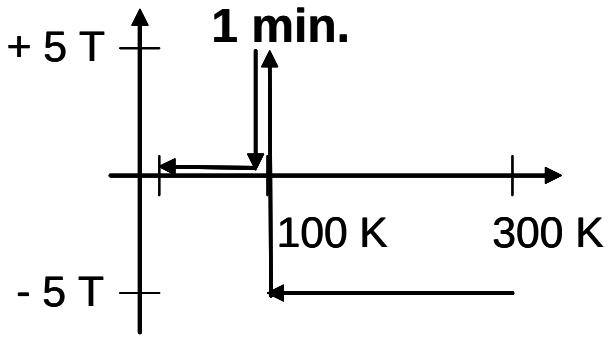

Figure 4.5: Switching procedure for **Fig. 4.6** and **Fig 4.14**

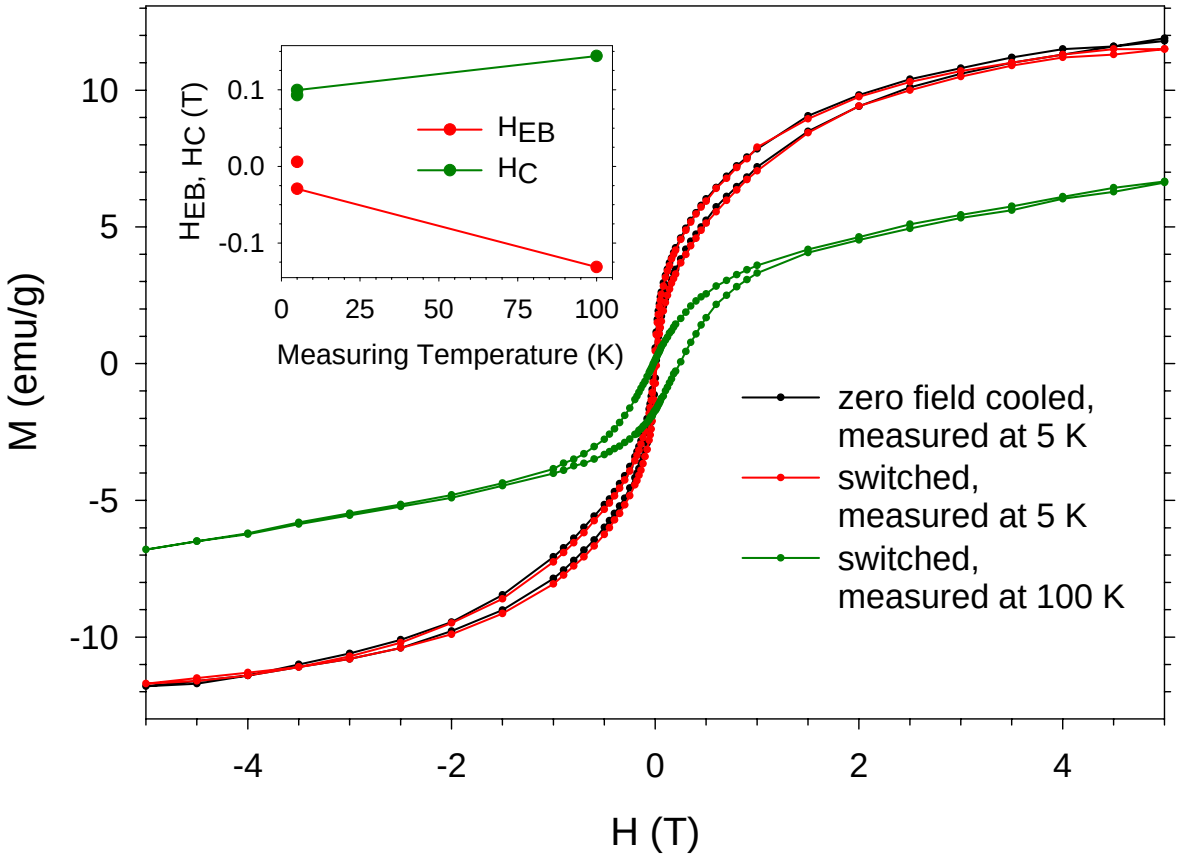

Figure 4.6: ($M_{partial}$ – 0.947 M_{full}) vs. H after cooling from 300 K to 100 K in a -5 T field, then switching to 100 K for 1 minute and cooling to 5 K in zero field and measuring at 5 K and 100 K; compared with zero field cooled curve measured at 5 K; inset: H_{EB} and H_C vs. T from the fit for each curve. $M_{partial}$ and M_{full} vs. H are in Appendix **E**, **Fig. E.3**.

The overlap between the switched and the ZFC curves measured at 5 K is remarkable. When the fitting procedure was applied to the switched curve, $H_{EB,5K}$ = -0.029 T and $H_{C,5K}$ = 0.010 T were measured. For the ZFC curve, $H_{EB,5K}$ = 0.0058 T and $H_{C,5K}$ = 0.093 T were measured. This value of $H_{EB,5K}$ serves as an estimate of the error in the fitting procedure. At 5 K, H_{EB} and H_C for the switched and ZFC curves are quite similar. The cooling procedure could be further optimized to achieve H_{EB} even closer to zero; we expect that could be done by choosing a switching temperature slightly greater than 100 K, so that fewer defect moments would pin the core in the negative field direction.

After heating the switched sample to 100 K and measuring again, $H_{EB,100K}$ = -0.13 T. Therefore, at 100 K, the EB is no longer randomized. A complete understanding of how the randomization occurs at 5 K but not at 100 K is lacking, but the following is a plausible explanation: As the sample is cooled through 170 K, in each partial NP, the CoO lattice begins pinning the core in the negative field direction. As each NP continues cooling to 100 K, some of the defect moments freeze and also pin the core into the negative field direction. Upon switching at 100 K, the defect moments that are not frozen switch into the positive field direction. After switching to zero field, some of these defect moments continue pinning in the positive direction, and they are frozen in that direction as they cool. This process is not well understood because it requires the defect moments to have nonzero coercivity, and may be time-dependent. After cooling to 5 K, the pinning effects of the lattice and defect moments in the negative field direction cancel out with the pinning effects of the defect moments in the positive field direction. This

situation would be different from the ZFC case because in this explanation, each particle has $H_{EB} \approx 0$ T, but single NP measurements would be required to test this hypothesis.

When the sample is heated back up to 100 K, the defect moments that were pinned in the positive field direction have become paramagnetic, so but the lattice and defect moments that froze above 100 K continue pinning the core in the negative field direction. We note that the same value of $H_{EB,100K} = -0.13$ T was obtained using a similar switching procedure in section **4.2.2**. This agreement is expected, since both samples were cooled in a -5 T field from 300 K to 100 K. When they are heated to 100 K and are measured, the memory of the different switching procedures below 100 K is erased.

4.5: Fourth switching experiment: switching to or from zero field

We observed in the first switching experiment (section **4.2.2**) that H_{EB} changes sign during heating if the cooling field is switched at 100 K. In this section, we performed a similar experiment, in which the field was switched between 5 T and zero field, rather than between -5 T and 5 T.

The partial and full samples were cooled in a 5 T field or zero field from 300 K to a 100 K, at which the field was switched to zero field or 5 T, and cooling was resumed to 5 K. This cooling procedure is depicted in **Fig. 4.7**. After cooling, M vs. H (**Fig. 4.8**) and remanent magnetization measurements (**Fig 4.15**) were performed at 5 K. As in section **4.2.1**, M vs. H curves were plotted using $M_{partial} - 0.947M_{full}$ (**Fig. 4.8**). The M vs. H curves for the partial and full samples are included in Appendix **E** (**Fig. E.4**).

The values for H_{EB} and H_C were taken from the fit using the procedure developed in section **3.4.3**. For cooling to 100 K in a 5 T field and then cooling to 5 K in

zero field (black curve in **Fig. 4.8**), $H_{EB,5T,ZFC}$ = 0.41 T and $H_{C,5T,ZFC}$ = 0.16 T. For zero field cooling to 100 K and then cooling in a 5 T field (red curve in **Fig. 4.8**), $H_{EB,ZFC,5T}$ = 0.50 T and $H_{C,ZFC,5T}$ = 0.23 T. These values are consistent with our expectation that the H_{EB} and H_C generated by freezing the defects below 100 K should be greater than those generated by freezing the lattice and the defect moments that freeze above 100 K.

We compare the case of zero field cooling to 100 K and then cooling in a 5 T field with that of the first switching experiment, in which the sample was cooled in -5 T field to 100 K and was then cooled in a 5 T field and measured at 5 K. In the first switching experiment, $H_{EB,switch100K}$ = 0.36 T < $H_{EB,ZFC,5T}$. This is expected because in the first switching experiment, the lattice and defect moments generate EB in the negative field direction, which must be overcome by the 5 T field applied below 100 K.

The case of cooling in a 5 T field and then switching to zero field is similar to the third experiment (section **4.4**), except the initial cooling fields are in opposite directions, and the in third experiment, the samples were switched to 5 T for 1 minute before switching to zero field. The additional switch to 5 T for 1 minute is significant because that curve in (**Fig. 4.6**) closely resembles the zero field cooled curve and has H_{EB} near to zero, but the curve corresponding to cooling in a 5 T field (black curve in **Fig. 4.8**) and then switching to zero field still has large H_{EB} and little resemblance to the zero field cooled curve.

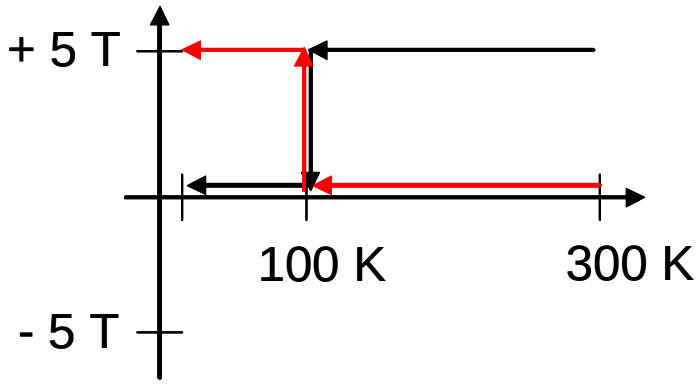

Figure 4.7: Switching procedure for **Fig. 4.8**

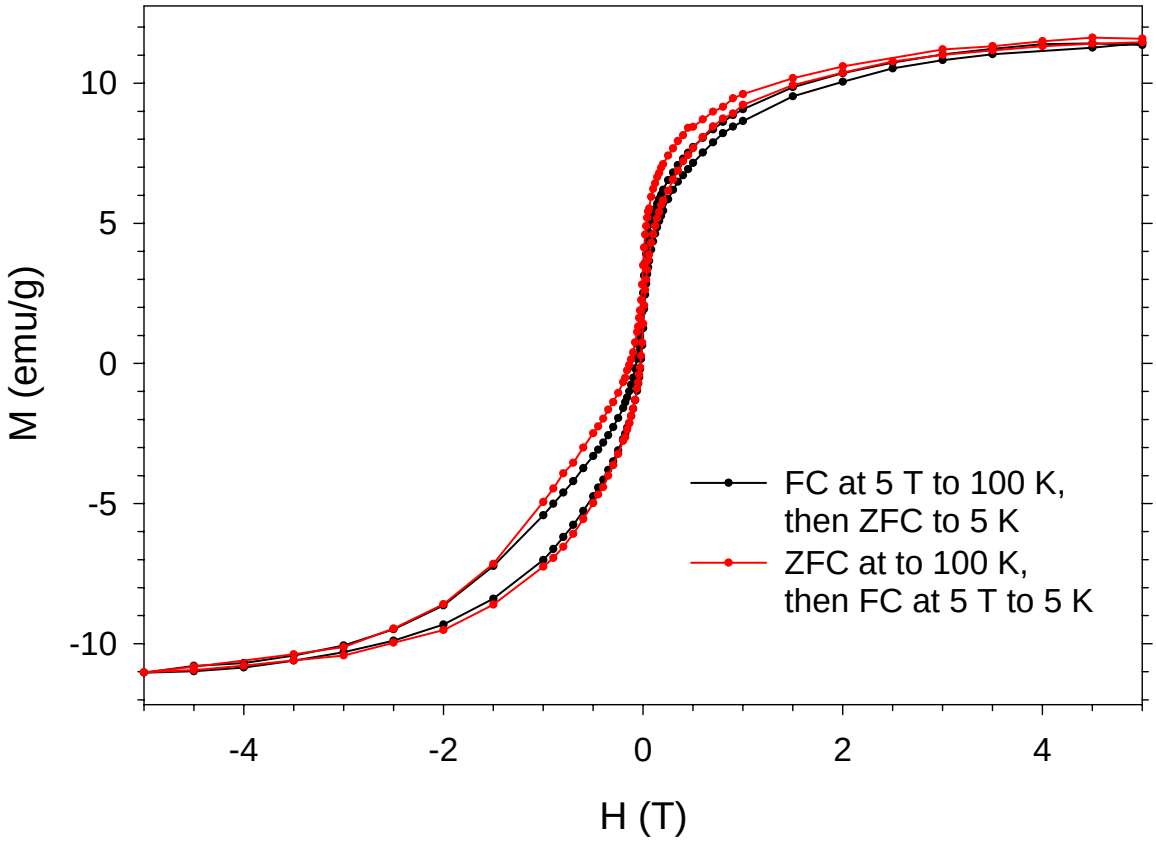

Figure 4.8: ($M_{partial}$ – 0.947 M_{full}) vs. H after cooling from 300 K to 100 K in a 5 T field (black) or zero field (red), then cooling from 100 K to 5 K in zero field (black) or a 5 T field (red). $M_{partial}$ and M_{full} vs. H are in Appendix **E**, **Fig. E.4**.

4.6: Discussion of coercivity

In the first and third switching experiments (sections **4.2** and **4.4**, respectively) H_{EB} can be tuned to values which are near to zero. We compare the M vs. H measurements at 5 K of switching at 50 K in the first switching experiment with those in the third experiment. In the first experiment, $H_{C,\ switch\ 50K} = 0.22$ T $> H_{C,\ third\ experiment} =$ 0.10 T. Although H_{EB} is reduced in both cases, the coercivities and the shapes of the curves differ substantially. In the first experiment for switching at 50 K, two relatively symmetric lobes appear, and the curve in the third experiment has smaller, symmetric lobes.

In both examples, the effects of EB due to the lattice and defect moments that freeze above the switching temperature nearly cancel out with the EB generated by the defect moments that freeze below the switching temperature. However, in the first experiment, switching occurs at a lower temperature (50 K, rather than 100 K). Therefore, the EB generated by the lattice and defect moments that freeze above the freezing temperature should be greater in the first experiment. Here, "greater" means there are more uncompensated spins at the Co/CoO interface that give rise to EB in the negative field direction due to cooling above the switching temperature. We similarly expect the EB generated by the defect moments below the switching temperature in the first experiment to be greater than in the third experiment, since those in the first experiment were cooled in a 5 T field rather than zero field. Thus, the magnitudes of two uncompensated magnetizations at the Co/CoO interface that nearly cancel out in the first experiment are greater than those which nearly cancel out in the third experiment.

A reasonable explanation for the coercivity enhancement in the first experiment which is not present in the third experiment is that although H_C usually scales with H_{EB}, this is not required. H_C has a greater enhancement from two opposing effects of greater magnitude that give rise to EB than from two smaller opposing effects[13]. This explanation also explains why H_C for the ZFC sample is smaller than for a FC sample. The partial NPs in the first and third switching experiments exhibit EB. However, we expect that the 5 T cooling field from 50 K to 5 K generates a greater uncompensated magnetization at the interface than that generated by the remanent magnetization in the third experiment. Although the magnetic field on the surface of a Co NP is 1.2 T (see Appendix **B**), the shape of the magnetic dipole generated by a single NP might lead to less optimal coupling than cooling in a larger, uniform field.

4.7: First switching experiment: thermal remanent magnetization

We now consider the first switching experiment (section **4.2**) from a different perspective. The switching procedure in **Fig 4.1** was used for cooling from 300 K to 5 K for a variety of switching temperatures. After cooling, the field was switched off, and the remanent magnetization was measured during heating. The results for this switching experiment are shown for each sample in **Fig. 4.9**. In the thermal remanent magnetization (TRM) measurement, the sample was cooled from 300 K to 5 K in a constant 5 T field.

The data for the native sample (**Fig. 4.9a**) show that switching has no effect on the magnetization curve. The CoO shell on this sample is too thin to cause EB, and the

sample only "remembers" that it was switched to a 5 T field at some temperature before it was cooled to 5 K.

The measurements of the full sample (**Fig. 4.9c**) have a rise at low temperature, which is similar to the rise in the temperature-dependent magnetization curve (**Fig. 3.9c**). These switching experiments show that the defect moments have a distribution of freezing and melting temperatures. When the sample is heated, the magnetization decreases as defect moments which were frozen in the positive field direction melt. At 5-10 K above the switching temperature, the defect moments which were frozen in the negative field direction begin to melt, and the magnetization increases to zero.

The measurements of the partial sample (**Fig. 4.9b**) are similar to those of the full sample, except the effects of EB on the magnetization of the core are also observed. The total magnetization is higher because of the contribution of the Co core. We note that $M_{TRM,partial,5K}$ = 5.6 emu/g, and $M_{TRM,full,5K}$ = 0.85 emu/g. Therefore, about 5 emu/g of the magnetization in the partial sample is due to the cores. We attribute the low temperature cusp in the TRM for the partial sample to the magnetization of the defect moments in the shell, since the cusp is about 1 emu/g high and is consistent with the steep rise observed at low temperature in **Fig. 4.9c**.

The same qualitative trend is observed in the partial sample as in the full sample: As the sample is heated, the magnetization decreases to a minimum at a temperature which is greater than the switching temperature, and then the magnetization increases towards zero. The physical explanation of the defect moments freezing and melting is the same, but in the partial sample, the defects interact with the core. As the sample is heated from 5 K, the defect moments melt, which leads to a reduction in the EB, and the

core magnetization decreases too. When a temperature 5-10 K above the switching temperature is reached, the defect moments that pinned the core in the positive field direction have melted, but defect moments with higher melting temperatures are still frozen and pin the core in the negative field direction. However, the minimum in the magnetization occurs at a temperature which is 20-40 K higher than the switching temperature. This additional temperature delay for reversing the orientation of the core moment may mean that slightly more thermal energy is necessary for it to change orientations as the pinning caused by the defects in the shell changes. After the minimum magnetization has been reached, EB decreases with increasing temperature, and the magnetization increases to zero.

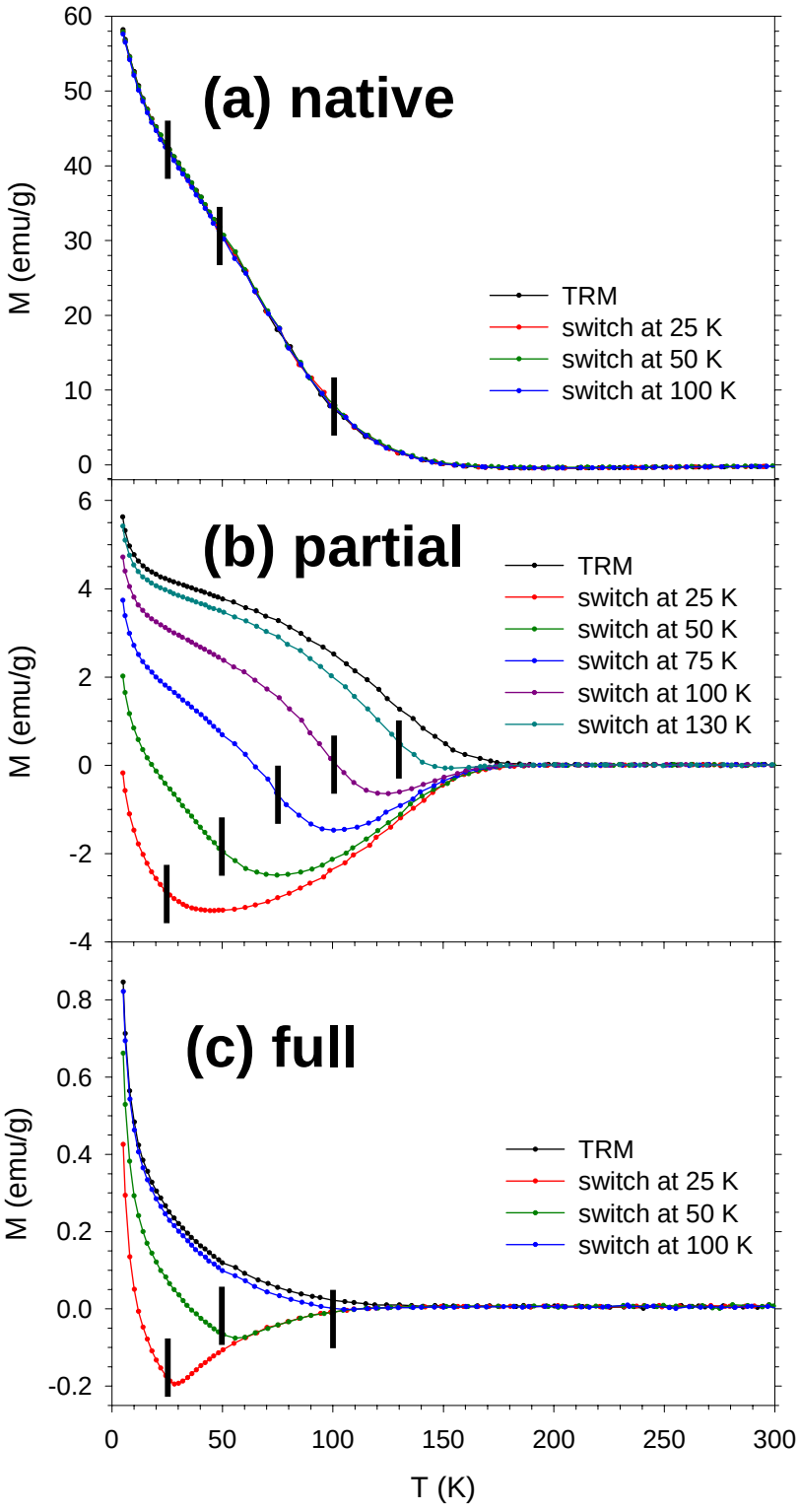

Figure 4.9: TRM and remanent magnetization after cooling from 300 K in a -5 T field, followed by switching to 5 T at a variety of temperatures for **(a)** native, **(b)** partial, and **(c)** full oxidation. The vertical black bars indicate the switching temperatures.

The TRM curve for the full sample is a measure of the total number of frozen defect moments at a particular temperature. The derivative, -d*M*/d*T* of the TRM curves therefore gives the distribution of defect moments' melting temperatures. This derivative plotted in **Fig. 4.10** for each sample. In each plot, the ZFC *M* vs. *T* curve measured in 0.01 T field is also plotted (same as in **Fig. 3.9**), to which -d*M*/d*T* has been scaled by multiplying by scaling factors of 3.39 for the partial sample and 3.63 for the full sample. The scaling factor 21.0 was used for the native sample, but the maxima do not occur at 5 K for both the ZFC *M* vs. *T* and the derivative of the TRM curves for the native sample, as they do for the partial and full samples.

The overlap between the two curves for the full sample in **Fig. 4.10c** is remarkable and unexpected. (Additional measurements of the ZFC *M* vs. *T* were taken down to 2.5 K, and the overlap breaks down below 5 K. These data are presented and discussed in section **4.16**.) The measurements are fundamentally different. The TRM measurement involves cooling in a large field and measuring in zero field, and the ZFC *M* vs. *T* is cooled in zero field and measured in a small field. The derivative of the TRM measurement could be reconciled with the ZFC *M* vs. *T* curve if, in that measurement, each defect moment were to orient in the field when it melted, but then became paramagnetic and quickly decayed to zero magnetization at a slightly higher temperature, thereby causing the ZFC *M* vs. *T* curve to give a distribution of the defect moments' melting temperatures. That physical description is incompatible with the Curie-Weiss Law (and the analysis performed in section **3.4.2**), however, which assumes a constant melting temperature.

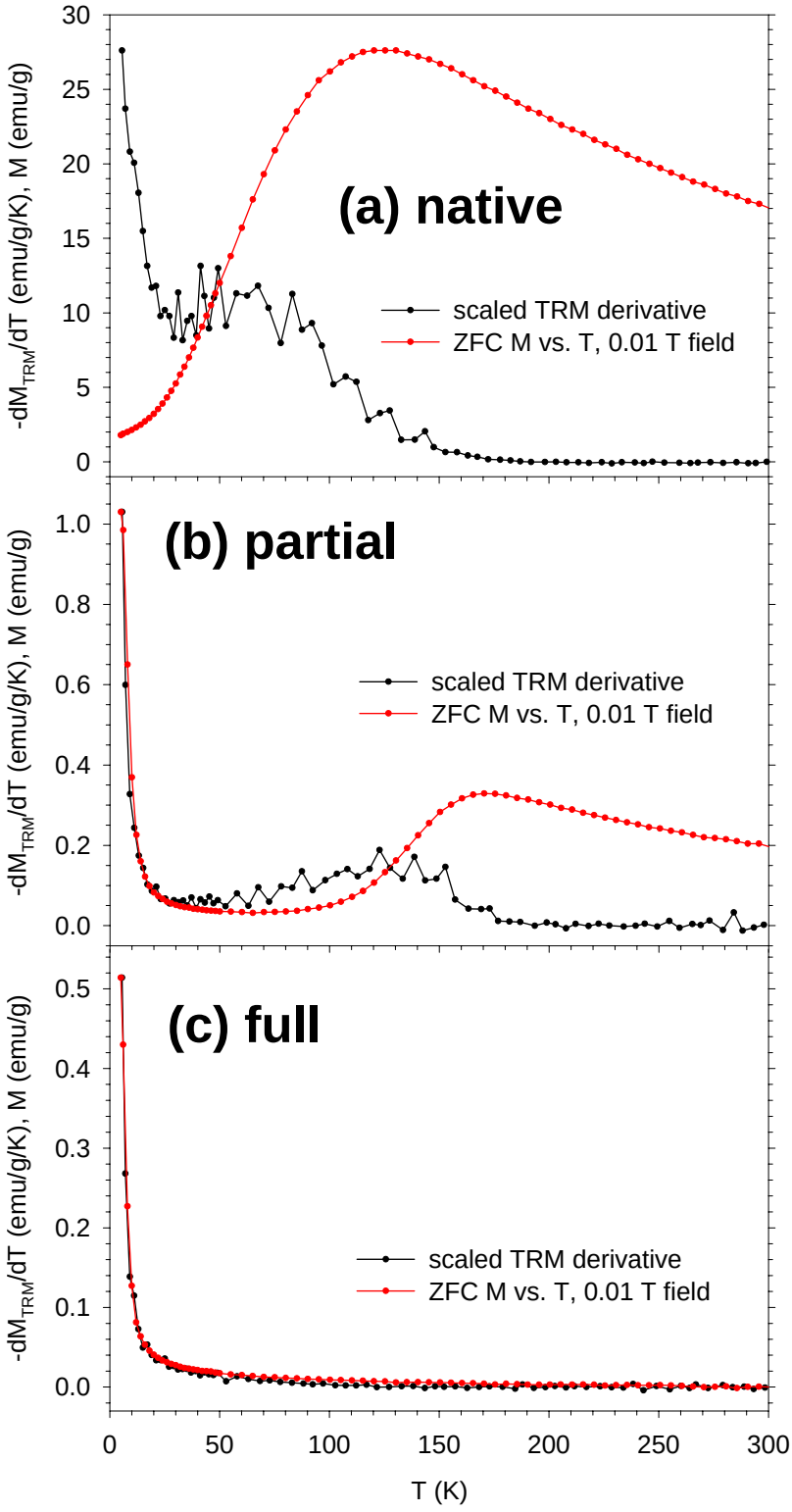

Figure 4.10: Scaled $-dM_{TRM}/dT$ and ZFC M vs. T, measured in 0.01 T field for **(a)** native, **(b)** partial, and **(c)** full oxidation.

Even if the Curie-Weiss analysis is invalid, another way of calculating a lower bound on the moment of the defects is from the TRM data for pure CoO (**Fig. 4.9c**) at 5 K. Their total magnetization of 0.85 emu/g at 5 K corresponds to a moment of 290 μ_B per NP (calculation in Appendix **F**) – which is consistent with the value from the Curie-Weiss analysis.

The scaling factors used to scale -d*M*/d*T* of the TRM curve to the ZFC *M* vs. *T* curves for the partial and full samples are quite similar. The overlap between those curves for the partial sample (**Fig. 4.10b**) is also good at low temperature, as would be expected, since that low temperature rise has the same physical origin as for the full sample. However, at higher temperatures, the peaks in the ZFC *M* vs. *T* curves that correspond to the blocking behavior of the core in **Figs. 4.10a-b** have little, if any, overlap with derivative of the TRM curve. The overlap of these curves that was due to the melting behavior of the defect moments at low temperature does not apply to the blocking behavior of the core, and there are differences in the physical mechanisms that give rise to that part of each curve.

The remanent magnetization curve for the full sample with switching at 100 K nearly overlaps the TRM curve (**Fig. 4.9c**). This (along with **Fig. 4.10c**) indicates that most of the defect moments have melting temperatures below 100 K. However, the TRM curve and the curve for switching at 100 K for the partial sample (**Fig. 4.9b**) are rather different, and significant EB is observed in the *M* vs. *H* curves at 100 K. Even though most of the defect moments have melted at 100 K, there is still significant EB due the remaining frozen defect moments and the CoO lattice.

4.8: Fifth switching experiment: memory effect of repeated switching during cooling

In the switching experiment in the previous section, we showed that the switching during cooling causes a minimum in the remanent magnetization curve for the partial and full samples. In order to test the precision with which the switching procedure could be "remembered" during heating, we switched the magnetization between ±5 T at regular temperature intervals of 10 K, 20 K, and 40 K during cooling, as shown schematically in **Fig. 4.11**. The last switching event was chosen in each case so that the sample would be in a 5 T field at 5 K.

The results of this switching experiment show that the full sample (**Fig 4.12b)** remembers the switching with a high precision, since individual peaks are observed even with a switching interval of 10 K. The partial sample (**Fig 4.12a**) shows individual peaks when the switching interval is 20 K and some oscillations that are not as well resolved when the interval is 10 K. This limitation is probably due to the interaction of the core and the shell and the increase in temperature above the switching temperature that is needed for the core to reorient into the new pinning environment created by the defects.

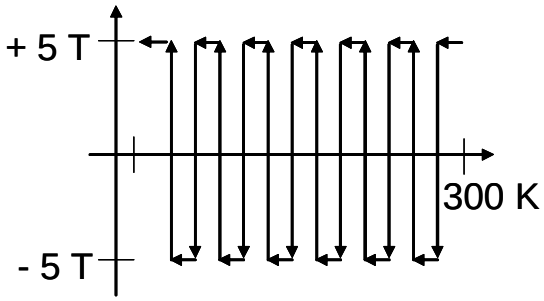

Figure 4.11: Switching procedure

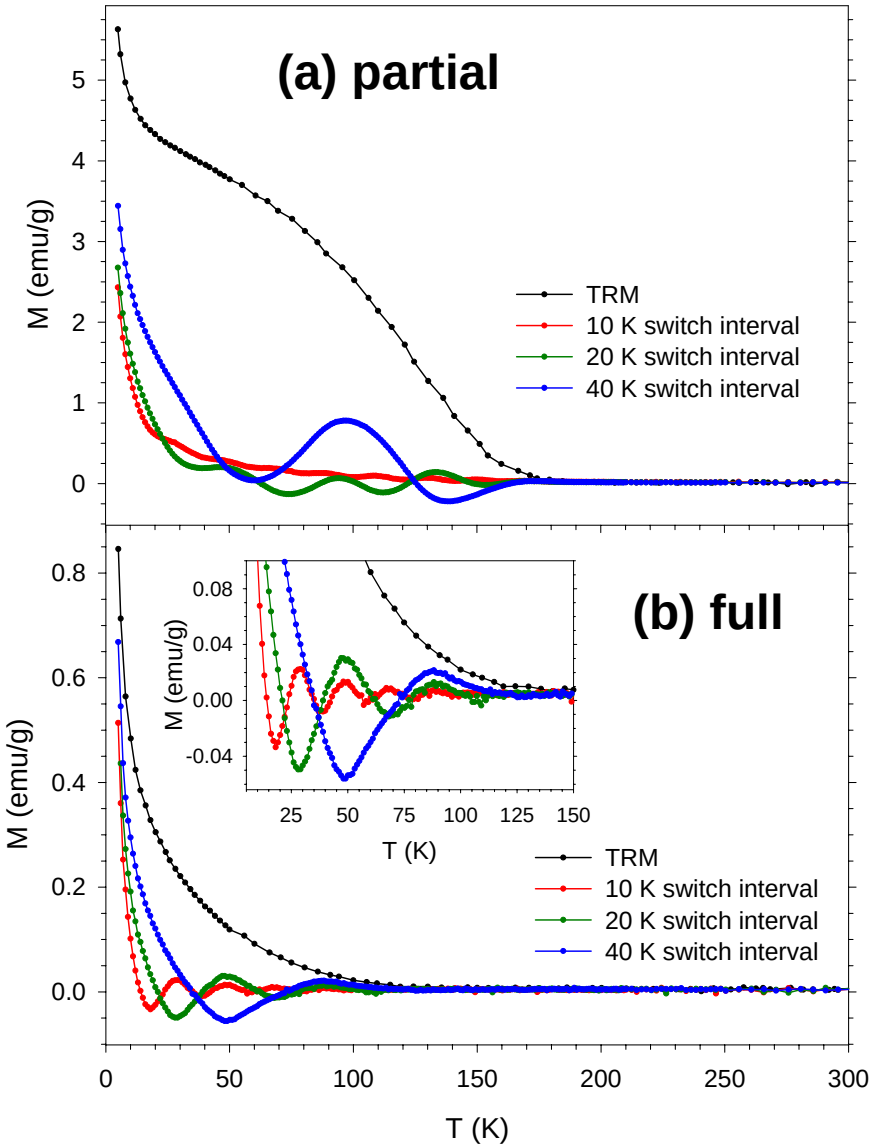

Figure 4.12: TRM and remanent magnetization after cooling from 300 K in a ±5 T field, which was switched at intervals of 10 K, 20 K, or 40 K during cooling for **(a)** partial and **(b)** full oxidation; inset is an expansion of the low temperature region for the full sample.

4.9: Second switching experiment: thermal remanent magnetization

We now consider the remanent magnetization for the second switching experiment. The partial and full samples were cooled from 300 K to 100 K in a 5 T field. At 100 K, the field was switched to -5 T, and cooling was resumed to 50 K, at which the field was switched to 5 T, and cooling was continued to 5 K, as depicted in **Fig. 4.4**. The remanent magnetization, which was measured during heating in zero field, is plotted in **Fig. 4.13**.

The curve for the full sample (**Fig. 4.13b**) has peaks near 50 K and 100 K, which are consistent with the observations for switching once in **Fig. 4.9c**. Similarly, the curve for the partial sample (**Fig. 4.13a**) has peaks near 70 K and 120 K, since slightly greater temperature is needed in order to begin reorienting the cores, which we discussed in section **4.7**. Although the peak in **Fig. 4.13b** at 100 K is very small, the corresponding peak in **Fig. 4.13a** is much larger, which is likely due to EB generated by the CoO lattice, since most of the defect moments have melted at 100 K.

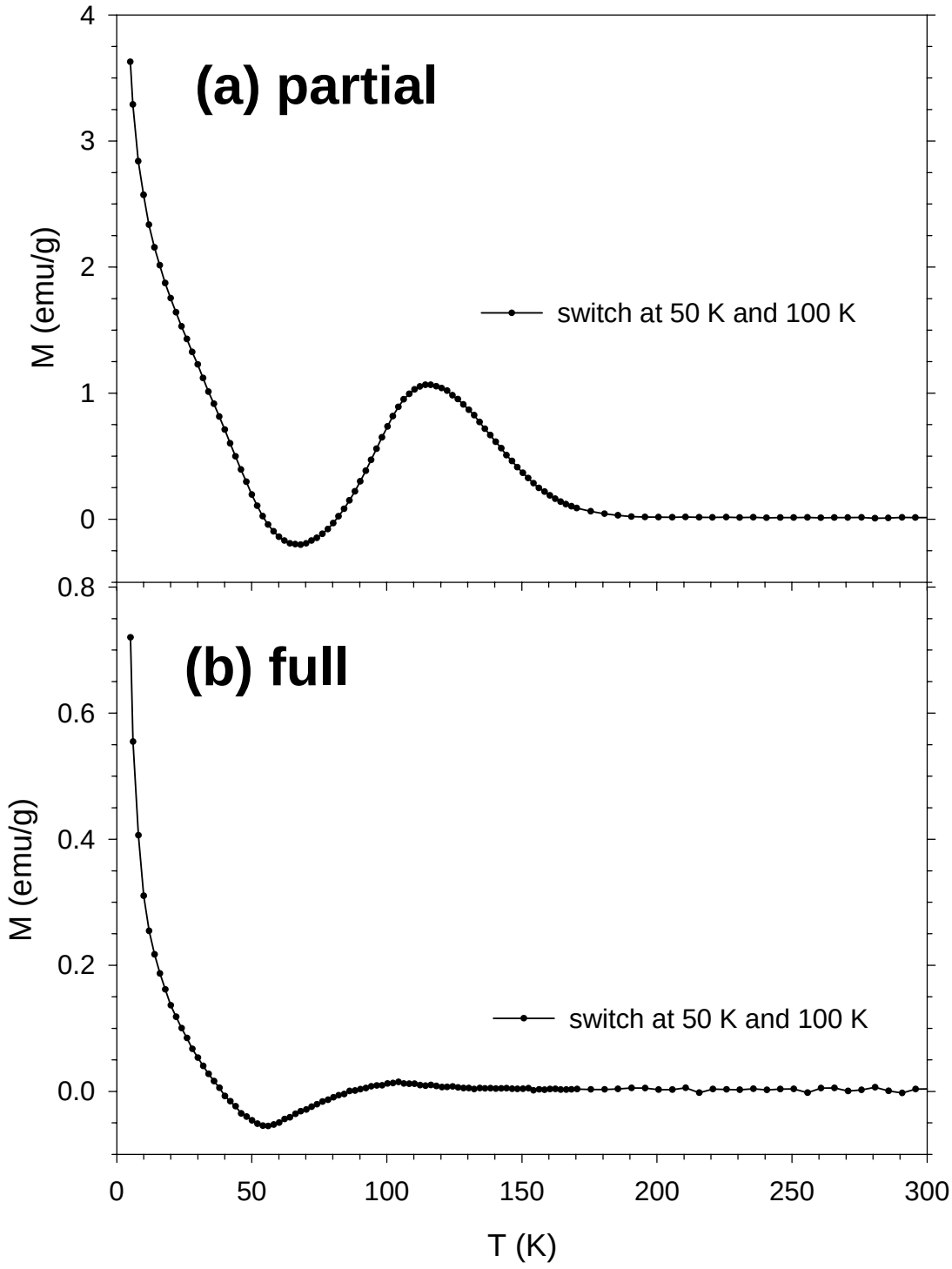

Figure 4.13: Remanent magnetization after cooling from 300 K to 100 K in a -5 T field, from 100 K to 50 K in a 5 T field, and from 50 K to 5 K in a -5 T field for **(a)** partial and **(b)** full oxidation

4.10: Third switching experiment: thermal remanent magnetization

We now consider remanent magnetization measurements which use a cooling procedure similar to the one shown in **Fig. 4.5**. Two new experiments were performed on the native, partial, and full samples using a variety of switching temperatures. The experiments performed on the native sample (**Fig. 4.14a**) were slightly different from those performed on the partial (**Fig. 4.14b**) and full (**Fig. 4.14c**) samples. In the first new experiment, the native sample was cooled from 300 K to a switching temperature in a 5 T field. At the switching temperature, the field was switched to zero, and cooling was resumed to 5 K. In the second new experiment, the native sample was cooled from 300 K to a switching temperature in a -5 T field. At the switching temperature, the field was switched to 5 T for 1 minute, and then to zero field before cooling to 5 K was resumed.

For the partial and full samples, in both experiments, each sample was cooled from 300 K to a switching temperature in a 5 T field. At the switching temperature, the field was switched to zero, and cooling was resumed to 5 K. In the first new experiment, the field was switched directly from 5 T to zero field at the switching temperature. In the second new experiment, the field was switched from 5 T to -5 T for one minute and then to zero field before resuming cooling.

Curves that were cooled in a ±5 T field to the switching temperature and then in the opposite field are shown in **Fig. 4.14** for comparison. (These curves are the same curves as shown in **Fig. 4.9**, except those for the partial and full samples are inverted about the field-axis.) TRM curves with constant 5 T field cooling are also shown in **Fig. 4.14**.

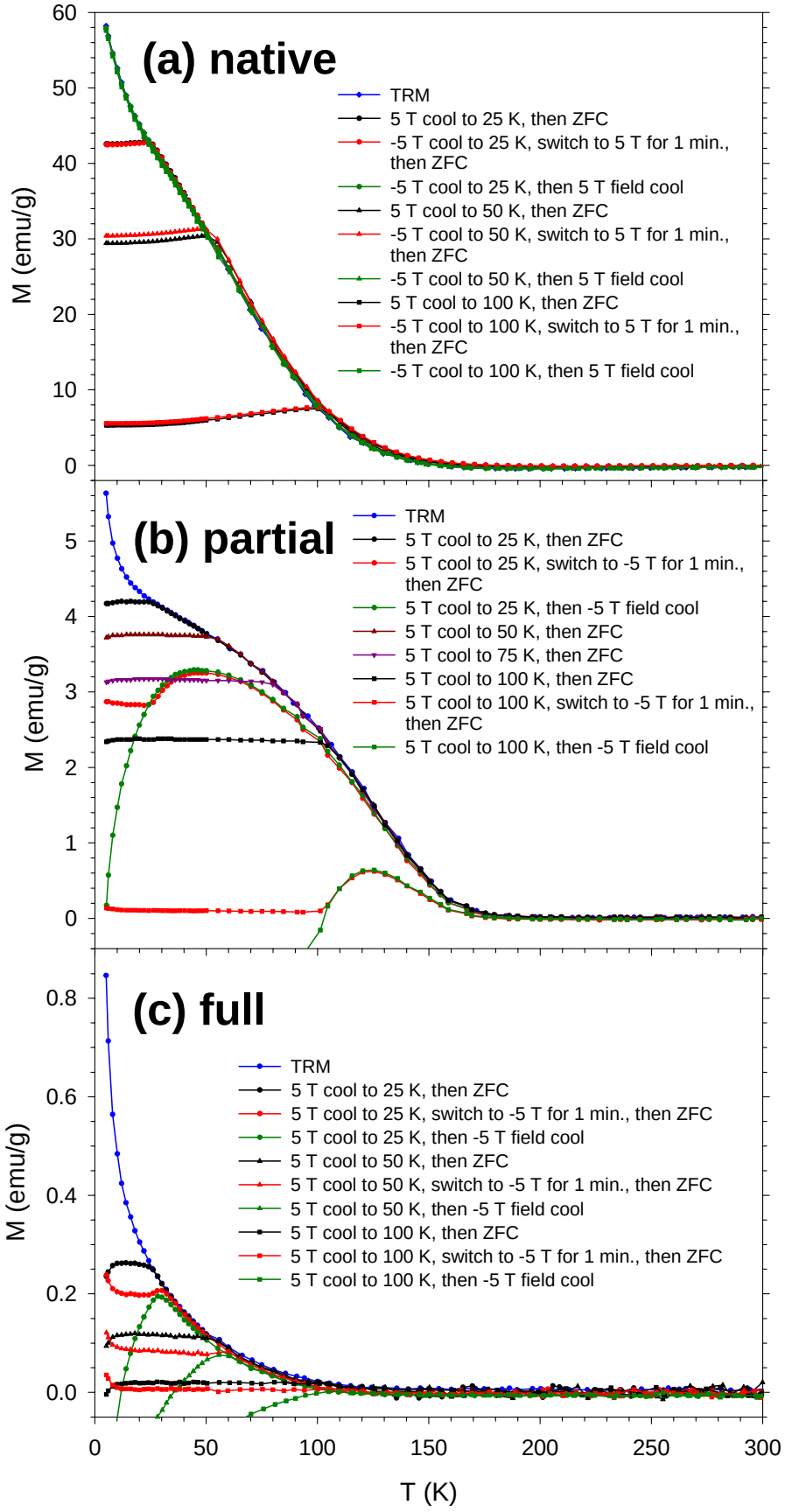

Figure 4.14: TRM and remanent magnetization after cooling from 300 K in a ±5 T field to a switching temperature, at which the field was switched either to zero field, to ±5 T for one minute and then to zero field, or to ±5 T, and then cooling to 5 K for **(a)** native, **(b)** partial, and **(c)** full oxidation.

The results for the native sample (**Fig. 4.14a**) are generally consistent with expectations. For the cooling procedures in which the field was switched to zero field, the magnetization remains nearly constant at the remanent magnetization from the last switching event to a 5 T field prior to switching to zero field and resuming cooling. The data with switching at 50 K have been reproduced, and it is not clear why the two curves with zero field cooling below 50 K do not overlap more closely.

The results for the full sample (**Fig. 4.14c**) for these experiments in which we switched to zero field (black and red curves) at the switching temperature are similar to the results for the native sample: below the switching temperature, the magnetization is roughly constant at the remanent magnetization of the switching temperature. However, in the full sample, the remanent magnetization is determined primarily by the original cooling field of 5 T, rather than the field from the last switching event (which was 5 T for the native sample and -5 T for the partial and full samples). The reason for this difference is because the magnetization in the full sample is from defect moments in the CoO which freeze in the initial cooling field and maintain their orientation even after a field in the opposite direction is applied at a lower temperature.

In the full sample, there are differences between the curves with and without the switch to -5 T for 1 minute before switching to zero field and resuming cooling. The remanent magnetization is lower in the experiment with the 1 minute switch to -5 T. That suggests that some of the defect moments are reoriented and frozen into the negative field direction. There is a bifurcation in these two curves at about 10 K above the switching temperature for switching at 25 K and 50 K. (The signal in the 100 K curves is too low to identify such a point.) Based on this shift of 10 K above the switching

temperature, and a similar observation in section **4.7** of a 5-10 K delay in the minima in **Fig. 4.9c**, a plausible explanation is that the defect moments within 5-10 K of the switching temperature are not yet fully frozen and may be switched in an applied field. If the defect moments are not quickly frozen after switching, there may be some time dependence in the decay of their magnetization after switching to zero field.

The partial sample (**Fig. 4.14b**) shows similar behavior to the full sample, except the magnetization of the Co core and its coupling to the CoO shell through EB are also observed. The bifurcation between the (black and red) curves with switching to zero field at 25 K and 100 K occurs at approximately 70 K above the switching temperature. As was discussed in section **4.7**, we attribute this temperature delay to the increased thermal energy which is needed to rotate the core orientation as the pinning caused by the defects in the shell changes. This comparison between these two curves for the partial sample may also be thought of as an intermediate case between the native sample, in which the final field before switching to zero field primarily determines the remanent field, and the full sample, in which the initial field during cooling before switching primarily determines the remanent field.

The curves for the partial sample with switching to zero field have cusps at 5-10 K above the switching temperature. Those that were not switched to -5 T for 1 minute merge into the TRM curve at this temperature. Those which were switched to -5 T for 1 minute before zero field cooling (red curves) merge in to the curves representing switching to and cooling in a -5 T field (green curves). All other peaks observed in remanent magnetization data for the partial sample after switching during cooling are broader, such as those in **Fig. 4.9b**. These cusps show that when the sample is heated

after switching to zero field, a smaller delay in the temperature is needed to rotate the core orientation as the pinning environment of the defects in the shell changes. The larger temperature delay is caused only when an opposing field has been applied in the switching procedure during cooling.

This last observation makes sense as follows: When the cores are heated after zero field cooling, they are in the remanent magnetization state of the switching temperature. Once the temperature at which the sample was switched to zero field is reached, the defect moments should quickly start to melt, and the magnetization curve should merge into that of the sample which was cooled in a field. The cores do not have to as significantly reorient with zero field cooling as they would if the sample was switched into the opposite field.

In summary, there are two causes for the temperature delay in cusps or minima after the switching temperature in remanent magnetization experiments for the partial sample: (1) The cores will have to unfreeze and rotate to track a more abrupt change in the defects in the shell. (2) If the defect moments with freezing temperatures within 5-10 K of the switching temperature may still be rotated in a large applied field during the switching event, then the switching event causes some cancellation of orientation of the defect moments that was achieved by the initial cooling field. The switching affects not only the orientation of the defect moments that freeze below the freezing temperature, but it also affects those with freezing temperatures within 5-10 K above it. (1) Applies only to the partial sample and to switching into an opposite field. (2) Applies to all switching events in the partial and full samples.

The data in **Fig 4.14** also provide a greater understanding of the *M* vs. *H* curves for the third switching experiment (section **4.4**). The remanent magnetizations for the partial and full samples which were switched from 5 T to -5 T for 1 minute and then to zero field are both nearly zero. This is consistent with the observation that the sample switched according to the procedure shown in **Fig. 4.5** and measured at 5 K (**Fig 4.6**) had low H_{EB} and good overlap with the zero field cooled curve. The fourth switching experiment (section **4.5**) showed that the switching event to the opposite field for 1 minute is required in order to bring H_{EB} to near zero and to cause good overlap with the zero field cooled curve. The data for the partial curve in **Fig. 4.14b** also show a large difference in the remanent magnetizations of the curves which were switched to zero field at 100 K with and without the switch to -5 T for 1 minute beforehand. However, the same curves for the full sample in **Fig. 4.14c** have nearly the same remanent magnetization, which is near to zero. One might look at those two curves in **Fig. 4.14c** and incorrectly assume that the *M* vs. *H* curves corresponding to those cooling procedures would be similar, but we know from the *M* vs. *H* curves of the third and fourth switching experiments (sections **4.4** and **4.5**) that the *M* vs. *H* curves differ greatly.

This last observation underscores an important point. Thermal remanent magnetization measurements provide a wealth of information, but they allow only limited predictions about the *M* vs. *H* curves for the same cooling procedures. A defect moment which maintains its remanent magnetization to a particular temperature may remain frozen with respect to thermal fluctuations, but a 5 T field may be sufficient to reorient it. (This appears to be the case for many of our switching experiments in the 5-10 K windows after the switching temperature.) If a defect moment can be reoriented in a 5 T

field, then it is unable to pin the Co core and will not cause EB in an *M* vs. *H* loop which is swept out between ±5 T. Thermal remanent magnetization measurements may guide our expectations, but the only way to know H_{EB} for a given cooling procedure is to measure it from an *M* vs. *H* measurement.

4.11: Fourth switching experiment: thermal remanent magnetization

We now consider remanent magnetization measurements of the fourth switching experiment (section **4.5**). Switching from an initial cooling field of 5 T to zero field was already performed in the previous section. Here, we cooled the partial and full samples from 300 K to a variety of switching temperatures in zero field, switched to 5 T field, and resumed cooling (**Fig. 4.15**). The "TRM" curves were cooled in a constant 5 T field and are shown in **Fig. 4.15** for comparison.

The data for the full sample show what we would expect based on the discussion in the previous section – a decay to zero magnetization within 5-10 K of the switching temperature. The data for the partial sample likewise decay to zero magnetization, but it occurs 30-50 K above the switching temperature, for the same reasons given in the previous section. The curves for both samples with switching at 100 K have reduced magnetizations compared with cooling the samples from 300 K in a 5 T field, but this reduction is relatively small and is consistent with the large value of H_{EB} which was observed for this switching procedure in section **4.5**.

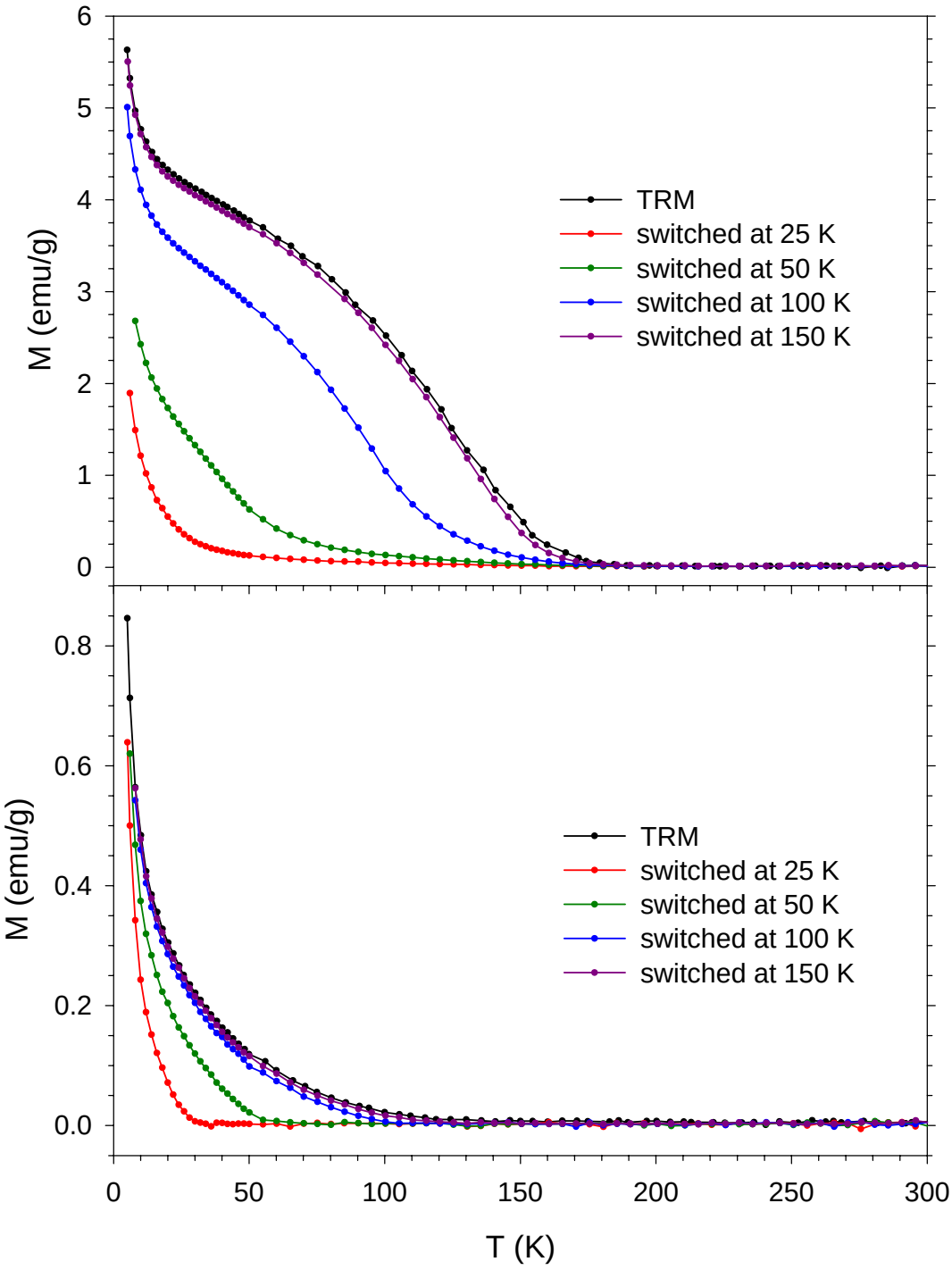

Figure 4.15: Remanent magnetization after cooling in zero field from 300 K to a switching temperature, and then cooling to 5 K in a 5 T field for **(a)** partial and **(b)** full oxidation

4.12: Sixth switching experiment: switching during heating

In the thermal remanent magnetization measurements in the previous sections, we have investigated the effects of switching the cooling field before starting the measurement. We now study the effects of pausing the measurement at a particular temperature and applying a large field, then switching back to zero field and resuming the measurement. The large field perturbs the system so that defect moments which are reoriented in the large field will be observed. Only the defect moments that cannot be reoriented are able to generate EB[17].

In the remanent magnetization curves plotted in **Fig. 4.16**, the partial and full samples were cooled from 300 K to 5 K in a 5 T field, which was then switched to zero field, and measurement proceeded as the temperature was increased. At 50 K and 100 K, the measurement was paused and the field was cycled to -5 T for 1 minute, to 5 T for 1 minute, to -5 T for 1 minute, and then back to zero field. For some of the measurements, after this switching procedure, the temperature was held at 50 K and 100 K, and the magnetization was measured for 1 or 4 hours before increasing the temperature. The purpose of this waiting time was to observe whether moments which were reoriented when the field was cycled would relax, and to observe how quickly this relaxation would occur. The curves identified as "TRM" are included for reference and did not undergo this field cycling as the samples were heated.

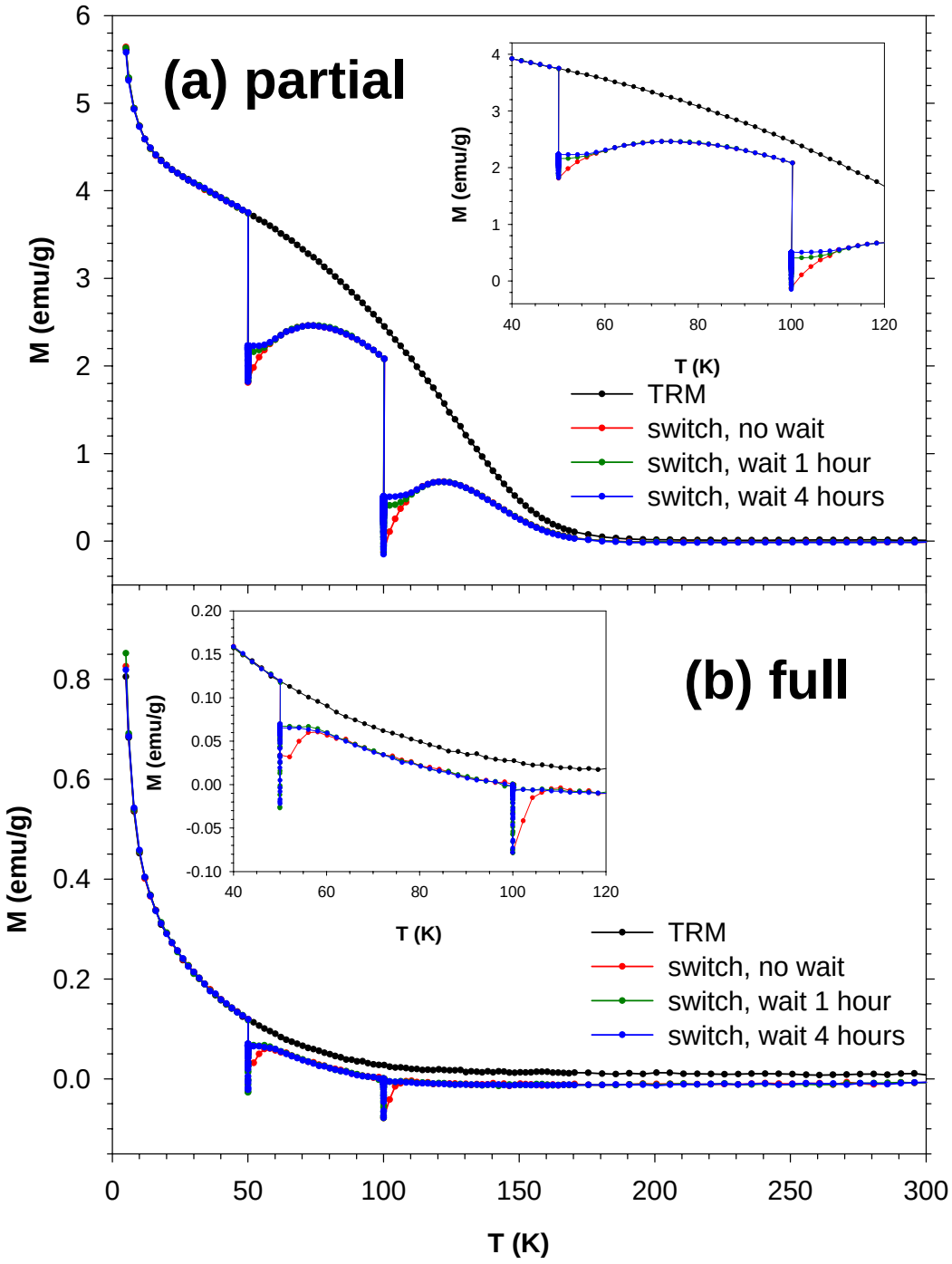

Figure 4.16: TRM and remanent magnetization after cooling in zero field and switching to -5 T (1 min.), then 5 T (1 min.), then -5 T (1 min.), and then to zero field before resuming measurement at 50 K and 100 K for **(a)** partial and **(b)** full oxidation. Insets show greater detail of the same measurements.

In the full sample (**Fig. 4.16b**), the curves with waiting times of 1 and 4 hours overlap. This suggests that most of the relaxation occurs during the first hour. After the cycling at 50 K, the magnetization increases, but not entirely back to the TRM curve. During cycling at 100 K, the magnetization increases nearly to its original value before cycling, but that may be misleading because the original value is close to zero magnetization. When there is no waiting time before resuming the remanent magnetization measurement as the sample is heated, the magnetization curve merges into the curves for which there were 1 or 4 hour waiting times within 5-10 K of the cycling temperature. This shows that the moments which relax during the 1 or 4 hour waiting intervals would relax much more quickly if the temperature were increased by 5-10 K.

Observations of the partial sample (**Fig. 4.16a**) are similar to those of the full sample with a few exceptions: (1) The curves with 1 and 4 hour waiting times do not overlap quite as well as for the full sample, which indicates that relaxation occurs more slowly. This is expected because the cores must also reorient as the defect moments relax after the field is cycled. Most of the relaxation still takes place in the first hour, however. (2) After the field cycling, the remanent magnetization increases to a maximum value at 20-30 K above the switching temperature, even though the magnetization of the defect moments continues decreasing (**Fig. 4.16b**). We attribute this temperature delay in reaching the maximum magnetization to the increased thermal energy which is required to reorient the Co cores as the defects relax after field cycling.

4.13: Seventh switching experiment: switching during cooling and heating

The experiment from the previous section with the field cycling at 50 K and 100 K during heating was repeated with a few modifications: Rather than cooling in a constant 5 T field, the sample was cooled from 300 K to 75 K in a -5 T field, and then from 75 K to 5 K in a 5 T field. At 50 K, the field was cycled as before, but at 100 K, the field was cycled to 5 T for 1 minute, to -5 T for 1 minute, to 5 T for 1 minute, and then to zero field, so that its final direction would oppose that of the initial cooling field at 100 K. The curves that are identified as "TRM" were cooled using the same procedure described here with the field switch at 75 K, but during heating, the field was not cycled at 50 K or 100 K.

The features in the results for the full sample (**Fig. 4.17b**) are the same as they were in the previous section (**Fig 4.16b**), except the TRM curve has a different shape, and the magnetization relaxes into the negative field direction at 100 K. The features in the results for the partial sample (**Fig. 4.17a**) also closely resemble those from the previous section (**Fig 4.16b**). Following the cycling at 50 K and 100 K, the magnetization approaches an extremum 20-30 K after the switching temperature, which is not present in the curve for the full sample.

Although the results in this experiment largely replicate those in the previous section, the switching during cooling is significant, because it enables us to probe the relaxation behavior of EB generated by the defect moments in the CoO shell (field cycling at 50 K) separately from the relaxation behavior of CoO lattice and defect moments with higher melting temperatures (field cycling at 100 K). The relaxation behavior in both regions for both samples has the same qualitative features.

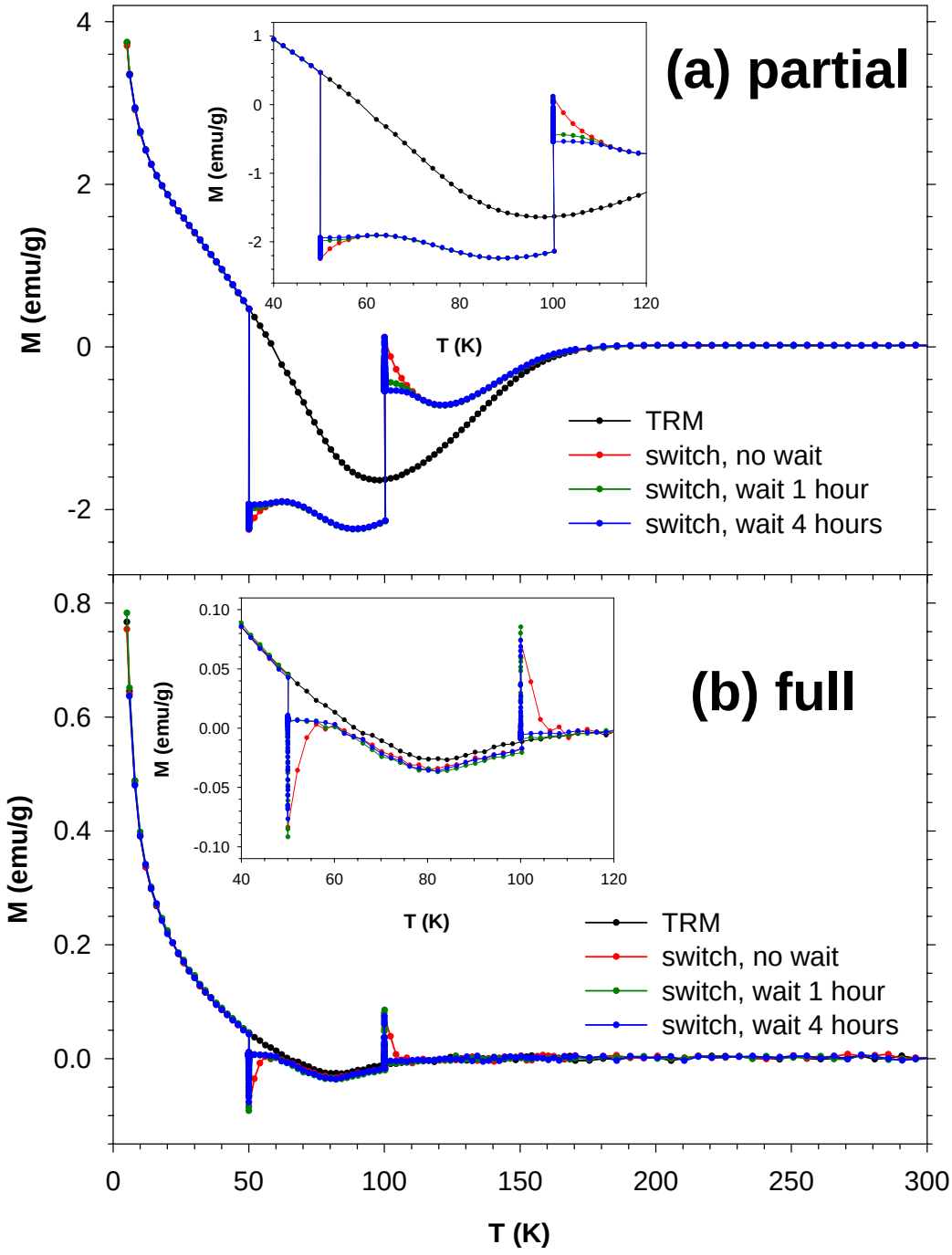

Figure 4.17: TRM and remanent magnetization after cooling in from 300 K to 75 K in a -5 T field, and then switching to 5 T and cooling to 5 K. During heating, at 50 K the field was switched to -5 T (1 min.), then 5 T (1 min.), then -5 T (1 min.), and then to zero field before resuming measurements. At 100 K, the field was switched to 5 T (1 min.), then -5 T (1 min.), then 5 T (1 min.), and then to zero field before resuming measurement for **(a)** partial and **(b)** full oxidation.
Insets show greater detail of the same measurements.

4.14: Thermal remanent magnetization: cooling field dependence

For all of the experiments in this chapter, fields of ±5 T and zero field have been applied. In this section, we investigate the cooling field dependence of the defect moments in the full sample by applying fields of 0.1 T, 1 T, and 5 T during cooling from 300 K to 5 K, and by measuring the thermal remanent magnetization during heating (**Fig. 4.18**).

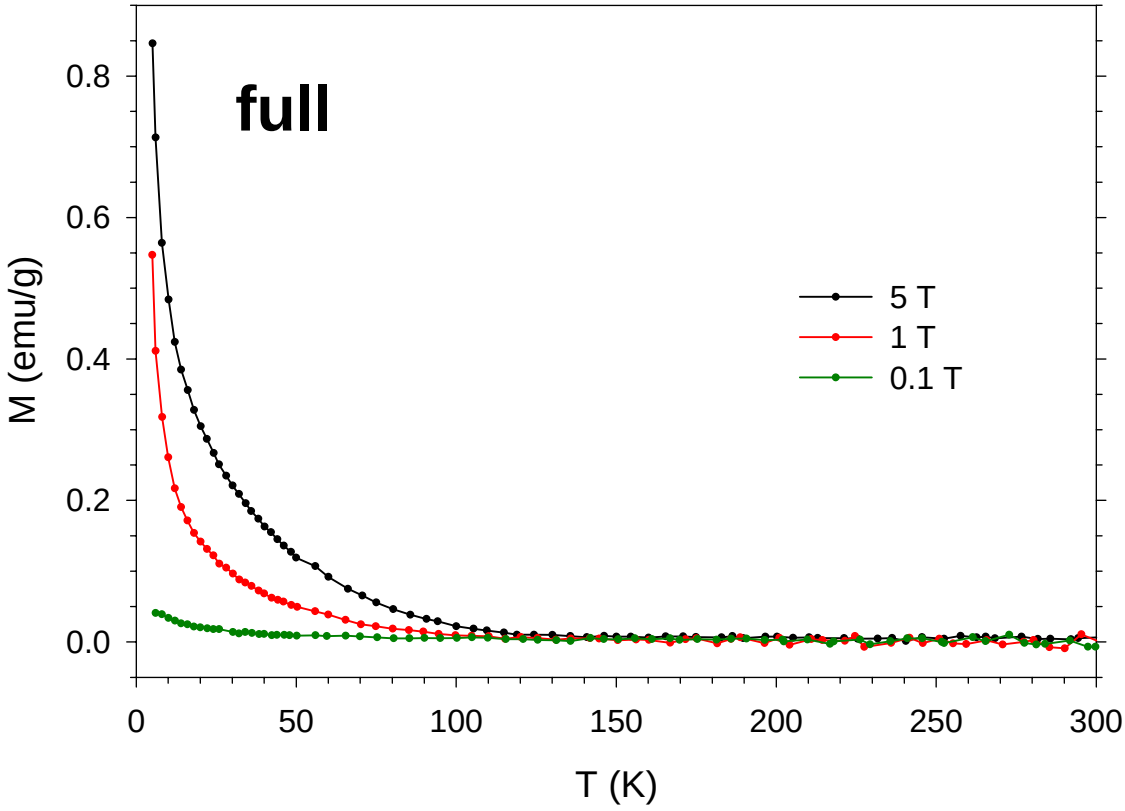

Figure 4.18: TRM of full sample in different cooing fields: 0.1 T, 1 T, and 5 T

The results are unusual: A large cooling field is required to orient most of the defects during cooling. In the remanent magnetization measurements in the previous sections, we have investigated how the defects moments relax to zero magnetization within 5-10 K of their melting. One might expect that such defect moments could be aligned in a small field, but this experiment shows that a large field is required to orient most of them. Further investigation would be required to understand why such a large field is needed to orient most of the defect moments. One possible explanation for this phenomenon is that if the full NPs have a large amount of lattice strain, the lattice strain could help the defect moments relax after melting via magnetoelastic coupling, but a large field would be required to overcome the lattice strain and to orient the defect moments. A similar additional mechanism would be plausible in the partial sample, since the EB coupling between the Co core and the CoO shell lattice and defects probably produces a large amount of lattice strain.

4.15: Magnetic training effect

EB requires the moments in the AFM which pin the FM to be stable during the switching of large fields when M vs. H curves are measured[17]. If the M vs. H curve is measured repeatedly, it has been observed experimentally that H_{EB} decreases during each successive measurement cycle. The physical basis for this decrease is that some of the moments which pin the FM are not stable to multiple field inversion cycles[8]. According to the DS model of EB, the domain structure in the AFM may adapt a more energetically favorable state, in which the pinning is reduced[4, 5]. The field cycling of successive measurements can help the domain structure overcome kinetic barriers in this relaxation

process. The magnetic training effect has been observed previously for other Co(core)/CoO(shell) NPs[18], as well as for Fe(core)/γ-Fe_2O_3(shell) NPs[19].

In **Fig. 4.19**, results for measurements of the magnetic training effect on the partial sample are presented. The sample was cooled in a 5 T field from 300 K to 5 K, and then the first *M* vs. *H* curve was measured during the first cycle. During the second cycle, the second *M* vs. *H* curve was measured. In order to obtain data for many cycles with limited instrument time, additional cycles between those during which an *M* vs. *H* curve was measured were added by switching the field from 5 T to -5 T and then back to 5 T for each additional cycle.

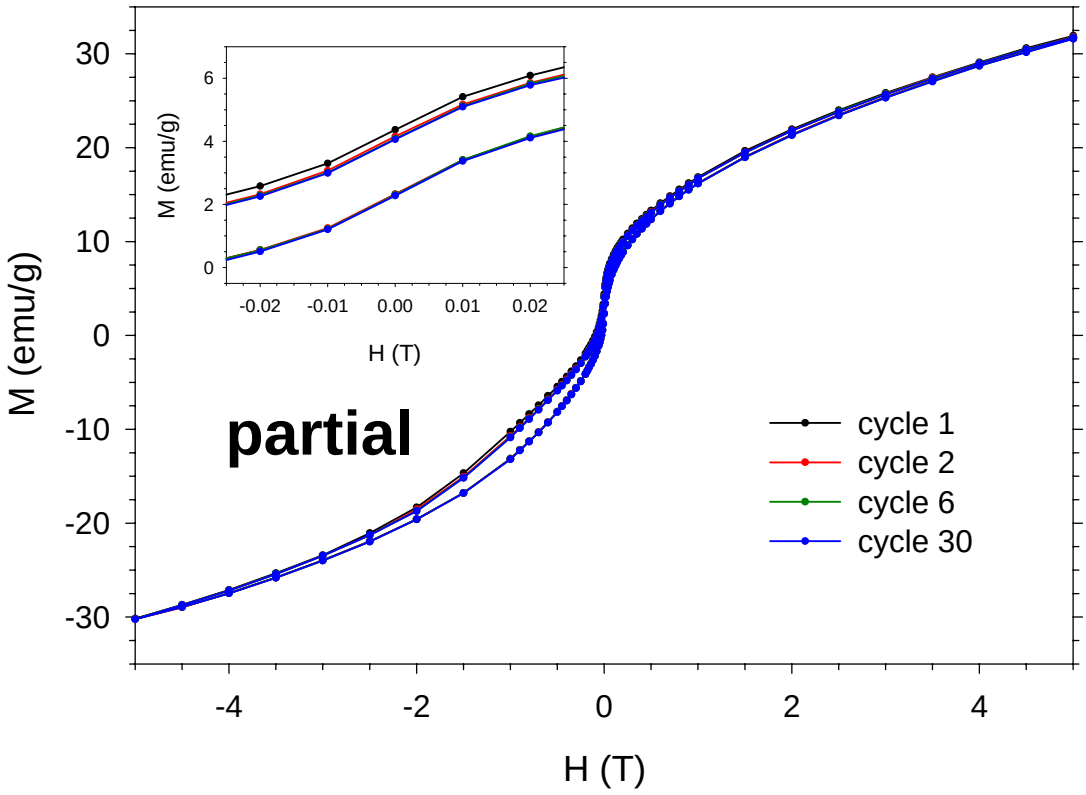

Figure 4.19: Repeated *M* vs. *H* curves of the partial sample after cooling in a 5 T field. The first, second, 6th and 30th curve are shown. The inset shows the region of the curves near to zero field.

The results show that most of the change in the *M* vs. *H* curve and thereby in the EB occurs during the first cycle. There is a smaller amount of change between the second and 6th cycles, and an even smaller amount between the 6th and 30th cycles. This appears to suggest that after infinite cycling, EB would still be present, and that the curve after infinite cycling may not look that different from after 30 cycles. If, on the other hand, there is still a small reduction in the EB during each cycle, then the curve could potentially relax to a case with no EB after infinite cycling.

The magnetic training effect has important ramifications on the suitability of exchange biased NPs for use in magnetic recording. Further investigation would be required in order to determine whether the magnetic training effect precludes the use of exchange biased NPs in magnetic recording, but this result is promising because of the small and decreasing amount of change in the *M* vs. *H* curve with each additional cycle, especially between the 6th and 30th cycles.

4.16: Conclusions and data to 2.5 K

In this chapter, we performed experiments in which switching the cooling field enables tuning of H_{EB} and H_C. These switching experiments have shown that EB generated by stoichiometric and crystallographic defect moments in CoO at low temperatures dominates the EB which is generated by the CoO lattice. This is quite remarkable that such a small number of defect moments in each NP can control its magnetic properties. Using switching experiments, we have studied the magnetic properties of these defect moments and the consequences that changes in the defect moments have on the EB of the Co core in the partially oxidized sample.

However, a recent paper[20] briefly report results of EB in ε-Co NPs which differ significantly from our data. They observed a peak at 8 K in their ZFC *M* vs. *T* measurement of their fully oxidized sample, which corresponds to the rise in the same measurement of our fully oxidized sample. The lowest temperature in our data thus far is 5 K. We hypothesized that the low temperature rise in our ZFC *M* vs. *T* measurement would continue increasing with decreasing temperature. In order to test this hypothesis, we took some additional data down to 2.5 K.

FC and ZFC *M* vs. *T* data were measured while heating the samples in a 0.01 T field (**Fig. 4.20**). The gap in the data between 4.1 K and 4.6 K is due to an instrumental limitation of the SQUID magnetometer. When the magnetometer switches between 4.1 K and 4.6 K, it turns a vacuum off once the temperature is above the boiling point of liquid He. That process causes the temperature to destabilize. When the temperature is raised across the gap, it jumps to about 10 K before cooling stabilizing at 4.6 K. This temperature jump causes an artifact in the ZFC data, unless the measurement procedure is modified to avoid it. In order to take data without the artifact, the field was switched to zero while the temperature was raised from 4.1 K to 4.6 K. After the temperature had stabilized at 4.6 K, the measuring field was turned back on, and the measurement continued.

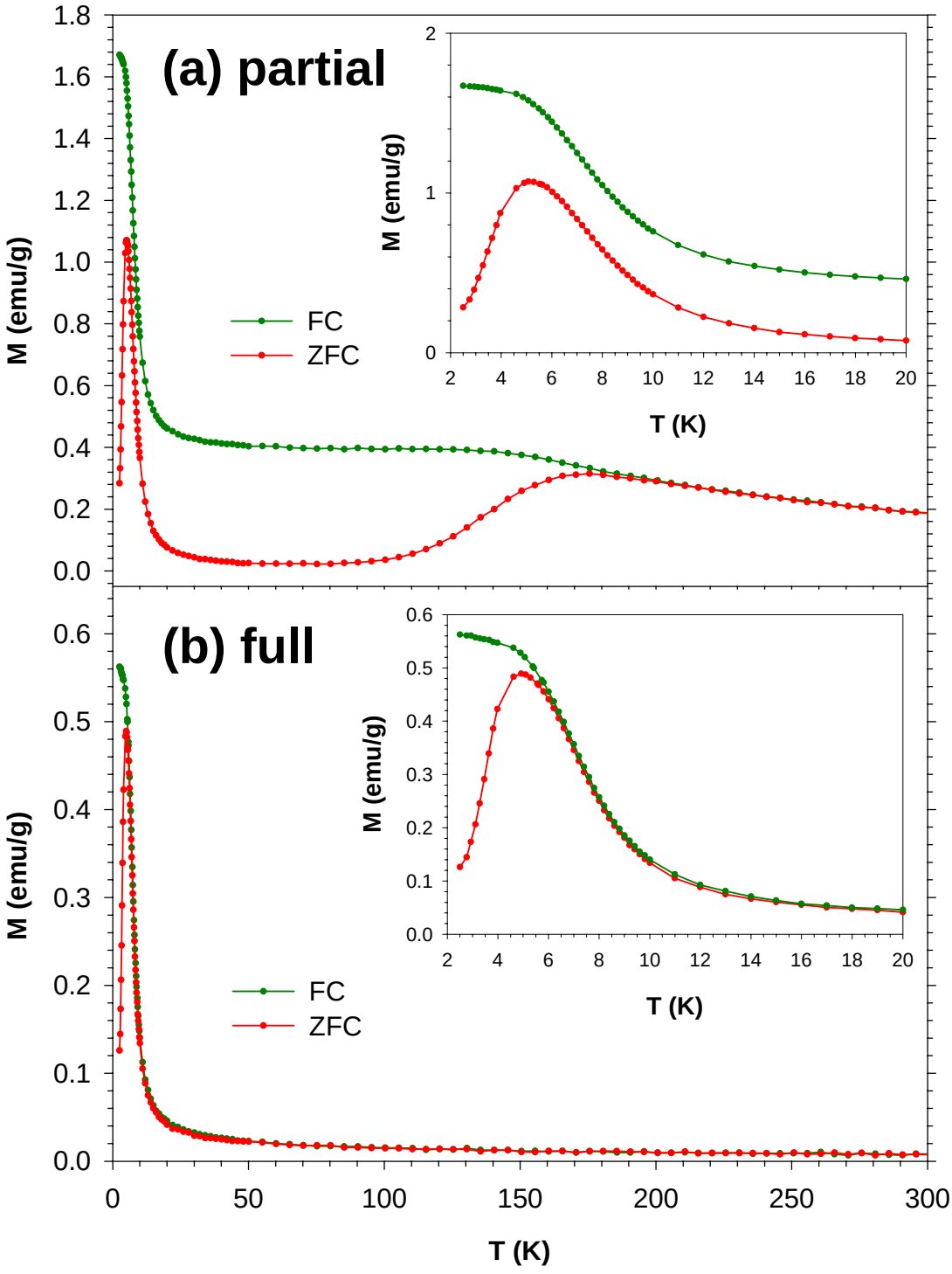

Figure 4.20: Co NPs with **(a)** partial and **(b)** full oxidation:
M vs. *T*: FC and ZFC, cooled to 2.5 K, measured in 0.01 T field.
Insets show greater detail of the same measurements.

The results are unexpected: In the partial and full samples, we observed a peak in the ZFC *M* vs. *T* data at about 5 K. The FC magnetization does not continue to rise as sharply below 5 K as above it. As we discussed in section **4.7**, the ZFC *M* vs. *T* data directly correspond to the distribution of defect moment melting temperatures. The peak in the data indicates that the distribution has as maximum at 5 K.

This result remains consistent with the rest of our analysis, except for one point of disagreement: At low temperature but above 5 K, the ZFC *M* vs. *T* curve for the partial and full samples overlaps with the scaled derivative of the TRM data. Initial TRM data taken to 2.5 K (but which are not shown here because of the artifact caused when going from 4.1 to 4.6 K) indicate that this correspondence does not continue at temperatures below 5 K.

4.17: References

[1] W. H. Meiklejohn and C. P. Bean, Physical Review 105, 904 (1957).

[2] N. C. Koon, Physical Review Letters 78, 4865 (1997).

[3] T. C. Schulthess and W. H. Butler, Physical Review Letters 81, 4516 (1998).

[4] U. Nowak, K. D. Usadel, J. Keller, P. Miltényi, B. Beschoten, and G. Güntherodt, Physical Review B: Condensed Matter and Materials Physics 66, 014430/1 (2002).

[5] J. Keller, P. Miltényi, B. Beschoten, G. Güntherodt, U. Nowak, and K. D. Usadel, Physical Review B: Condensed Matter and Materials Physics 66, 014431/1 (2002).

[6] M. D. Stiles and R. D. McMichael, Physical Review B: Condensed Matter and Materials Physics 59, 3722 (1999).

[7] D. Suess, M. Kirschner, T. Schrefl, J. Fidler, R. L. Stamps, and J. V. Kim, Physical Review B: Condensed Matter and Materials Physics 67, 054419/1 (2003).

[8] J. Nogués and I. K. Schuller, Journal of Magnetism and Magnetic Materials 192, 203 (1999).

[9] K. Takano, R. H. Kodama, A. E. Berkowitz, W. Cao, and G. Thomas, Physical Review Letters 79, 1130 (1997).

[10] T. J. Moran, J. M. Gallego, and I. K. Schuller, Journal of Applied Physics 78, 1887 (1995).

[11] H. T. Shi, D. Lederman, N. R. Dilley, R. C. Black, J. Diedrichs, K. Jensen, and M. B. Simmonds, Journal of Applied Physics 93, 8600 (2003).

[12] J. Nogues, D. Lederman, T. J. Moran, and I. K. Schuller, Physical Review Letters 76, 4624 (1996).

[13] C. Leighton, J. Nogues, B. J. Jonsson-Akerman, and I. K. Schuller, Physical Review Letters 84, 3466 (2000).

[14] J. Nogues, L. Morellon, C. Leighton, M. R. Ibarra, and I. K. Schuller, Physical Review B 61, R6455 (2000).

[15] T. J. Moran and I. K. Schuller, Journal of Applied Physics 79, 5109 (1996).

[16] P. Miltenyi, M. Gierlings, M. Bamming, U. May, G. Guntherodt, J. Nogues, M. Gruyters, C. Leighton, and I. K. Schuller, Applied Physics Letters 75, 2304 (1999).

[17] H. Ohldag, A. Scholl, F. Nolting, E. Arenholz, S. Maat, A. T. Young, M. Carey, and J. Stohr, Physical Review Letters 91 (2003).

[18] D. L. Peng, K. Sumiyama, T. Hihara, S. Yamamuro, and T. J. Konno, Physical Review B: Condensed Matter and Materials Physics 61, 3103 (2000).

[19] R. K. Zheng, G. H. Wen, K. K. Fung, and X. X. Zhang, Physical Review B 69 (2004).

[20] Y. P. Bao, M. Beerman, A. B. Pakhomov, and K. M. Krishnan, Journal of Physical Chemistry B 109, 7220 (2005).

Appendix E for Chapter 4

Supplementary data

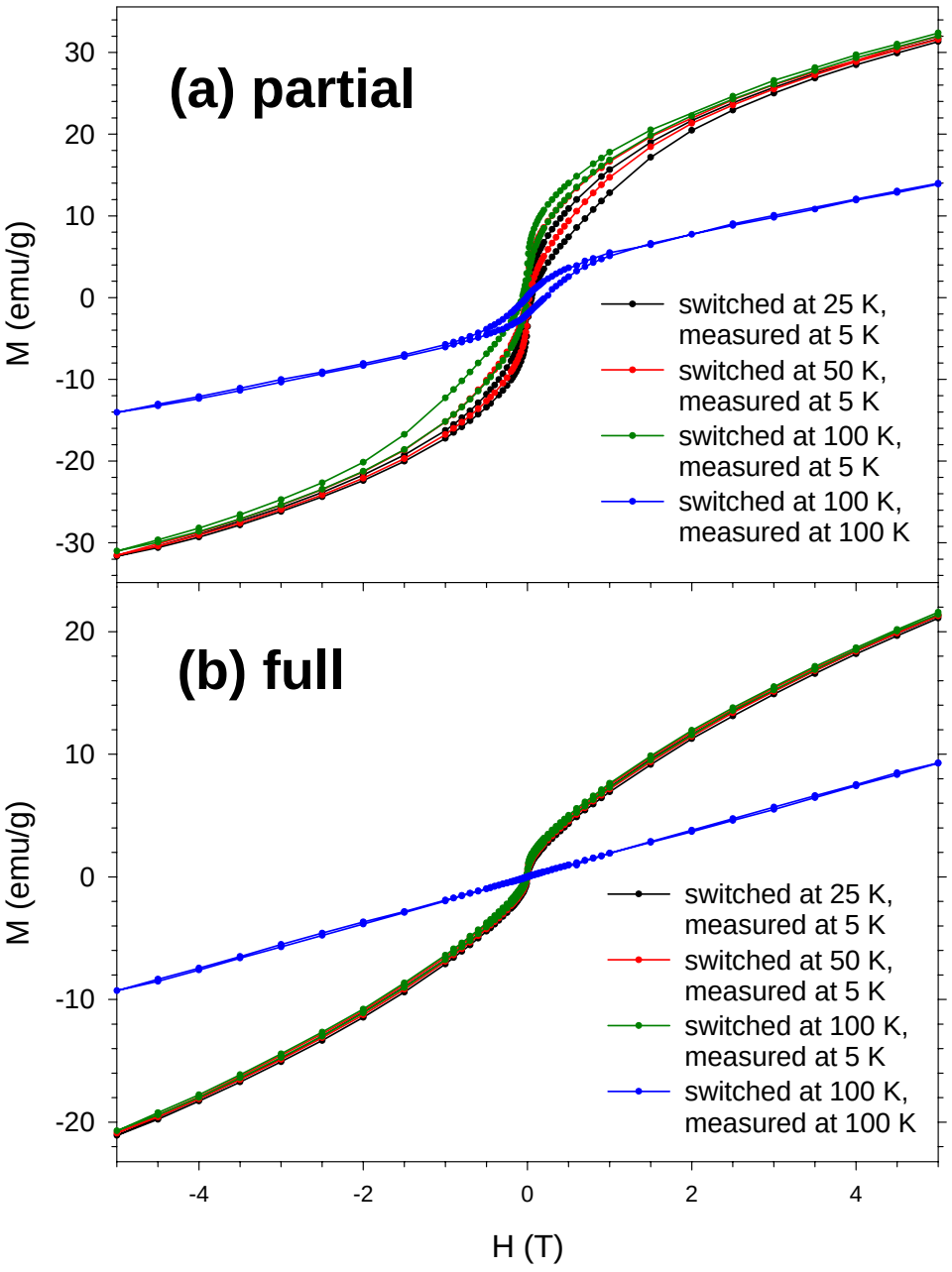

Figure E.1: (Additional data for **Fig. 4.2**) *M* vs. *H* after cooling from 300 K in a -5 T field, followed by switching at 25 K, 50 K, or 100 K for **(a)** partial oxidation and **(b)** full oxidation

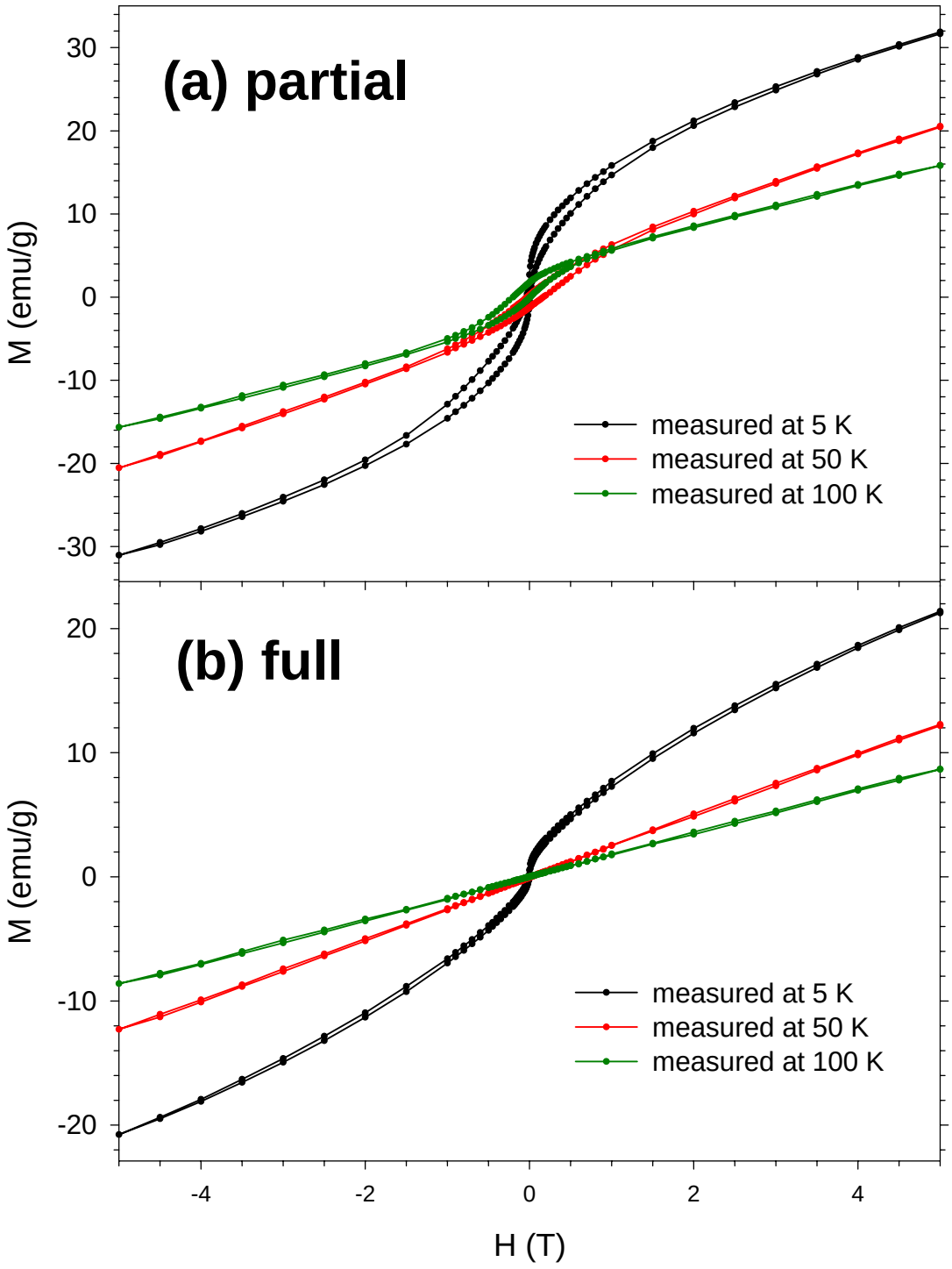

Figure E.2: (Additional data for **Fig. 4.4**) *M* vs. *H* after cooling from 300 K to 100 K in a -5 T field, from 100 K to 50 K in a 5 T field, and from 50 K to 5 K in a -5 T field, followed by measurement at 5 K, 50 K, and 100 K for **(a)** partial oxidation and **(b)** full oxidation

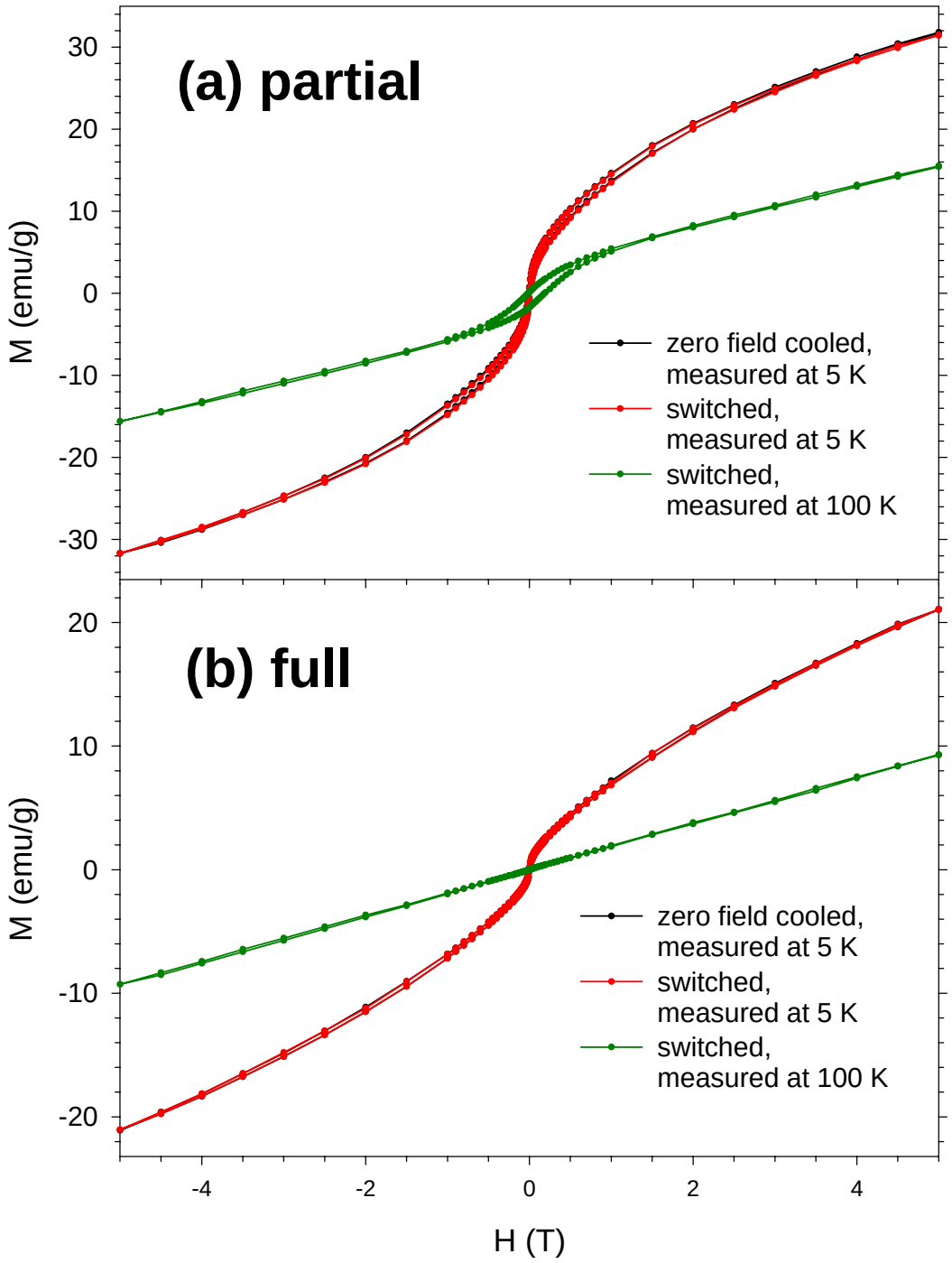

Figure E.3: (Additional data for **Fig. 4.6**) *M* vs. *H* after cooling from 300 K to 100 K in a -5 T field, then switching to 100 K for 1 minute and cooling to 5 K in zero field and measuring at 5 K and 100 K; compared with zero field cooled curve measured at 5 K for **(a)** partial oxidation and **(b)** full oxidation

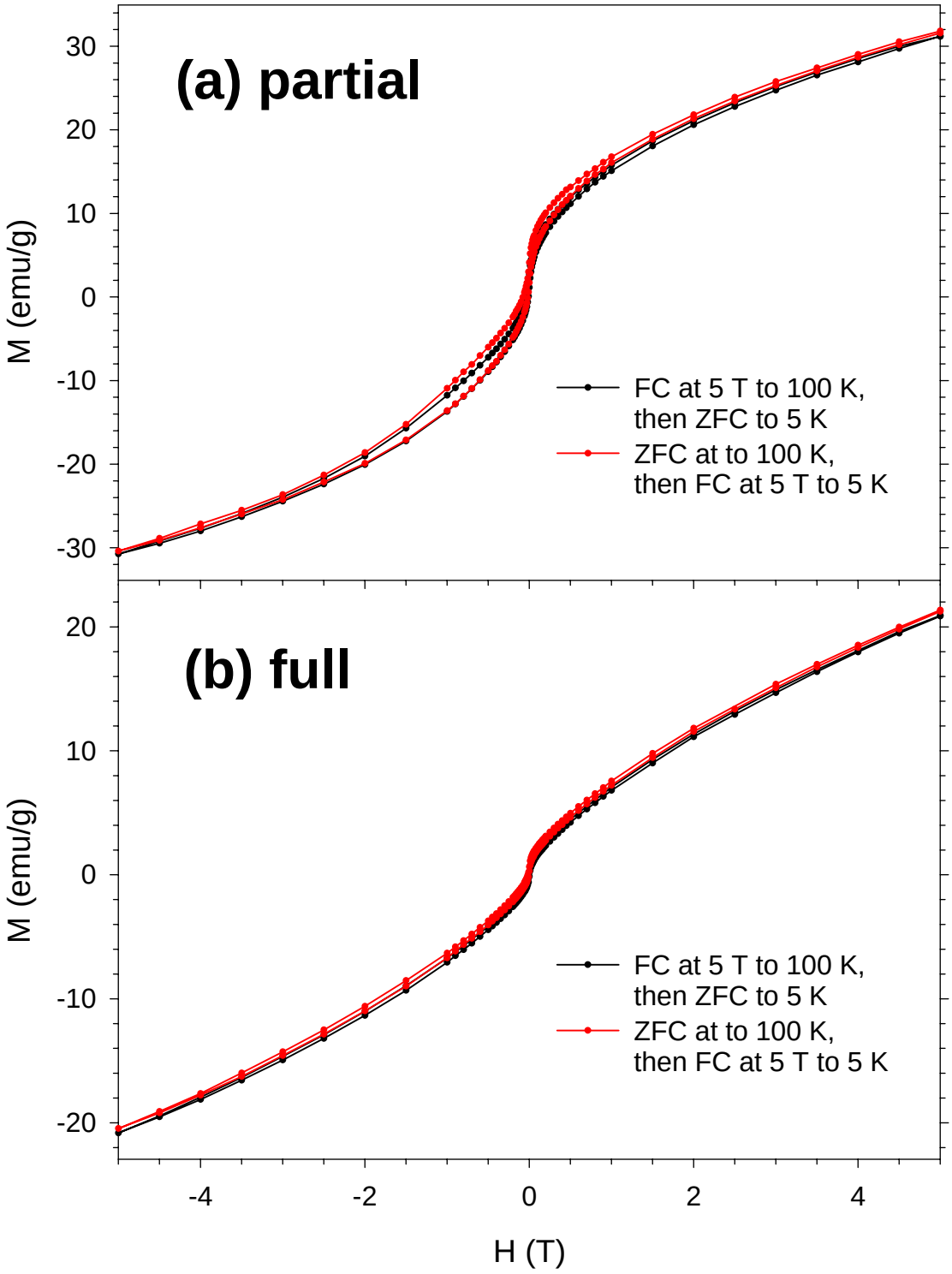

Figure E.4: (Additional data for **Fig. 4.8**) *M* vs. *H* after cooling from 300 K to 100 K in a 5 T field (black) or zero field (red), then cooling from 100 K to 5 K in zero field (black) or a 5 T field (red) for **(a)** partial oxidation and **(b)** full oxidation

Appendix F for Chapter 4

Conversion of thermal remanent magnetization to moment per particle

The details of a calculation which is used in section **4.7** are shown here. The densities of Co and CoO are δ_{Co} = 8.92 g/cm^3 and δ_{CoO} = 6.44 g/cm^3. We convert the TRM magnetization of the full sample at 5 K to emu per unit volume of full NPs and then convert to SI units and to Bohr magnetons:

$$0.846\frac{\text{emu}}{\text{g}}\left(6.44\frac{\text{g}}{\text{cm}^3}\right)=5.45\frac{\text{emu}}{\text{cm}^3}=5450\frac{\text{A}\cdot\text{m}^2}{\text{m}^3}=5.87\times10^{26}\ \frac{\mu_B}{\text{m}^3} \qquad \textbf{(Eq. F.1)}$$

For this calculation, we also need the full NP volume, V_{full}, which is the volume of CoO material excluding the hollow core. We calculate this volume from the native NP core and shell volumes ($V_{Co,native}$ and $V_{CoO,native}$, respectively) using **Eq. F.2**, which assumes that the number of Co atoms per NP was preserved during oxidation:

$$\delta_{Co}V_{Co,native}+\delta_{CoO}V_{CoO,native}=\delta_{CoO}V_{full} \qquad \textbf{(Eq. F.2)}$$

We obtain V_{full} = 4.86 x 10^{-25} m^3. Therefore, the moment per fully oxidized NP is 285 μ_B.

Chapter 5

Iron oxide nanoparticles and their incorporation into silica microspheres with quantum dots

5.1: Introduction

The ferrimagnetic iron oxides, γ-Fe_2O_3 (maghemite) and Fe_3O_4 (magnetite), are attractive for use in biological applications because they are already oxidized and are stable in air and water, unlike Fe or Co. Recently a number of procedures for preparing monodisperse iron oxide NPs with a variety of sizes have been reported [1-5]. In this chapter, we report our preparation and characterization of γ-Fe_2O_3 NPs by following one of these methods[3]. After a discussion of the magnetic characterization, we report initial results for incorporating them into SiO_2 microspheres along with CdSe(core)/CdZnS(shell) QDs. Such composite materials have potential applications in separations, as beads for use in magnetic tweezers[6], and as magnetic resonance imaging contrast enhancement agents. We report preliminary results for manipulating these magnetic, highly luminescent microspheres on a microelectromagnetic device.

5.2: Chemistry and characterization of γ-Fe_2O_3 nanoparticles

5.2.1: Preparation

γ-Fe_2O_3 NPs of diameter 10 nm were prepared according to the method reported by Teng, et al[3], with one exception: 300 μL of $Fe(CO)_5$ was added to 2.2 mL of oleic acid in 15 mL of dioctyl ether at 100 °C. The temperature was increased at a rate of 2 °C per

minute to a final temperature of 275 °C, at which it was held constant for 2.5 hours. After cooling to room temperature, 0.25g of $(CH_3)_3NO$ was added as an oxidizing agent. We chose a shorter oxidation time than Teng, et al used before raising the temperature to 275 °C: The mixture was heated from room temperature to 275 °C at a rate of 6.7°C per minute, and then the temperature was held at 275 °C for 15 minutes before cooling. The NP size can be varied by changing the duration of heating at 275 °C prior to addition of $(CH_3)_3NO$.

After cooling, the NPs were processed for storage by first adding ethanol as a non-solvent to precipitate them. After centrifuging, the supernatant was discarded, and the NPs were redispersed in hexanes. This solution was centrifuged, and any solids were discarded. The NPs were precipitated again by addition of more ethanol. After centrifuging and discarding the supernatant, the NPs were redispersed and stored in THF.

5.2.2: Transmission electron microscopy

Low resolution (**Fig. 5.1**) and high resolution (**Fig. 5.2**) TEM images of the sample show that the sample is quite monodisperse. We did not measure an average diameter from TEM, but we estimate that it is about 10 nm. Both TEM images show that the NPs are faceted. **Fig. 5.2** shows that each NP is single-crystalline.

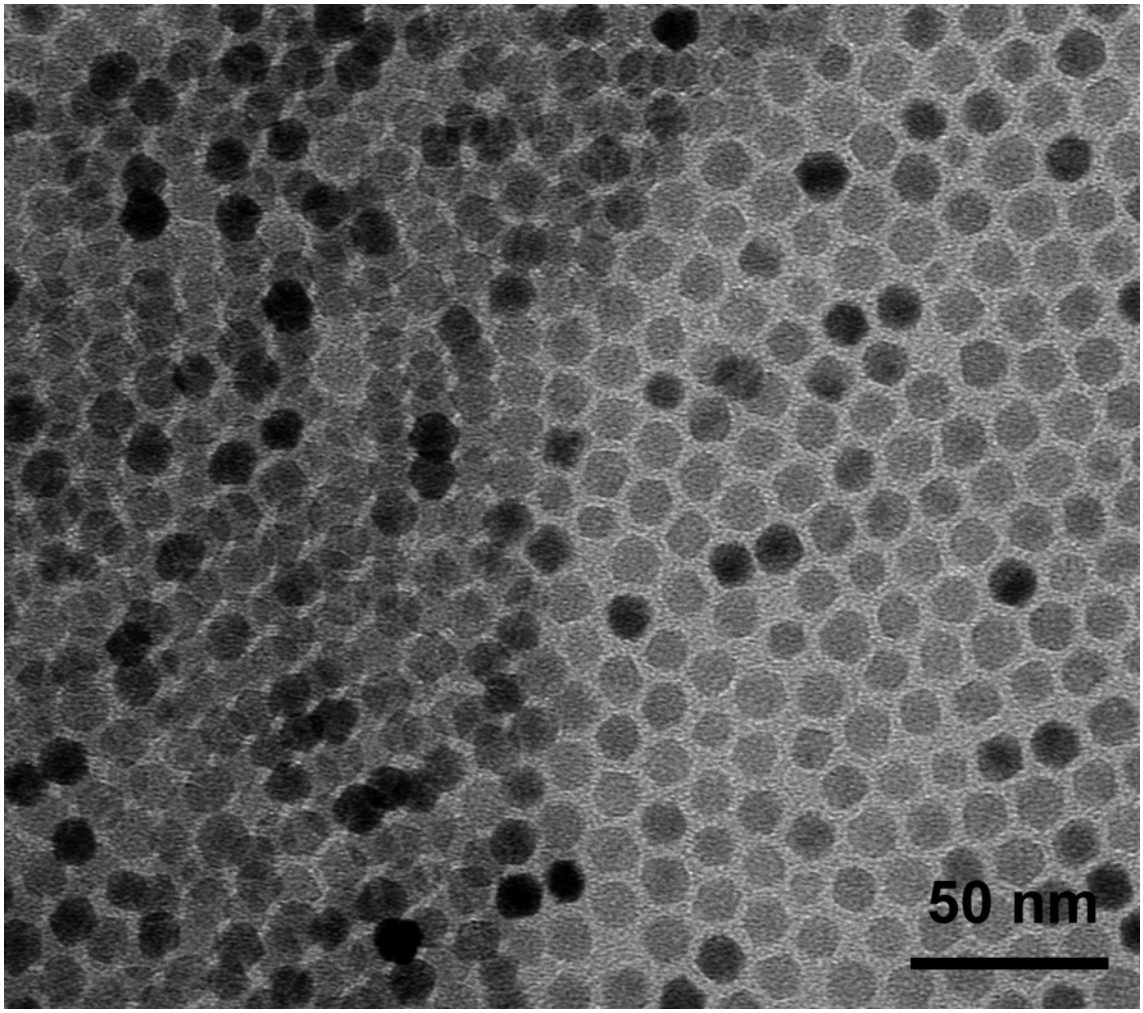

Fig. 5.1: TEM micrograph of γ-Fe_2O_3 NPs

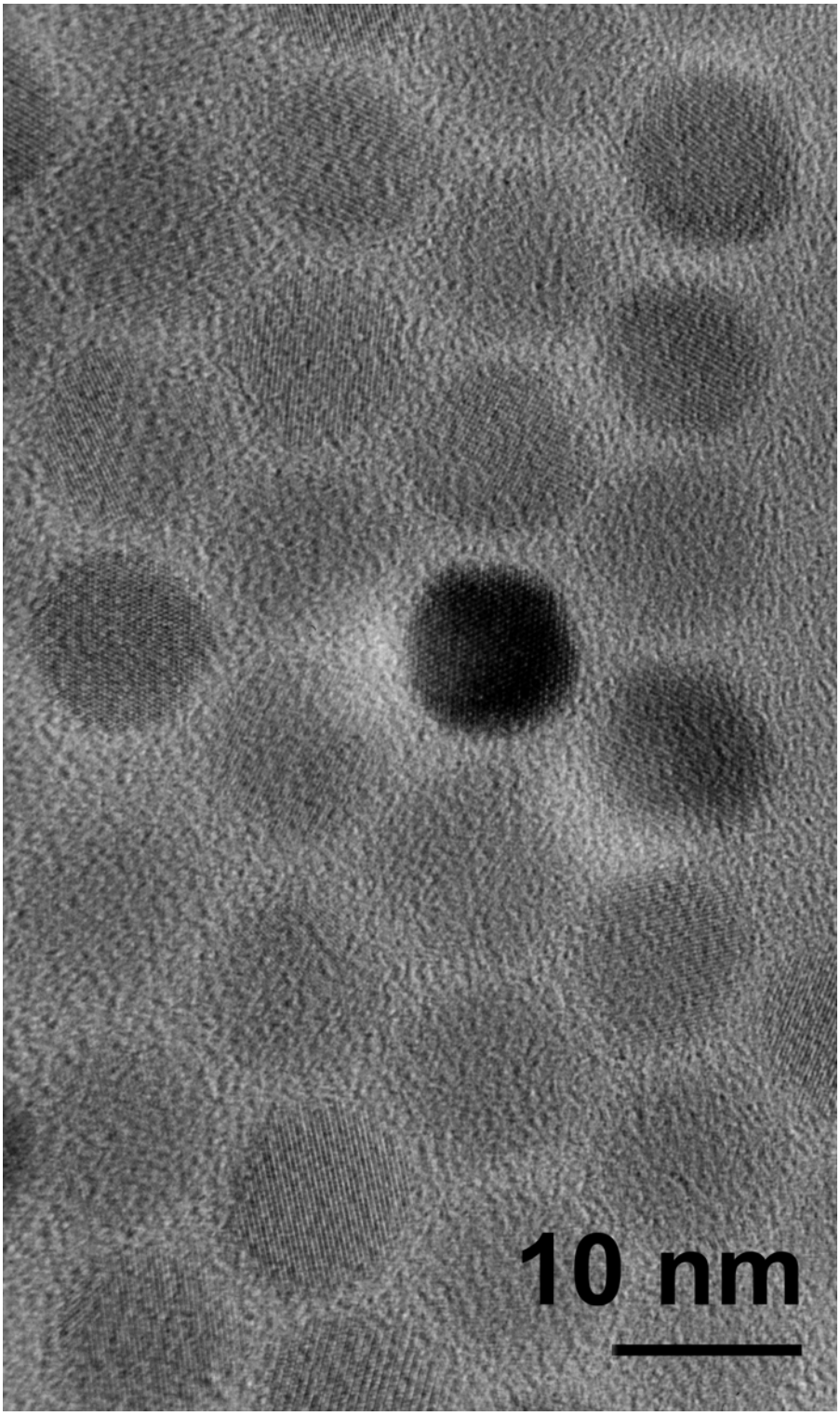

Fig. 5.2: HRTEM micrograph of γ-Fe_2O_3 NPs

5.2.3: Magnetic properties

For the magnetic measurements, three samples were prepared from the same batch of NPs for which the TEM is shown in **Figs. 5.1** and **5.2**. Polymer sticks of the γ-Fe_2O_3 NPs were prepared using the same procedure that is described for Co NPs in section **3.2.2**. A "precipitated" sample was prepared by removing the THF under vacuum and measuring the resulting powder. In order to prepare another sample with a higher packing density, ethanol was added to a concentrated solution of the NPs in THF, and they were sonicated and then centrifuged. The ethanol caused the NPs to precipitate and also removed some of their ligands. After centrifuging, the powder was dried. We call this the "rinsed and precipitated" sample and expect it to have a higher packing concentration because fewer ligand molecules are present to dilute the γ-Fe_2O_3 cores.

SQUID measurements of the zero field cooled M vs. T curve measured with 0.01 T applied field are shown in **Fig. 5.3** for each sample. The blocking temperatures are 80 K, 130 K, and 155 K. This trend of increasing T_B as the packing density of magnetic NPs increases has been observed previously[7, 8]. As the packing density increases, the dipolar coupling between NPs grows. This interaction energy must be overcome by thermal energy in order for the NPs to become superparamagnetic. Therefore, the denser the packing, the higher the thermal energy must be in order to overcome the dipolar coupling, which causes T_B to increase.

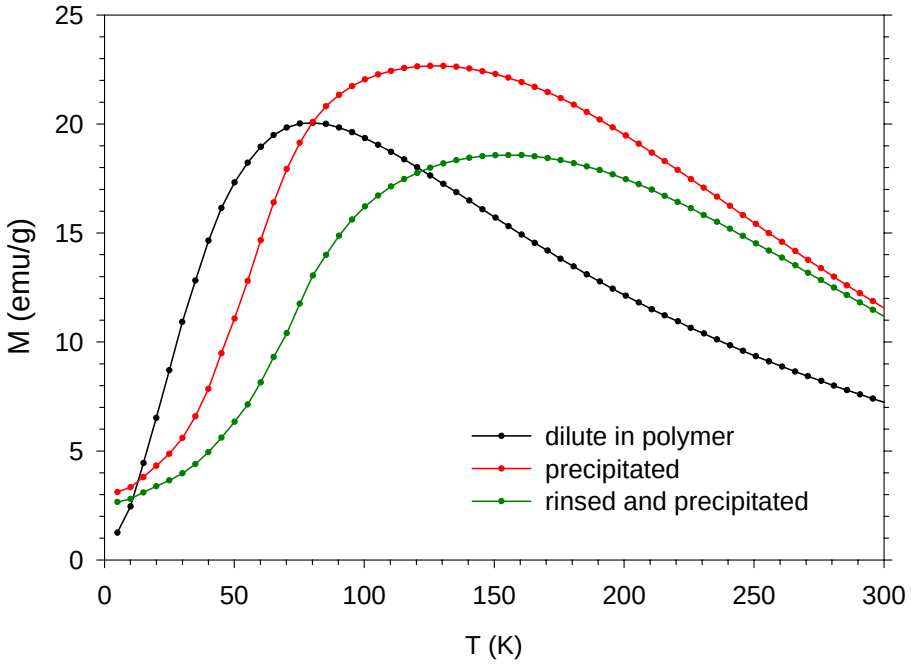

Fig 5.3: Zero field cooled *M* vs. *T* measured in a 0.01 T field for γ-Fe_2O_3 NPs of different packing densities

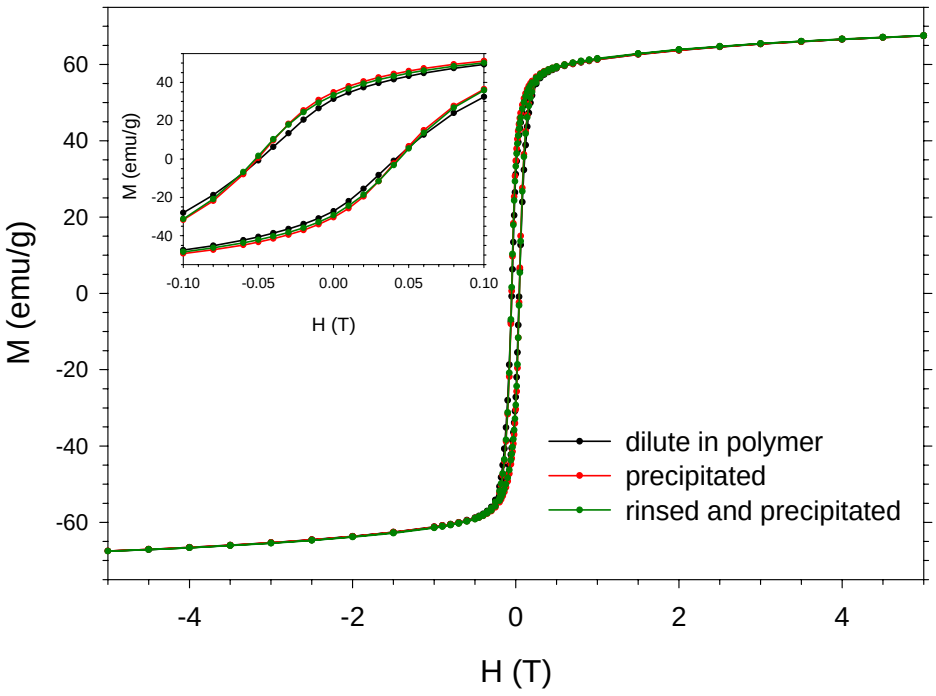

Fig 5.4: *M* vs. *H* at 5 K after cooling from 300 K in a 5 T field for γ-Fe_2O_3 NPs of different packing densities. The inset shows greater detail of the same measurements.

Measurements of M vs. H at 5 K after cooling from 300 K in a 5 T field are shown for each sample in **Fig. 5.4**. In order to calibrate the magnetization scale, a piece of the polymer was sent out for elemental analysis by Galbraith Laboratories, Inc., using inductively coupled plasma – optical emission spectroscopy. The magnetizations of the precipitated samples were scaled to have the same saturation magnetization as the polymer sample of 67.5 emu/g, which is 91% of the bulk value of 74 emu/g[9]. The slight reduction in the saturation magnetization could be attributed to many sources. It is mostly likely caused by the NP surface, possibly by the quenching of the surface moments[10], or by the existence of a different iron oxide phase on the NP surface.

Additional evidence for the presence of a small amount of another form of iron or iron oxide is that the samples exhibit a small H_{EB}, which is shown in **Table 5.1** along with H_C. Because iron has many oxides (see **Table 2.1**), it is rather plausible that an impurity of another oxide could generate the small EB observed here[2].

Sample	H_{EB} (T)	H_C (T)
dilute in polymer	0.0075	0.0451
precipitated	0.0080	0.0467
rinsed and precipitated	0.0082	0.0478

Table 5.1: H_{EB} and H_C for γ-Fe_2O_3 NPs of different packing densities

5.2.4: Discussion of coercivity

Table 5.1 shows that H_C is rather insensitive to the NP packing density, but it increases slightly as the packing density increases. In work done by Gross, et al[8], they report that H_C for precipitated Co NPs is 30% of its value for dilute particles, which is a

rather different result. The discrepancy between our data and theirs suggests that a complete understanding of the behavior of H_C in highly concentrated NPs is lacking. In our work, we cooled the sample in a 5 T field for the M vs. H measurements, which enabled us to observe EB. However, EB also causes H_C to increase. The increase in our case is probably minimal, because the EB is quite weak, but it would be better to use NPs that exhibit no EB, so that EB would be eliminated as a variable in the experiment. The Gross, et al work is subject the same difficulty, however, since their Co NPs may have a CoO shell, which could give rise to greater EB than is observed here.

In section **2.2.3**, we discussed how H_C depends on NP size and the domain structure. In a powder of precipitated NPs, H_C should also depend on the domain structure in the powder. Although there have been some investigations into the domain structure of coupled NPs[11], more experimental work and simulations are needed to fully understand how NPs form domains. We expect the process of domain formation to be quite different in NP powders than in continuous crystals because the ligands quench the exchange interaction between NPs. Therefore, dipolar interactions should dominate. Local variations in the relative crystallographic orientations of adjacent particles would also be important in determining the domain structure, since the NPs have magnetocrystalline anisotropy.

5.3: Incorporation of γ-Fe_2O_3 nanoparticles into SiO_2 microspheres with quantum dots

(The work in this section was done in collaboration with Numpon Insin and John Zimmer.)

5.3.1: Background

Composite nanomaterials containing optically and magnetically active components are desirable for many applications, particularly in biology and medicine. Chan and Zimmer, et al[12] from our lab have developed expertise for incorporating CdSe QDs into SiO_2 microspheres[12]. We are in the process of extending their method to incorporate γ-Fe_2O_3 NPs into the same shell as CdSe QDs. Such a composite material, especially with a total diameter of or below 100 nm, would be of interest for many applications.

5.3.2: Preparing the nanoparticles for incorporation

High quality bare SiO_2 microspheres are available commercially, or they may be prepared according to literature methods reported by Chan and Zimmer et al[12]. Smaller bare SiO_2 microspheres may be prepared according to other literature methods[13]. The incorporation method of Chan and Zimmer et al[12] requires that the NPs be made ethanol-soluble through ligand exchange. Since each type of NP has different surface chemistry, the ligands which bind to the NP surface and impart ethanol solubility may be different for each type of NP.

When an excess of 12-hydroxydodecanoic acid or 5-aminopentanol is added to a solution of the γ-Fe_2O_3 NPs in THF, and then the THF is removed by vacuum, the precipitate is dispersable in ethanol. The quality of the dispersion depends on the concentrations of the ligand and NPs and whether the mixture was heated after adding ethanol to further promote the ligand exchange.

5.3.3: Incorporation

The method of incorporation is still under refinement for different sizes of NPs and SiO_2 microspheres. We describe a typical procedure here which consists of three steps:

(1) Ligand exchange was performed to bring the γ-Fe_2O_3 NPs into ethanol: In a typical procedure, ethanol was added to the solution of γ-Fe_2O_3 NPs (of about 7.0 nm in diameter) in THF in order to precipitate them. After centrifuging, the supernatant was discarded, and the NPs were dried under vacuum. This powder, which had a mass of 6 mg, was introduced into a nitrogen-atmosphere glovebox, in which 140 mg of a 50% (by mass) mixture of 5-aminopentanol (AP) and anhydrous ethanol and an additional 270 mg of anhydrous ethanol were added. The mixture was heated at 40 ^{0}C until the NPs were well dispersed, after which 50 mg of 3-aminopropyltrimethoxysilane (APS) was added. The solution was then heated for another hour to ensure cap exchange with AP and APS. For larger sizes of γ-Fe_2O_3 NPs, more ethanol and AP were needed in order to redisperse the NPs in ethanol.

(2) The CdSe/CdZnS NPs were dispersed in ethanol using the technique of Chan and Zimmer, et al[12]: In a typical procedure, 26 mg of CdSe/CdZnS NPs was mixed with 195 mg of anhydrous ethanol, 29 mg of APS, and 54 mg of AP. The mixture was then heated to 40 ^{0}C for about 1 hour, leading to the formation of a well-dispersed solution of CdSe/CdZnS NPs.

(3) The γ-Fe_2O_3 and CdSe/ZnS NPs were incorporated into the SiO_2 shell simultaneously: In a typical procedure, 100 μL of γ-Fe_2O_3 NPs and 10 μL of CdSe/CdZnS NPs in ethanol (prepared as described above) were added to 30 mg bare

silica microspheres (of diameter 300 nm) and 16 mg of hydroxypropyl cellulose (average molecular weight M_w = 370,000) in 10 mL of ethanol while vigorously stirring, followed by the addition of 50 μL of H_2O, 50 μL of NH_4OH (28 wt.-% in H_2O), and 0.15 mL tetraethoxysilane. The mixture was stirred in an oil bath at 75 ^{0}C for 1 hour. The SiO_2(core)//SiO_2,Fe_2O_3,CdSe/CdZnS(shell) microspheres were then purified by performing 3-5 cycles of centrifuging, discarding the supernatant, and redispersing the microspheres in 10 mL of ethanol.

5.3.4: Characterization of the product

TEM images provide information about the SiO_2 shell thickness, uniformity, and its roughness. **Fig. 5.5** is a typical TEM image of microspheres of 500 nm diameter containing γ-Fe_2O_3 (diameter of 15 nm) and CdSe/ZnS NPs in their shells. **Fig. 5.6** shows an expanded region from near the middle of **Fig. 5.5**.

Figs. 5.5 and **5.6** show that most of the micrsospheres have smooth shells. Occasional unincorporated NPs and agglomerates of NPs are observable in the background on the substrate. That suggests that the reaction conditions are not yet optimized, or that the NPs need to be better dispersed in ethanol before starting the reaction. Moreover, the amount of NPs incorporated into each microsphere is not uniform. The microsphere furthest to the right in **Fig. 5.6** appears to have lower coverage of NPs than the one immediately to the left of it.

SQUID characterization is used to quantify the number of γ-Fe_2O_3 NPs per microsphere. M_S is measured for M vs. H curves of a dried microsphere powder of known mass. The mass of each microsphere can be estimated based on the diameter in

TEM, and the moment of each γ-Fe_2O_3 NP can also be estimated from its diameter. However, the fraction of NPs which are unincorporated is unknown. Therefore, the number of NPs per microsphere measured from M_S is a high estimate and will not be meaningful until the portion of unincorporated NPs is reduced to a negligible level.

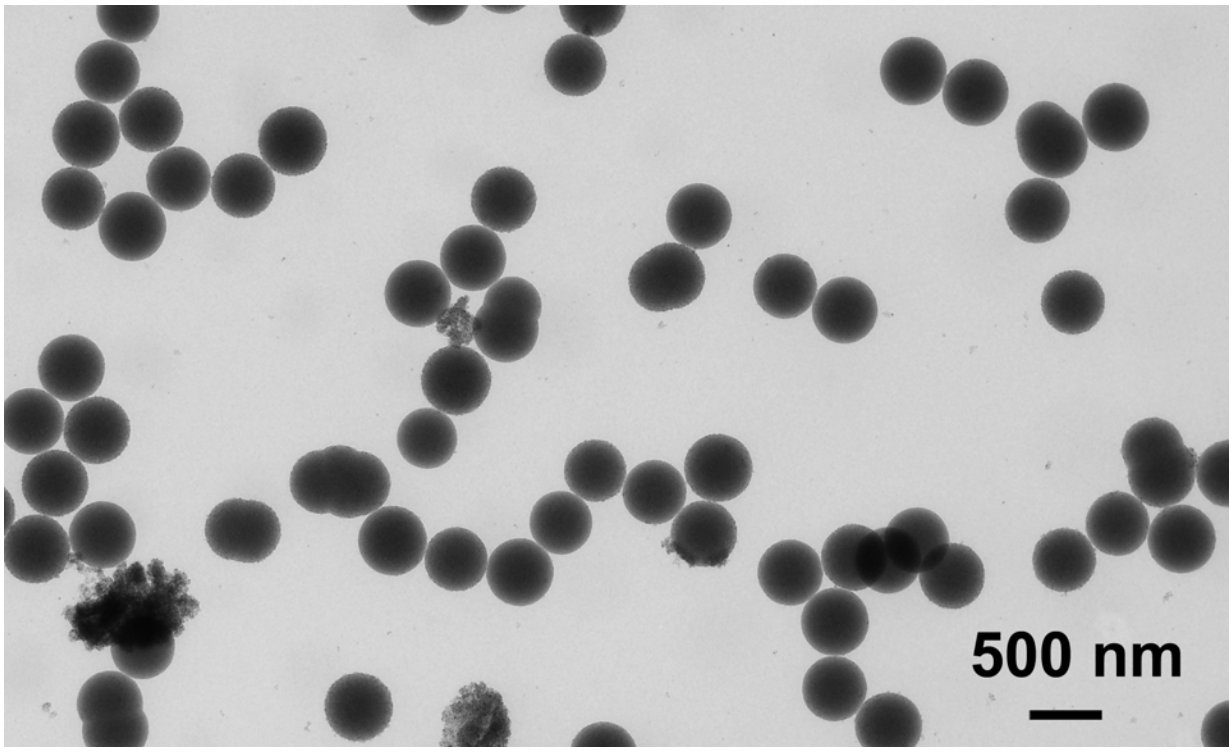

Fig. 5.5: TEM micrograph of SiO_2(core)//SiO_2,Fe_2O_3,CdSe/CdZnS(shell) microspheres of 500 nm diameter

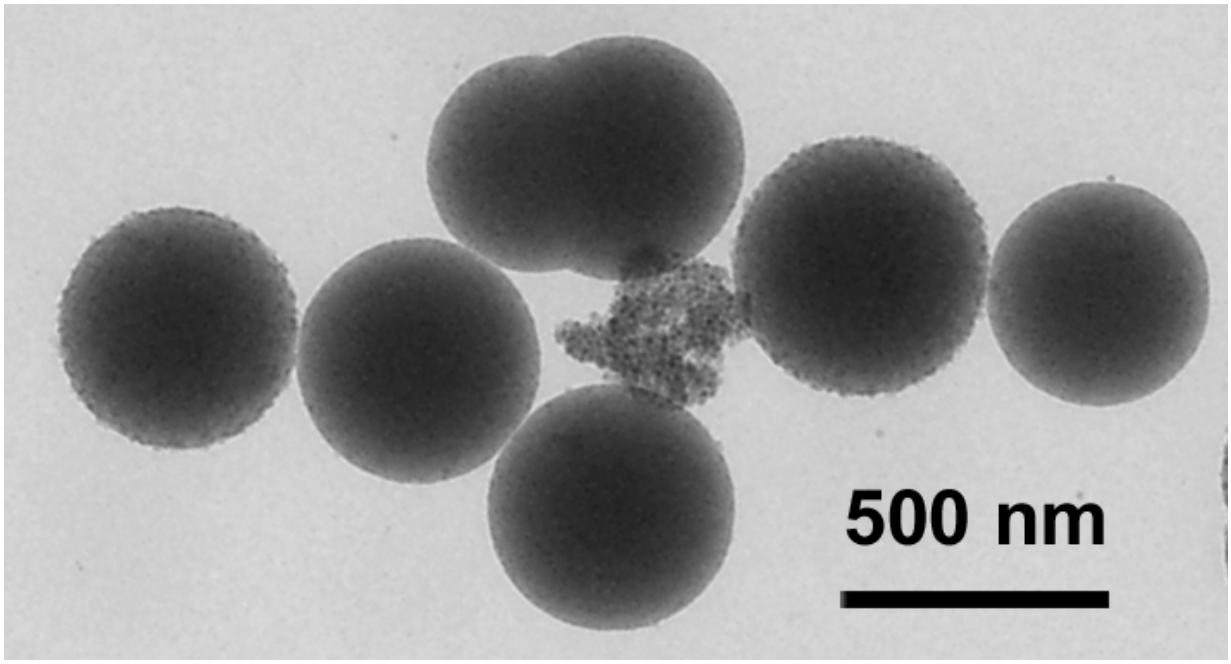

Fig. 5.6: Expanded region of **Fig. 5.5**

5.4: Trapping SiO_2(core)//SiO_2,Fe_2O_3,CdSe/CdZnS(shell) microspheres on a microelectromagnetic device

(The work in this section was done in collaboration with Numpon Insin and with Hakho Lee in the Westervelt lab at Harvard.)

Our collaborators at Harvard fabricate microelectromagnetic devices for the control and manipulation of magnetic NPs[14]. The devices consist of arrays of Au wires which generate magnetic fields and field gradients when current runs through them. Micron-sized magnetic beads, tagged cells, and magnetotactic bacteria[14-16] have been manipulated on these devices. For biological tagging and micromaniupulation, much smaller magnetic tags are desirable. However, particles smaller than the wavelength limit

for transmission mode optical microscopy also need to be functionalized with fluorescent tags for tracking their motion using fluorescence microscopy.

Preliminary results show that our SiO_2(core)//SiO_2,Fe_2O_3,CdSe/CdZnS(shell) microspheres can be manipulated on a microelectromagnetic device. Two samples of microspheres of diameter 300 nm were dispersed together in water, one with a SiO_2(core)//SiO_2,Fe_2O_3,CdSe/CdZnS(shell) composition with red emission, and a non-magnetic sample, SiO_2(core)//SiO_2,CdSe/CdZnS(shell) with green emission. A few drops of the solution were placed on the surface of the device, which consists of a set of parallel Au bars of width 2 μm with a center-to-center spacing of 8 μm with a thin insulating layer on the surface. A fluorescence image of this solution over the device with no current running is shown in **Fig. 5.7a**.

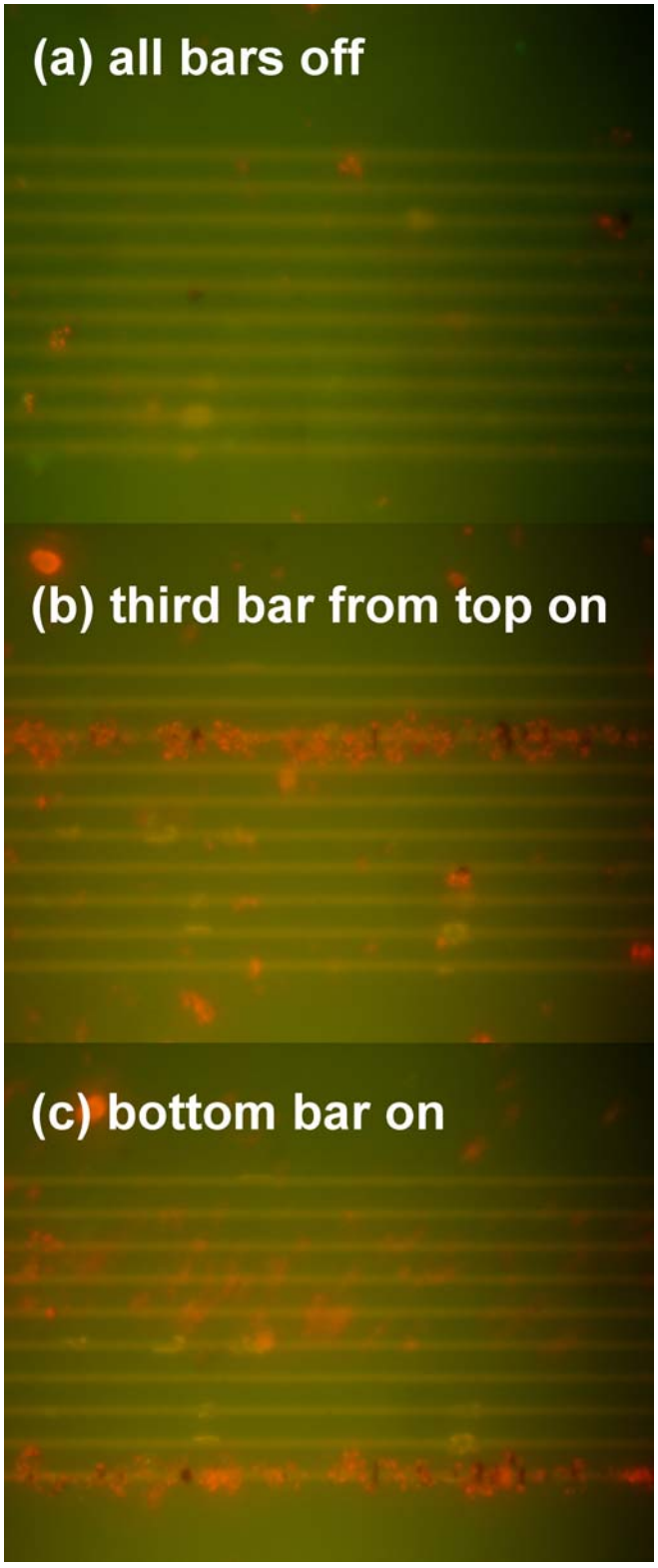

Fig. 5.7: Fluorescence microscope images of red-emitting magnetic microspheres and green-emitting non-magnetic microspheres in water over an array of gold bars with **(a)** all bars off, **(b)** the third bar from the top turned on, **(c)** the bottom bar on.

When current runs through the bar, a field of up to 0.007 T can be generated, and the corresponding field gradient is sufficient to trap the red-emitting microspheres. When the current on the third bar from the top was turned on, the red microspheres migrated towards that bar (**Fig. 5.7b**). The third bar was then turned off, and the bottom bar was turned on, and the red microspheres migrated towards it (**Fig. 5.7c**). The cloud of microspheres in **Fig. 5.7c** between the third and sixth bars from the top had been trapped on the third bar (**Fig. 5.7b**), but the field from the bottom bar began pulling them towards it, and they were eventually trapped there. This experiment demonstrates that the microspheres are responsive to small magnetic field gradients, since they can be moved over a the distance of 56 μm from the third bar from the top to the bottom bar, a distance at which the field gradient strength has significantly decayed. (Few green microspheres were observed in **Fig. 5.7** due to their low concentration and the green background emission coming from the insulating layer on the device surface.)

5.5: Conclusions

These preliminary results show that after certain problems are resolved, we will have prepared magnetic, highly luminescent microspheres than can be manipulated on a microelectromagnetic device. High quality, monodisperse γ-Fe_2O_3 NPs have been prepared. Methods of ligand exchange for dispersing them in ethanol have been developed but require further optimization. The reaction for incorporating NPs into SiO_2 shells needs further optimization so that the incorporation will be more uniform, and there will be fewer unincorporated NPs and aggregates. We would like to decrease the microsphere diameter from our current smallest size of 300 nm to 100 nm or below.

5.6: References

[1] T. Hyeon, S. S. Lee, J. Park, Y. Chung, and H. Bin Na, Journal of the American Chemical Society 123, 12798 (2001).

[2] F. X. Redl, C. T. Black, G. C. Papaefthymiou, R. L. Sandstrom, M. Yin, H. Zeng, C. B. Murray, and S. P. O'Brien, Journal of the American Chemical Society 126, 14583 (2004).

[3] X. W. Teng and H. Yang, Journal of Materials Chemistry 14, 774 (2004).

[4] W. W. Yu, J. C. Falkner, C. T. Yavuz, and V. L. Colvin, Chemical Communications, 2306 (2004).

[5] K. Woo, J. Hong, S. Choi, H. W. Lee, J. P. Ahn, C. S. Kim, and S. W. Lee, Chemistry of Materials 16, 2814 (2004).

[6] A. R. Bausch, W. Moller, and E. Sackmann, Biophysical Journal 76, 573 (1999).

[7] J. B. Dai, J. Q. Wang, C. Sangregorio, J. Y. Fang, E. Carpenter, and J. K. Tang, Journal of Applied Physics 87, 7397 (2000).

[8] A. F. Gross, M. R. Diehl, K. C. Beverly, E. K. Richman, and S. H. Tolbert, Journal of Physical Chemistry B 107, 5475 (2003).

[9] R. C. O'Handley, *Modern Magnetic Materials: Principles and Applications* (John Wiley & Sons, New York, 2000).

[10] A. E. Berkowitz, J. A. Lahut, I. S. Jacobs, L. M. Levinson, and D. W. Forester, Physical Review Letters 34, 594 (1975).

[11] V. F. Puntes, P. Gorostiza, D. M. Aruguete, N. G. Bastus, and A. P. Alivisatos, Nature Materials 3, 263 (2004).

[12] Y. Chan, J. P. Zimmer, M. Stroh, J. S. Steckel, R. K. Jain, and M. G. Bawendi, Advanced Materials 16, 2092 (2004).

[13] C. L. Chang and H. S. Fogler, Langmuir 13, 3295 (1997).

[14] C. S. Lee, H. Lee, and R. M. Westervelt, Applied Physics Letters 79, 3308 (2001).

[15] H. Lee, A. M. Purdon, and R. M. Westervelt, Applied Physics Letters 85, 1063 (2004).

[16] H. Lee, A. M. Purdon, and R. M. Westervelt, Ieee Transactions on Magnetics 40, 2991 (2004).

Chapter 6

Iron platinum alloy nanoparticles

6.1: Introduction

Colloidal FePt NPs are actively being pursued as a potential material for high density magnetic recording due to their high magnetocrystalline anisotropy[1]. **Table 2.1** shows two phases of FePt. The FCC phase of FePt has *K* comparable to FCC Co, but the FCC phase can be converted to the FCT phase by annealing, for which *K* is more than 15 times greater than for HCP Co[1].

However, all colloidal routes for preparing monodisperse FePt NPs produce the FCC phase, and the NPs sinter and agglomerate during anealing[2-4], thereby causing a polydisperse size distribution and inhomogeneous magnetic properties. If monodisperse FePt NPs in the FCT phase could be prepared for high density magnetic media, we calculate that a minimum NP diameter of 4.3 nm is needed using the formula, $KV = 70k_BT$ [5] at 300 K for a conservative estimate of the NP size that would be stable at room temperature. That is the reason why many studies of FePt NPs use NP diameters of 4 nm[1, 3, 6-8]. There are other challenges for applying FePt NPs in magnetic recording, such as the large switching field that would be required because of the high H_C of FePt[5].

Our initial interest in FePt NPs was primarily to incorporate the FCC phase into SiO_2 microspheres, as we demonstrated for γ-Fe_2O_3 NPs in Chapter **5**. FePt NPs are metallic[7] (in contrast to γ-Fe_2O_3, which is an insulator[9]) and may have interesting magnetotransport properties. Thiols are also reported to bind well to FePt NPs[10], which

may make much of the surface chemistry for Au NPs adaptable to FePt. Initial TEM results suggest that FePt NPs may fuse in solution, which has been observed previously in other NP systems[11].

6.2: Preparation of FePt NPs

We followed a literature method to prepare FCC FePt NPs[12]: 0.197 g of $Pt(acac)_2$ was added to 10 mL of benzyl ether and was heated to 100 °C. (The solution changed from a yellow to brown color during heating. The next step was done as soon as the temperature had stabilized at 100 °C.) While stirring, 135 μL of $Fe(CO)_5$ was added, followed by 1.32 mL of oleylamine (97%, Pfaltz & Bauer) and 1.27 mL of oleic acid (TCI). The mixture was heated to 240 °C for one hour, and then to reflux for two hours before cooling.

After cooling, the NPs were processed by first adding ethanol as a non-solvent to precipitate them. After centrifuging, the supernatant was discarded, and the NPs were redispersed in hexanes. However, they did not redisperse well, and 20 drops of a 50% (by volume) mixture of oleylamine and oleic acid were added, which caused the NPs to redisperse. Precipitating FePt NPs once removes so many of the amine and carboxylic acid ligands that the NPs will not redisperse in solution without adding more ligands. This solution was centrifuged, and any solids were discarded. The NPs were precipitated again by addition of ethanol. The NPs were redispersed in hexanes or THF when 20 drops of the oleylamine-oleic acid mixture were added.

Polymer sticks of the FePt NPs were prepared using the same procedure that is described for Co NPs in section **3.2.2**. In order to measure the alloy composition and to

calibrate the magnetization scale for the SQUID measurements, a piece of the polymer was sent out for elemental analysis by Galbraith Laboratories, Inc., using inductively coupled plasma – optical emission spectroscopy. The composition is $Fe_{39}Pt_{61}$. In future work, the NPs could be enriched in Fe by adjusting the amounts of $Pt(acac)_2$ and $Fe(CO)_5$ that are used in the reaction[12].

6.3: Surface chemistry

6.3.1: Octadecanethiol

In order to determine the relative binding strengths of thiols to the amines and carboxylic acids already present, an excess of octadecanethiol was added to the THF solution, and the THF was removed under vacuum. The NPs were redispersed in hexanes and were precipitated with ethanol. After centrifuging and discarding the supernatant, the NPs redispersed well in hexanes without adding more octadecanethiol. Therefore, thiols bind more tightly to the FePt NP surface than amines or carboxylic acids, because enough thiol ligands remained bound to the NPs after precipitation that the NPs could redisperse.

6.3.2: Solubility in ethanol

For future incorporation into a SiO_2 shell, ligand exchange must be performed to disperse the NPs in ethanol. After adding an excess of 12-hydroxydodecanoic acid to a solution of the FePt NPs in THF and removing the THF by vacuum, the precipitate is dispersable in ethanol. Attempts to repeat the same experiment using 6-mercaptohexanol or 11-mercaptoundecanol produced a non-dispersible cloudy aggregate.

If the THF solution is dried under vacuum after the last step in which 20 drops of the oleylamine-oleic acid mixture were added during processing, then the product (which is a viscous liquid, due to the oleylamine and oleic acid) redisperses into a 50% (by mass) mixture of AP and ethanol.

6.4: Transmission electron microscopy

From the TEM image of FePt NPs in **Fig. 6.1**, we estimate a diameter of about 8 nm. HRTEM images in **Figs. 6.2-6.5** show that the NPs are generally single-crystalline. However, **Fig. 6.3** shows an FePt NP that has a grain boundary. A few overlapping particles are observed in **Fig 6.1**, and HRTEM images of overlapping NPs are shown in **Figs. 6.4** and **6.5**. The images in **Fig. 6.4** show Moiré patterns due to the overlapping NP lattice planes. The images in **Fig. 6.5** suggest that the cores of the overlapping NPs have fused together, since the planes at the boundary seem to intersect in a more ordered manner than would be expected for two NPs which overlap without fusing.

For such fusion to occur, the ligands in the boundary region would have to be displaced. Such displacement may be easier in FePt NPs than for many other NPs because the amine and carboxylic acid ligands are weakly bound to the NP surface. The NP lattices do not appear to orient in the same direction in every case of fusion, but there is a continuous set of lattice planes observable across the pair of NPs in the left side of the middle panel of **Fig. 6.5**, which suggests that oriented attachment may occur. Although these results suggest that the FePt NP cores fuse, a more thorough study would be necessary to state that conclusively.

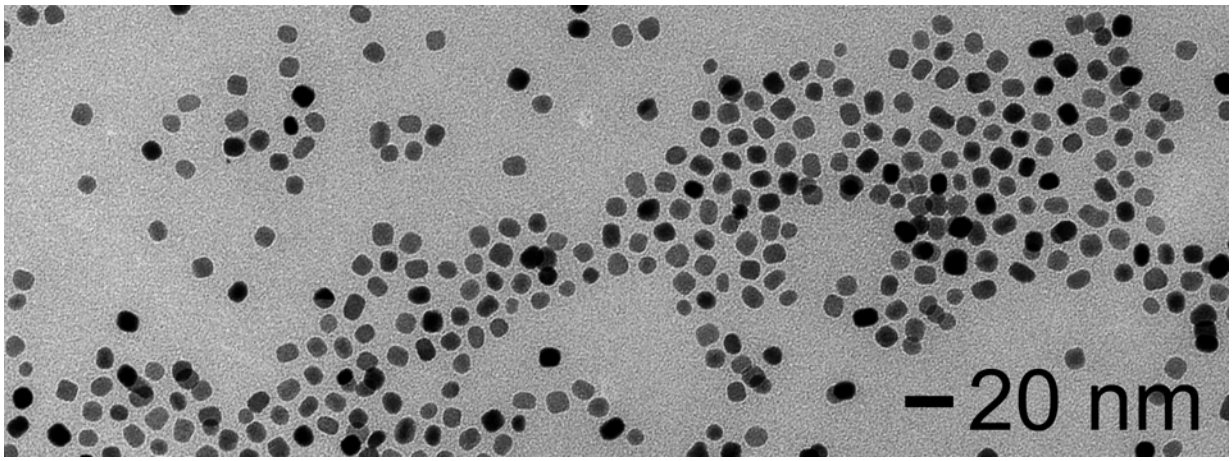

Fig. 6.1: TEM of FePt NPs

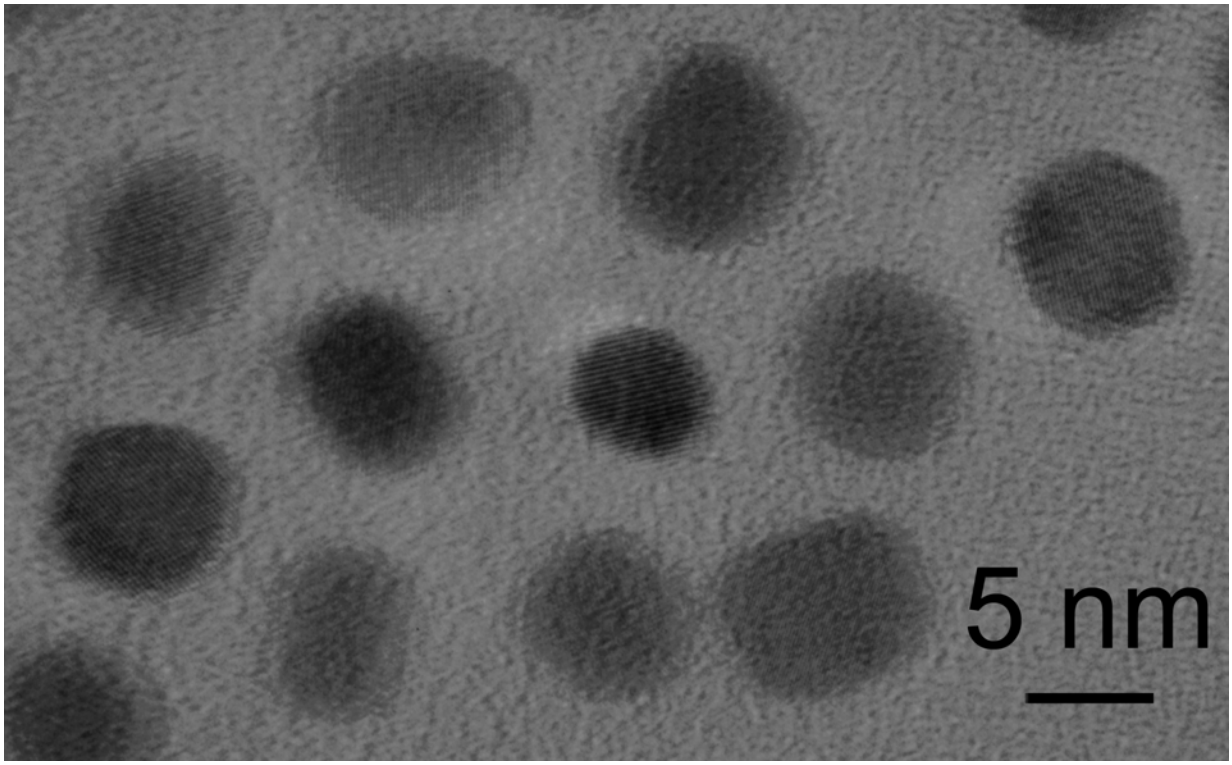

Fig. 6.2: HRTEM image of FePt NPs

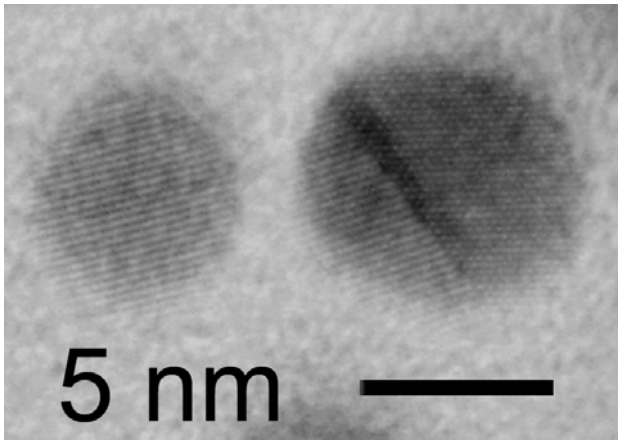

Fig. 6.3: HRTEM image of an FePt NP (right) showing a grain boundary

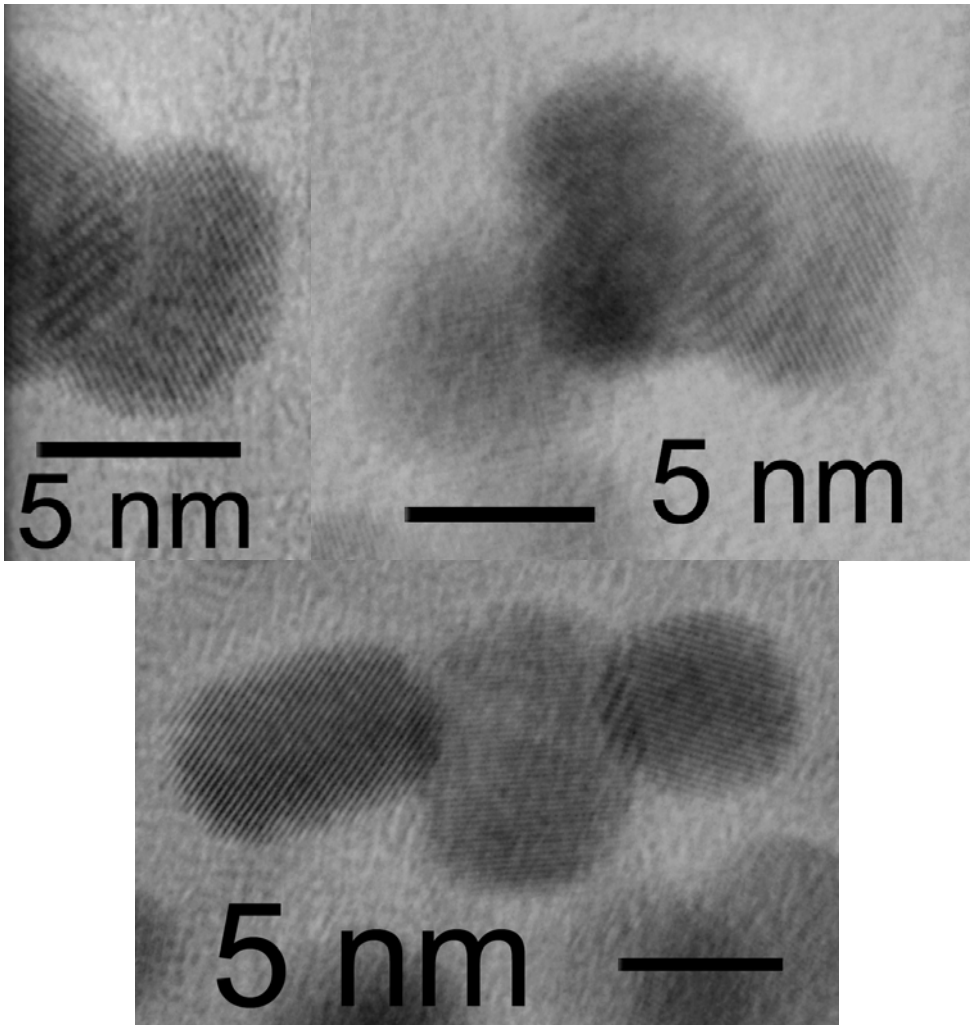

Fig. 6.4: HRTEM image showing Moiré patterns of overlapping FePt NPs

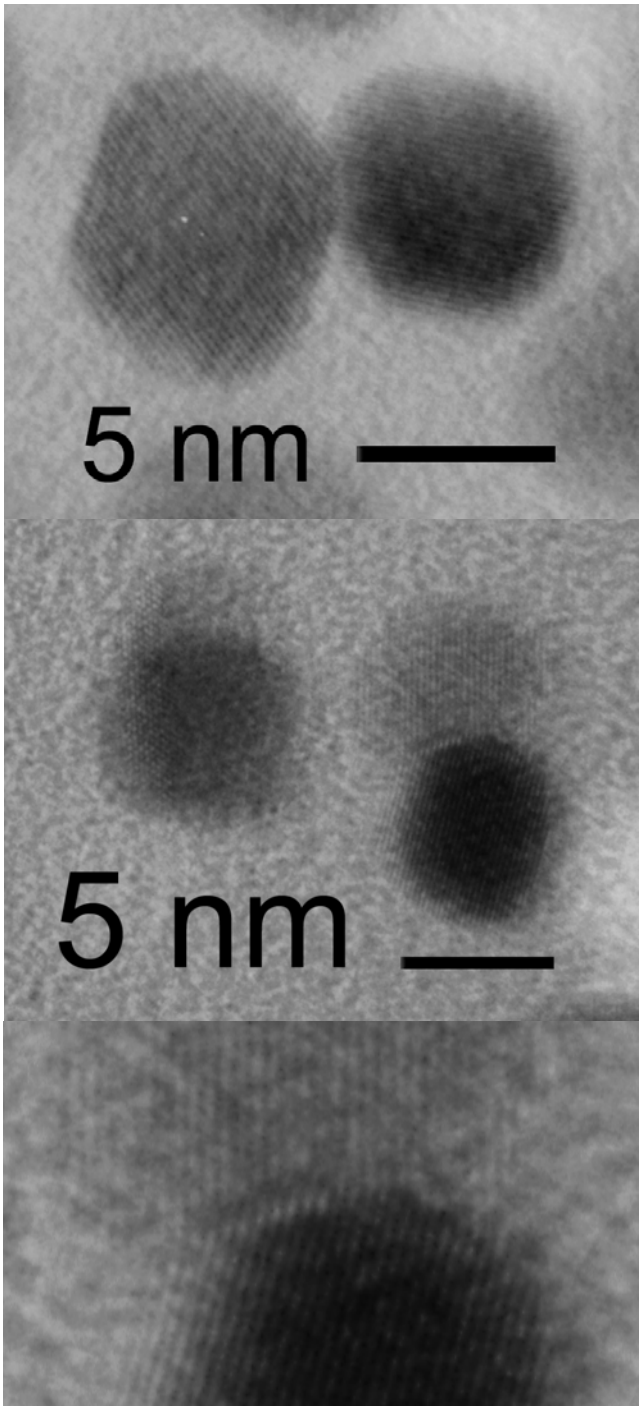

Fig. 6.5: HRTEM images which suggest crystalline attachment of two FePt NPs. The bottom panel is an enlarged region of the interface from the middle panel.

6.5: Magnetic characterization

Measurements of the zero field cooled *M* vs. *T* curve measured with 0.01 T applied field for the FePt NPs diluted in the polymer matrix are shown in **Fig. 6.6.** The blocking temperature is 55 K.

Measurements of *M* vs. *H* at 5 K after cooling from 300 K in a 5 T field are shown in **Fig. 6.7**. The saturation magnetization is 26 emu/g. We did not find a reference value for comparison, but this value is significantly smaller than for the Co and γ-Fe_2O_3 NPs reported in chapters **3** and **5**, respectively. One reason for the low saturation magnetization is because the alloy is richer in Pt than in Fe. We measured H_{EB} of -87 μT, which is caused by the alignment of the sample in the SQUID magnetometer and experimental uncertainty, and the value also depends on the spacing of the measurement points. This sample exhibits no EB. At 5 K, H_C is 0.11 T.

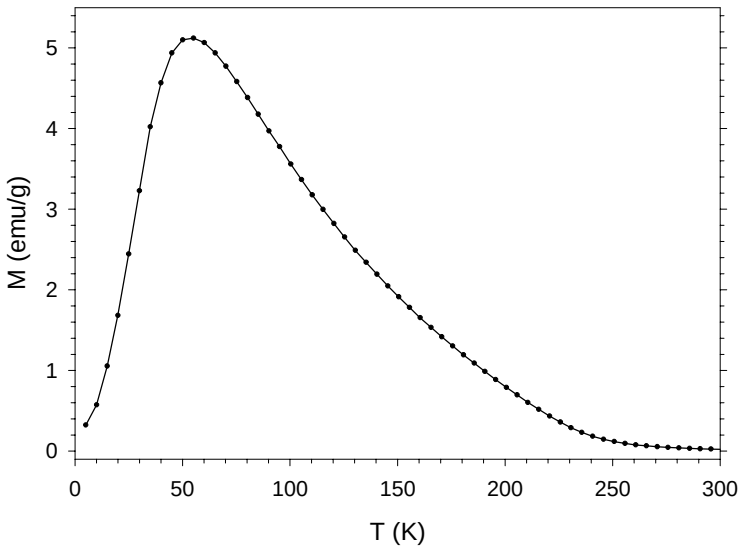

Fig 6.6: Zero field cooled *M* vs. *T* measured in a 0.01 T field for FePt NPs

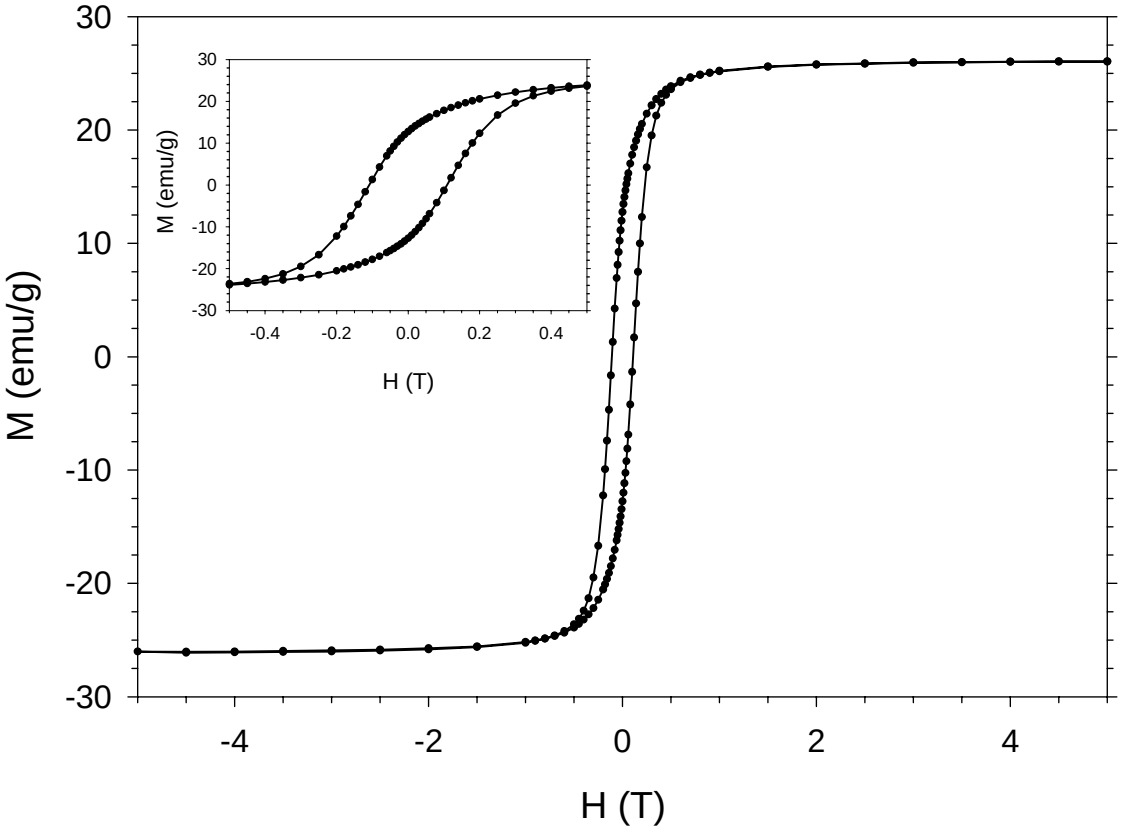

Fig 6.7: *M* vs. *H* at 5 K after cooling from 300 K in a 5 T field for FePt NPs. The inset shows greater detail of the same measurement.

6.6: References

[1] S. Sun, C. B. Murray, D. Weller, L. Folks, and A. Moser, Science (Washington, D. C.) 287, 1989 (2000).

[2] T. J. Klemmer, C. Liu, N. Shukla, X. W. Wu, D. Weller, M. Tanase, D. E. Laughlin, and W. A. Soffa, Journal of Magnetism and Magnetic Materials 266, 79 (2003).

[3] T. Thomson, M. F. Toney, S. Raoux, S. L. Lee, S. Sun, C. B. Murray, and B. D. Terris, Journal of Applied Physics 96, 1197 (2004).

[4] H. Zeng, S. H. Sun, T. S. Vedantam, J. P. Liu, Z. R. Dai, and Z. L. Wang, Applied Physics Letters 80, 2583 (2002).

[5] D. Weller, A. Moser, L. Folks, M. E. Best, W. Lee, M. F. Toney, M. Schwickert, J. U. Thiele, and M. F. Doerner, Ieee Transactions on Magnetics 36, 10 (2000).

[6] S. H. Sun, S. Anders, T. Thomson, J. E. E. Baglin, M. F. Toney, H. F. Hamann, C. B. Murray, and B. D. Terris, Journal of Physical Chemistry B 107, 5419 (2003).

[7] B. Stahl, J. Ellrich, R. Theissmann, M. Ghafari, S. Bhattacharya, H. Hahn, N. S. Gajbhiye, D. Kramer, R. N. Viswanath, J. Weissmuller, and H. Gleiter, Physical Review B 67 (2003).

[8] M. Ulmeanu, C. Antoniak, U. Wiedwald, M. Farle, Z. Frait, and S. Sun, Physical Review B 69 (2004).

[9] J. Tang, M. Myers, K. A. Bosnick, and L. E. Brus, Journal of Physical Chemistry B 107, 7501 (2003).

[10] N. Wang, E. Watson, X. C. Sun, and D. E. Nikles, Abstracts of Papers of the American Chemical Society 225, U434 (2003).

[11] Z. Y. Tang, N. A. Kotov, and M. Giersig, Science 297, 237 (2002).

[12] M. Chen, J. P. Liu, and S. H. Sun, Journal of the American Chemical Society 126, 8394 (2004).

Chapter 7

Functionalization and magnetic properties of commercial cobalt nanoparticles

7.1: Introduction

In this chapter, we report a method for functionalizing commercially available NPs to make them dispersible in organic solvents, and we characterized them using TEM and SQUID magnetometry. Strem Chemicals, Inc. recently started selling Co NPs at an inexpensive price of $67/g. They prepare the NPs in multiple gram quantities. In the method which they report[1], $Co_2(CO)_8$ and AlR_3 (where R is an alkyl group) are dissolved in toluene and heated. More AlR_3 is added to the mixture, and after continued heating, the preparation is complete. The only surface functionalization is the AlR_3, which acts as a stabilizer during NP growth[2, 3]. The AlR_3 is believed to form a thin shell on the surface of the NPs, which is consistent with the slower oxidation rate of the Strem NPs as compared with our Co NPs (Chapter **3**) that are prepared without AlR_3 reagents.

7.2: Surface chemistry

The bare NPs arrived precipitated in a small amount of toluene. Some of the bare NPs were added to THF, along with an excess of stearic acid or hexadecylamine. After stirring for a couple minutes, the THF was removed by vacuum. Hexanes were added to the powder, and after sonicating, some of the NPs dispersed into the hexanes, but many remained aggregated. After centrifuging, the supernatant was retained. This process

worked using both stearic acid and hexadecylamine, but the hexadecylamine dispersed a greater portion of the NPs.

A sample which was stabilized using hexadecylamine was dried under vacuum, and the NPs were diluted in a polymer stick using the same procedure described for our Co NPs in section **3.2.2**. In order to measure the Al content, pieces of the polymer and some of the bare NPs as-received from Strem were sent to Galbraith Laboratories, Inc. for elemental analysis using inductively coupled plasma – optical emission spectroscopy. The composition is $Co_{95.9}Al_{4.1}$. Therefore, the Al shell is quite thin.

7.3: Transmission electron microscopy

In ordr to remove excess ligands, a sample of NPs that was stabilized in hexanes using stearic acid was precipitated by adding ethanol. After centrifuging, the precipitate was redispersed in hexanes, and a drop of this solution was placed on the TEM grid. The TEM image in **Fig. 7.1** shows that the NPs have a distribution of sizes and shapes, but most are spherical with diameters between 11 nm and 15 nm. The variations in contrast across each particle show that they are polycrystalline, which is expected[1]. The HRTEM image in **Fig. 7.2** shows more details of the many small grains of which these NPs are composed.

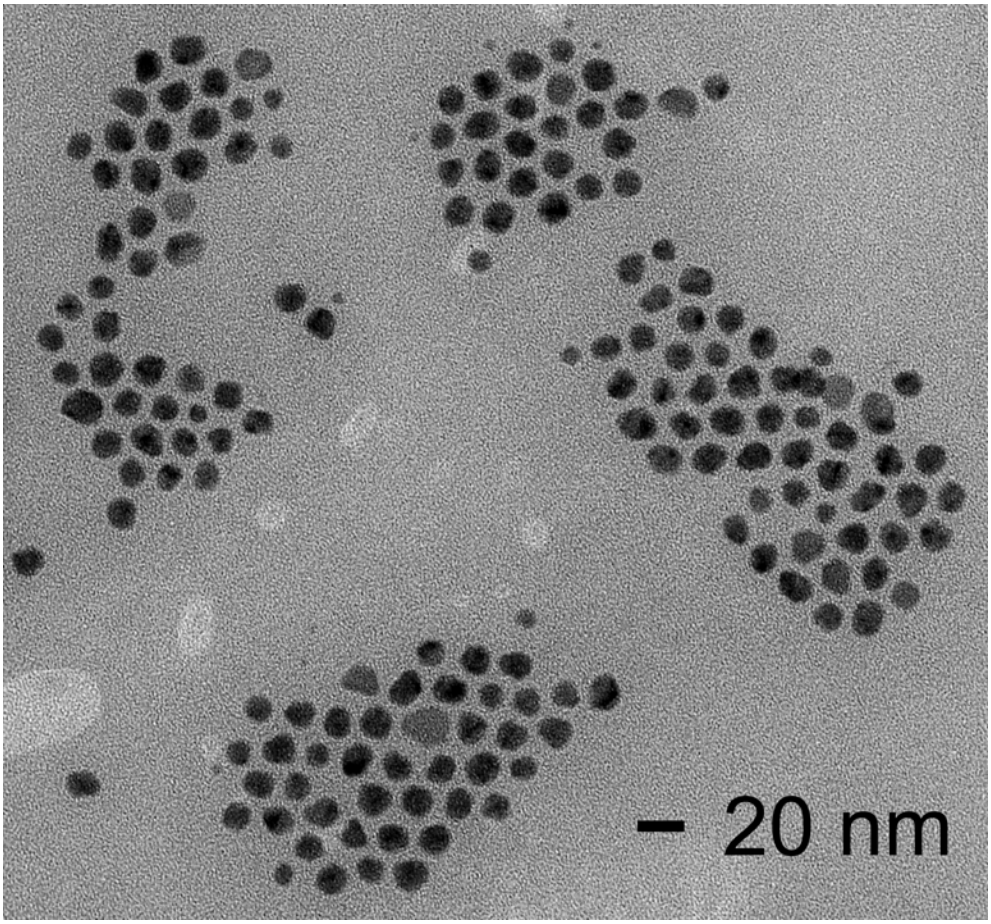

Fig. 7.1: TEM image of Strem Co NPs

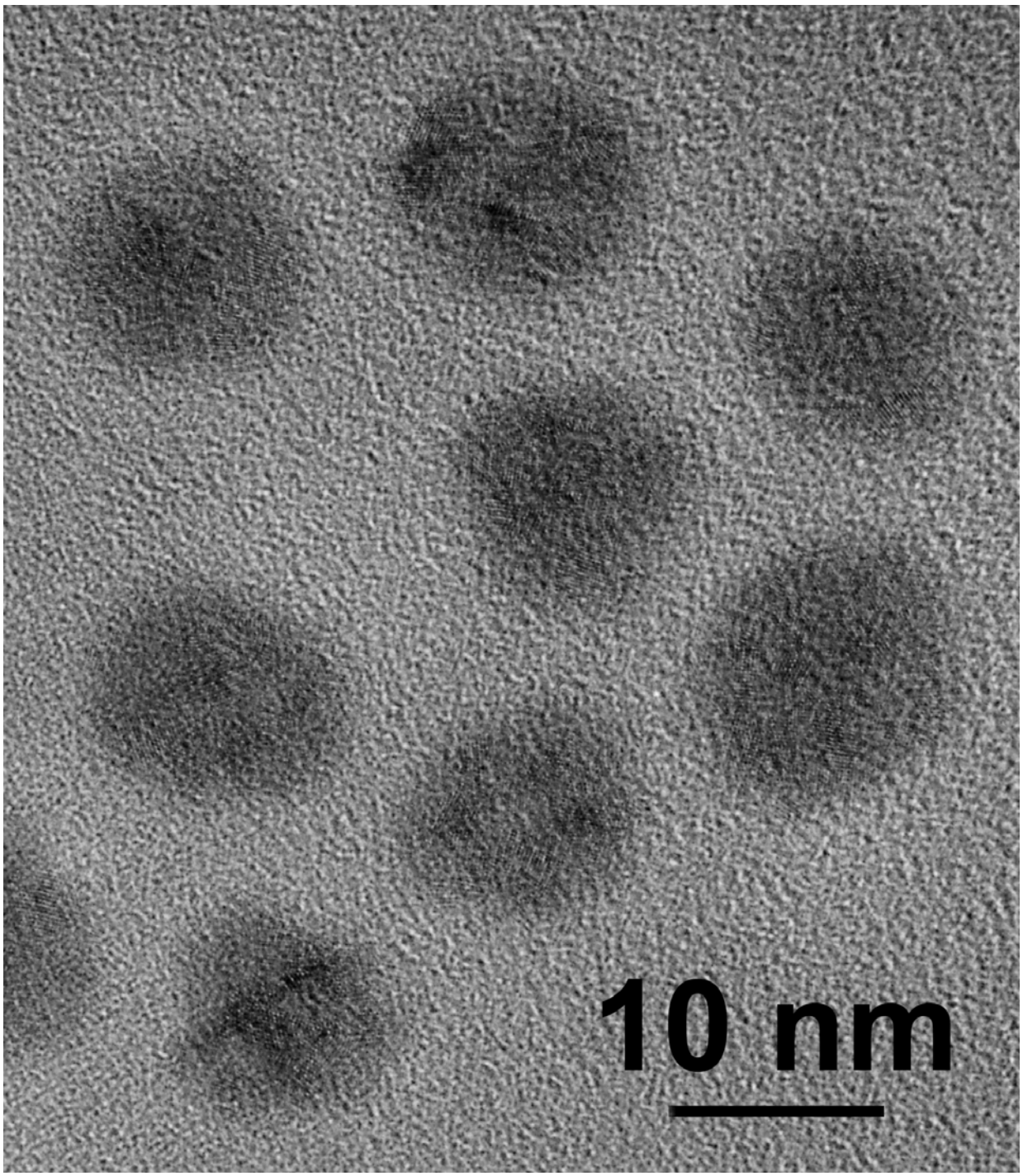

Fig. 7.2: HRTEM image of Strem Co NPs

7.4: Magnetic characterization

Measurements of the zero field cooled *M* vs. *T* curve measured with 0.01 T applied field for the Strem Co NPs diluted in the polymer matrix are shown in **Fig. 7.3**. The blocking temperature is 265 K. Because of this high T_B, the NPs may aggregate in solution at room temperature due to dipolar coupling. This dipolar coupling may be responsible for causing many of the bare NPs to remain precipitated after adding stearic acid or hexadecylamine to disperse them.

Measurements of *M* vs. *H* at 5 K after cooling from 300 K in a 5 T field are shown in **Fig. 7.4**. The saturation magnetization is 116 emu/g, which is 72% of the bulk value of 162 emu/g. This suggests that the NPs have a thin oxide shell. We measured H_{EB} of 0.023 T, which is small because the thin oxide shell is unable to significantly generate EB[4]. At 5 K, H_C is 0.18 T.

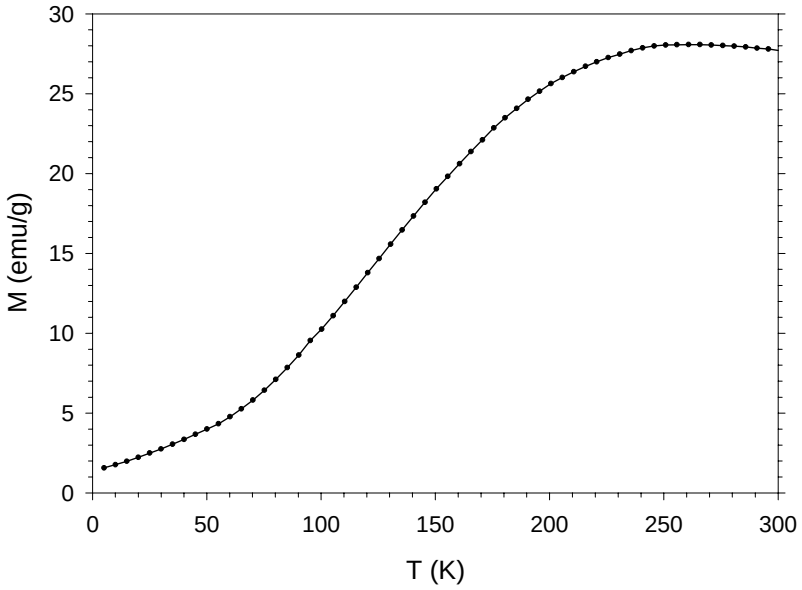

Fig 7.3: Zero field cooled *M* vs. *T* measured in a 0.01 T field for Strem Co NPs

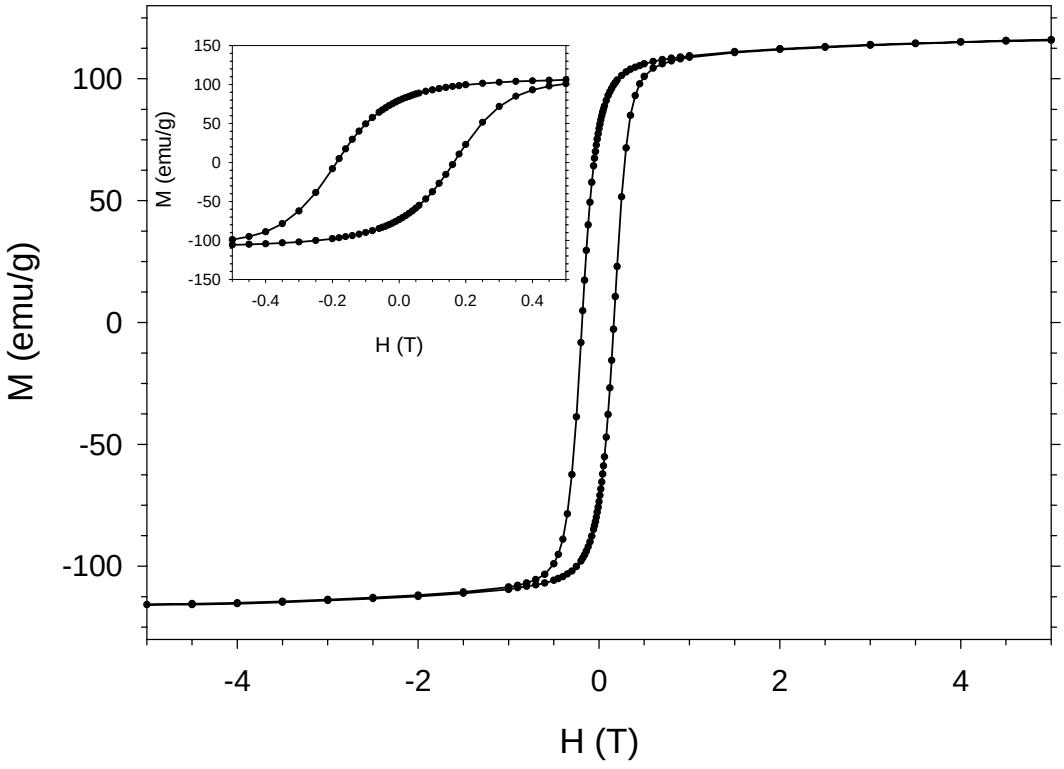

Fig 7.4: *M* vs. *H* at 5 K after cooling from 300 K in a 5 T field for Strem Co NPs. The inset shows greater detail of the same measurement.

7.5: References

[1] H. Bönnemann, W. Brijoux, R. Brinkmann, N. Matoussevitch, N. Waldofner, N. Palina, and H. Modrow, Inorganica Chimica Acta 350, 617 (2003).

[2] K. Angermund, M. Buhl, U. Endruschat, F. T. Mauschick, R. Mortel, R. Mynott, B. Tesche, N. Waldofner, H. Bonnemann, G. Koehl, H. Modrow, J. Hormes, E. Dinjus, F. Gassner, H. G. Haubold, T. Vad, and M. Kaupp, Journal of Physical Chemistry B 107, 7507 (2003).

[3] K. Angermund, M. Buhl, E. Dinjus, U. Endruschat, F. Gassner, H. G. Haubold, J. Hormes, G. Kohl, F. T. Mauschick, H. Modrow, R. Mortel, R. Mynott, B. Tesche, T. Vad, N. Waldofner, and H. Bonnemann, Angewandte Chemie-International Edition 41, 4041 (2002).

[4] V. Skumryev, S. Stoyanov, Y. Zhang, G. Hadjipanayis, D. Givord, and J. Nogués, Nature (London, United Kingdom) 423, 850 (2003).

Appendix G

Guide to transmission electron microscopy

(Dirk Weiss, John Zimmer, Mike Frongillo, and Tony Garratt-Reed have contributed to the content of this chapter by sharing their TEM experiences and knowledge with me.)

G.1: Motivation

TEM is a powerful characterization technique which I have had to use extensively in my research, because the easiest way to measure the size and distribution of my NPs is to use TEM. Others in the Bawendi lab who work with semiconductor NPs often have to do less TEM, because they can obtain the size and size distribution from absorbance and emission measurements. I write this chapter primarily for my Bawendi lab colleagues. TEM can have a steep learning curve, and I share here some things that I have learned by trial and error. Mike Frongillo in the CMSE microscopy lab at MIT gives a good training, and does an excellent job of keeping the microscopes running well using limited resources. However, the microscopes have many different aperture settings, and there are some things from experience that I emphasize here about how to do TEM on NPs well.

G.2: Sample preparation

The key to getting good TEM images is a well-prepared sample – in particular to get the right concentration of unaggregated particles and to get rid of enough of excess organics so that they do not blur the image. The procedure for preparing samples out of solutions of organics is well known in our lab, but the method for preparing samples from

aqueous solutions is not well known. I recommend putting a drop of the aqueous solution on the TEM grid and drying it (and the tweezers holding it) after 1-3 seconds using filter paper (Whatman 50). This technique gives much better results than drying the drop with a heat gun.

G.3: Microscope setup

The MIT microscopy lab has three transmission electron microscopes in operation: JEOL 200CX, JEOL 2000 FX, and a JEOL 2010. (A JEOL 2011 will soon be in operation too.) In each microscope, use the middle condenser aperture and a spot-size of 2. For the highest contrast imaging, use the smallest objective aperture. If the illumination with the smallest objective aperture is inadequate, use the smallest objective aperture with which you can get sufficient illumination. However, for high-resolution imaging, in order to see the lattice, use the largest objective aperture or none at all. When you put the objective aperture into place, if your aperture eliminates rings from the diffraction pattern, you will not be able to see the corresponding lattice planes in magnification mode.

G.4: Stigmation, focusing, and illumination

Stigmation is probably the most difficult part of using the TEM that requires the most practice, and no image that is poorly stigmated will be usable. Begin stigmating at low magnification using the Fresnel fringes of NPs or of the carbon substrate. Once you have stigmated at one magnification, increase the magnification and stigmate again. As you go to higher magnifications (100 kX and above), use the pattern of the carbon

substrate to stigmate. Use the stigmators to eliminate the parallel streaks that you observe if the image is slightly out of focus in either direction. Once you have done that, go to the point of best focus, and turn each stigmator knob one at a time in and out of the best stigmated image. Leave it at the setting that shows the clearest image without streaks in either direction during the focusing. Poor stigmation will ruin an image. Focusing is also important, although a well-stigmated but slightly out-of-focus image may still be useful. Stigmation and focusing need to be done together, and then once a well stigmated image has been achieved, the focus may be finely adjusted.

In order to describe optimal focus, we first describe what happens as one turns the focus knob. If we begin with the focus set above the grid, we can see the NPs below as dark spots with poorly defined edges. As we turn the knob clockwise, those edges initially shrink but become better defined, and the contrast decreases as the NPs come into focus. As we continue turning the knob clockwise, we also see the grains in the carbon substrate come into focus. If we observe carefully, those grains come into focus, and as we keep turning, they become blurry, then they come back into focus again and become blurry again, and the Fresnel rings around the NPs become visible as we keep turning the knob out of focus.

The important part of focusing is when we see the carbon grid for the first time as we move the focal plane downward (turning clockwise) from above the grid. The best focus occurs when the grains of the carbon substrate are clearly resolved right before they blur as we keep turning the knob clockwise. I have had the best results by looking for the blurry spot between the two focus settings in which the grains of the carbon substrate are in focus and then turning the knob slightly counter-clockwise until I get a good image of

the carbon substrate. This technique is also quite useful for taking pictures of small NPs that may not appear well on the monitor. One can focus on the substrate and take pictures, and small NPs may be visible in the films. This is particularly useful for HRTEM on the 2010.

Having the condenser lens spread the beam is also important for taking good images. If the beam is not spread, then the stigmation can vary across the area of the film. This is particularly important for HRTEM on the 2010.

G.5: Magnification

For most NPs that are smaller than 20 nm in diameter, I recommend using a magnification of 100 kX for publication-quality images. These images can be blown-up if necessary. The same image taken at 200 or 210 kX usually has less contrast than the same image which was taken at 100 kX. In order to get a good image at 100 kX, I recommend stigmating at 200 kX (or higher, if possible). When doing HRTEM on the 2010, most of my useful images are taken at 600 kX and 800 kX. Pictures taken at 1,000 kX are desirable, but one has to wait even longer for the sample translators to stabilize. Images at 800 kX give a greater image area, and this magnification is usually sufficiently high. Pictures taken at intermediate magnifications between 100 kX and 600 kX are not that useful.

G.6: Taking pictures

If the beam is spread as suggested in section **G.4**, a longer exposure time will be needed than for a beam which is tightly focused. I recommend using exposure times of

2-3 seconds, but you may need longer times for HRTEM on the 2010. If you put down the smaller screen while setting up to take the picture, it will give you a better reading of the illumination intensity to use for the picture.

To get good images, take many pictures, and take the time to stigmate and focus them well. This is especially true for HRTEM on the 2010.

G.7: Electron diffraction

Electron diffraction is a powerful technique that provides much of the same information as X-Ray diffraction (XRD), and it does not require the large amount of sample that is needed for XRD. Single-NP electron diffraction is challenging, but the electron diffraction ring pattern from a sample of many NPs is useful for identifying the stoichiometry of the material, or whether the sample is oxidized. In order to measure lattice constants quantitatively, the camera constant needs to be measured using a calibration standard, but the crystal structure can often be identified from the ring pattern without calibration.

Electron diffraction is done as follows:

1. Choose an area of the sample for which you want a diffractogram and bring it into focus. Center the beam.
2. Enter the selected-area magnification mode.
3. Insert a selected-area diffraction (SAD) aperture. Use the diffraction focus knob to get as sharp an image of the rim of the aperture as possible.
4. Enter diffraction mode. Use the diffraction focus knob to focus the center spot. Rotate the condenser knob to decrease the illumination while continuing to focus the

center spot. As you decrease the illumination, the size of the center spot will decrease. Continue to decrease the illumination until the spot is quite small. Use the projection alignment to center the spot.

5. Move the pointer so that it covers the center spot. You will be able to do this best using the small screen and the binoculars.
6. Take a series of pictures of different exposure times. If the illumination is still bright, start with exposures with times of 4, 8, 16, 32, and 64 seconds. If it is darker, start at 8 or 16 seconds.

Another way to select an area of the grid which will give a good diffraction pattern is to insert an SAD aperture, to enter diffraction mode, and then to translate the sample until a good diffraction pattern appears.

G.8: Choosing the right microscope

The 200 CX is a great microscope, and it is quick to use! With practice, taking pictures at 100 kX is pretty easy. Reliable stigmation at 200 kX is more challenging, and I recommend using the 2000 FX for publication quality images. For getting the highest contrast low-resolution images, I recommend using the 2000 FX rather than the 2010. The contrast is better, and microscopy is faster. Use the 2010 for lattice imaging.

G.9: Developing pictures

Developing the films is pretty straight-forward, except variations in the developer temperature can lead to overdeveloped (too dark) or underdeveloped (too transparent) films. This is especially the case in the winter, when the lower temperature in the rinsing

bath can cool the developer. The optimal developer temperature is 19 °C. I carry a thermometer with me and check the developer temperature every time before developing my films. If it is too cold, I add hot water to the rinsing bath to heat the rinsing bath to 19 °C (and the thermal currents will then heat up the developer). Be careful not overheat the rinsing bath, since that will lead to overdeveloping. I have generally found slightly underdeveloped films easier to salvage than overdeveloped ones, so I aim to err towards slightly underdeveloping my films.

During the final washing step after fixing, I have always found 5 minutes to be a sufficient washing time.

G.10: Scanning pictures and adding scale bars

I recommend scanning the whole negative in the scanner at the CMSE facility at 1,600 dpi. That generates large files (50-60 MB), but it maximizes one's ability to select and magnify the best images afterwards. Photoshop provides the best contrast adjustment.

The scale bars printed on the negatives from the 2000 FX and 2010 are inaccurate and should not be used. A simple way to calculate the scale bar length is to convert the 1600 dpi (which is pixels per inch) to 629.92 pixels/cm. Using a magnification of 100 kX as an example, if we convert 629.92 pixels/cm to nm and multiply by 100,000, then we get 6.2992 pixels/nm. To make a 10-nm scale bar in Photoshop for a picture taken at 100 kX, we would draw a thick line 63 pixels long. For a more accurate magnification measurement, the magnification would need to be calibrated to a standard.

Acknowledgements

I thank God for providing me with good research results and an interesting research topic. This research has renewed my sense of wonder of God's creative power and of his timing for providing unusual results and insights in the experimental design and analysis. HRTEM is rather tedious, but I enjoyed being able to observe individual lattice planes in NPs because it reminded me of how highly ordered our world is. Although synthetic procedures, instrumentation, and analysis techniques have been developed by people, this human creativity appears to me as a small reflection God's greater creativity in making a highly-ordered universe with many unusual physical phenomena to study and apply. I also sensed God's provision as I came up with ideas for the critical steps in the experimental design and analysis, and for providing me with a supportive community of people who have encouraged and challenged me to persevere in my work, but also to see it in a broader context. I thank this community for helping make my time in graduate school an exciting time of growth.

I dedicate this thesis to my family and to my many friends in Boston, with whom I've shared many joys and struggles, and to Lisa and our future family, with whom I will share many joys and struggles. From a young age, my parents encouraged my curiosity in the world around me. As I got acquainted with that world, I broke many tape measures by pulling the tape out too far, and I asked many unanswerable questions, yet I expected them to have the answers. I thank them for the sacrifices that they made in raising me, in cultivating my curiosity, and for encouraging me to pursue my dreams. I thank Sarah, for being a caring older sister, fun playmate, great friend, and willing coadventurer in some of my investigations about the world around me, even though she did occasionally require some coaxing. I am thankful to Sarah that she experienced many things in life before I did, and that I could see and learn from her experiences. I miss you, Sarah.

I thank my aunt and uncle, Carole and Roger, for challenging me with scientific puzzles, and for encouraging me to try things that I didn't think I could do. I thank my high school teachers for their interest in me, for their encouragement, and for laying a great foundation for my future studies. I thank my undergraduate advisor, Don Aue, for the excellent mentoring and advice that he has provided. I thank Geoff Strouse for providing me an opportunity to work on semiconductor nanocrystals in his lab as an undergraduate, and for helping develop my interest in the nanoworld.

I thank Moungi Bawendi for his mentoring and advising me at MIT. I am thankful for the latitude which he has given me to seek my own research project and to follow it wherever the interesting research results would lead me. He has been patient with me when my research was going slowly. I am thankful for the meticulousness which he has models, and for his reminders that control experiments are really important.

I thank my many labmates in the Bawendi lab, who have encouraged me, collaborated with me, and who have shared many ideas. They have also reminded me (usually in a positive way) that personality plays an important role in doing science. I have been quite fortunate to work with such a group of fun, talented people.

I thank Bob O'Handley, Young Lee, and Marc Kastner, for discussing my research with me, and for helping me better understand magnetic materials. I thank Mike Frongillo for training on the TEM, and for keeping the microscopes running well. I thank Fangcheng Chou for training on the SQUID. I thank the DOD for a graduate fellowship.

I am thankful for the many friends who have helped me to grow in the rest of my life outside of graduate school during this time. I thank my brothers and sisters in Graduate Christian Fellowship at MIT and at Park Street Church for helping me to grow in my faith, for supporting and encouraging me through some very difficult times, and for helping me to see my research in a broader context.

In particular, I am thankful to my best friend and fiancée, Lisa. I am thankful for how she has loved me in caring for me deeply and for her steady encouragement and inspiration not only in my research, but in continuing to grow in all aspects of my life. I am thankful for the thoughtfulness, tenacity, and sense of discipline which she models. Lisa has been a great partner in endeavors of all kinds – the fun, silly, and the serious. As my time in graduate school comes to a close, I look forward to our life together with great joy, and to the many chapters that we will write together.